NORTHWESTERN UNIVERSITY

Electric and Magneto-Electric Nonlinear Optical Response of Twisted Intramolecular Charge Transfer Chromophores

A DISSERTATION

SUBMITTED TO THE GRADUATE SCHOOL
IN PARTIAL FULFILLMENT OF THE REQUIREMENTS

for the degree

DOCTOR OF PHILOSOPHY

Field of Chemistry

By

Alexander Jen-Tong Lou

EVANSTON, ILLINOIS

September 2018

ABSTRACT

Electric and Magneto-Electric Nonlinear Optical Response of Twisted Intramolecular Charge Transfer Chromophores

Alexander Jen-Tong Lou

Nonlinear optical (NLO) effects are used universally in modern day telecommunication and form the foundation of emergent photonic technologies. Twisted intramolecular charge transfer (TICT) chromophores, composed of a donor and acceptor fragment connected by a twisted bi-aryl bridge, combine large molecular NLO response with properties such as transparency in the IR region, thermal stability, and compact chemical structure, which makes them promising candidates for use in electro-optic devices. In this work we elucidate the impact of structural and environmental changes on 2nd order (β), 3rd order (γ), 5th order ($\chi^{(3)}:\chi^{(1)}$), and magneto-electric (M_y and P_z) NLO response of TICT chromophores. *Chapter 1* reports the synthesis and characterization of a series of high-β TICT chromophores that utilize a new type of acceptor group and exhibit intermediate bi-aryl torsional angles which were previously inaccessible. Whereas earlier TICT chromophores exhibited poor performance in polar solvents, this series maintains a high β value in DMF. The use of polar solvents has the added benefit of mitigating aggregate formation, thereby enhancing β in concentrated solutions. *Chapter 2* explores the interactions of the highest performing chromophore of the series, B2TMC-2, with organic salt additives, which lead to large spectroscopic changes and improved β values. The origin of these effects is determined to be coulombic attraction between the salt and the chromophore acceptor group, which competes with dipole-driven aggregate formation. The increases in β arise entirely from the disaggregating property of the salt, and we demonstrate that the same interactions in solution persist in host/guest films. In *Chapter 3*, we explore the impact of hybridizing a stilbene and TICT chromophore on γ

and $\chi^{(3)}$:$\chi^{(1)}$. The observed two-photon absorption is attributed to the stilbene fragment, while the excess polarizablity is related to the twisted fragment, which causes localization of ground and excited states. The $\chi^{(3)}$:$\chi^{(1)}$ response contributes significantly to nonlinear refraction, and highlights the drastic change in NLO response resulting from a subtle structural modification. In *Chapter 4*, we outline the theoretical underpinnings of the first connections between magneto-electric response and molecular structure, showing that the twist motif can be productively applied to 2-D molecules. The sum of this work provides insight into the impact of bi-aryl twist angle, acceptor group identity, and environmental factors on several NLO effects, and in many cases yields productive guidelines based on deep understanding of specific cause/effect relationships.

Acknowledgement

I have been fortunate during my Ph.D. work to enjoy the support of family and friends, and to have the opportunity to work with excellent collaborators. I would first like to thank my advisor, Prof. Tobin Marks, for his support and trust in my ideas and work. The freedom to pursue my own ideas, and to have ownership of my successes and failures has been an important part of my education. I would like to thank my committee members, Prof. Dave Harris for his continued support and interest in my career, and Prof. Antonio Facchetti for useful discussions and encouragement. I would also like to thank Prof. Steve Rand for the opportunity to be a part of the DYNAMO project, and the Foundation of Nonlinear Optics conference which was an annual opportunity that helped me develop as a scientist.

None of this work would have been possible without the cooperation and expertise of my collaborators. In particular I would like to acknowledge Elena Cariati, Stefania Righetto, Cristiano Zuccaccia, and Alceo Macchioni for their contribution to this work. I would also like to thank Alexander Baev and Sepehr Benis for their tenacious effort and Liz Dreyer for laying the foundation for our theoretical work on magneto-electric effects.

Graduate school would not have been the same without friends, family and colleagues. First, I'd like to say thank you to my colleagues Tom Aldrich, Steven Swick, and Ferdinand Melkonyan for the company in lab. I am proud to continue the tradition of science in my family - I was particularly inspired by my grandmother, who was dedicated to science education, and my parents. Special thanks to my cousin Kathryn Connolly, and to my sister Mimi. Finally, thanks to my friends for all of the great times we have at Northwestern! I can't imagine graduate school without them, especially Scott, Ryan, and Jordan. And lastly, I want to thank my fiancée Sam for supporting and encouraging me and for being my best friend.

Table of Contents

List of Figures

List of Tables

List of Schemes

Introduction

0.1 Applications and fundamentals of NLO. The field of nonlinear optics (NLO) encompasses a multitude of phenomena, some of which find widespread commercial use, while others form the foundation of emergent technologies.[1-5] Most notably, 2nd order NLO materials constitute the active component of electro-optic modulators which are used for ~99% of all intercontinental communication.[6] Such ubiquitous applications have motivated improvements in NLO response of organic materials at the microscopic (molecules) and macroscopic (bulk materials) level, while interest in emergent technologies such as all-optical switching and computing have driven the development of 3rd order NLO materials.[7] Beyond this, recently discovered magneto-electric nonlinearity may lead to even more intriguing applications including cloaking, high efficiency light-to-electricity conversion, and negative permeability materials.[8,9] It is therefore important to develop materials which can exhibit large NLO effects and are suitable for these applications. Organic materials, composed of molecular or polymeric chromophores, are of particular interest due to their potential for very high NLO response, and the opportunity to create targeted synthetic changes which probe specific structure/property relationships. This work focuses on deepening our understanding of a unique class of organic NLO active chromophores with the goal of improving their suitability for 2nd order, 3rd order, and magneto-electric applications.

The simplest description of NLO effects in a molecular system begins with the electric dipole moment, μ, which is a vector that represents a distribution of point charges defined as eq. 0.1, where q is a point charge and r is the position of the charge m with respect to the origin.

$$\vec{\mu} = \sum_m q_m \vec{r}_m \quad (0.1)$$

$$\mu(F) = \mu_0 + \mu_{\text{ind}}(\text{F}) = \mu_0 + \alpha F_1(\omega) + \tfrac{1}{2} \beta F_1(\omega)F_2(\omega) + 1/6\, \gamma F_1(\omega)F_2(\omega)F_3(\omega) + \ldots \quad (0.2)$$

In the context of a molecule, μ represents the electron distribution within the molecular scaffold. This distribution can be altered by the application of an external electric field, $F(\omega)$, leading to a field-dependent dipole moment, $\mu(F)$, which is the sum of the intrinsic moment (μ_0) and the field induced change in dipole moment (μ_{ind}).The perturbation of μ by an electric field can be expressed as a Taylor series (eq. 0.2), where α is the linear polarizability, and β and γ are the nonlinear coefficients for 1st and 2nd hyperpolarizability respectively. When $F(\omega)$ is small, as with non-intense light, the first two terms are sufficient to describe light/matter interactions. However, when $F(\omega)$ is large, as with lasers and high voltage DC fields, the latter terms, which scale as $F(\omega)^2$ and $F(\omega)^3$, become increasingly important and give rise to useful phenomena. These terms, and higher order ones not discussed here, constitute the field of nonlinear optics. On the bulk scale, an equivalent expression can be written to describe the polarization (P) of a material; macroscopic and molecular NLO response are related as $\chi^{(1)} \propto \alpha$, $\chi^{(2)} \propto \beta$, and $\chi^{(3)} \propto \gamma$, although the exact relationship includes number density, local field corrections, and orientational considerations as described elsewhere.[10]

$$P(F) = P_0 + \chi^{(1)} F_1(\omega) + \tfrac{1}{2} \chi^{(2)} F_1(\omega)F_2(\omega) + 1/6\, \chi^{(3)} F_1(\omega)F_2(\omega)F_3(\omega) + \ldots \quad (0.3)$$

In eqs. 0.2 and 0.3, the fields can have different frequencies, ω, or be applied along specific Cartesian directions. Two conventions account for these scenarios: First, for a 2nd order process, one would write $\beta(\omega_1; \omega_2, \omega_3)$ meaning the input to the NLO process is two photons of frequency ω_2 and ω_3 and the output is one photon with ω_1, with $\omega_1 + \omega_2 + \omega_3 = 0$ to conserve momentum. It is often useful to employ this practice to describe certain common effects such as second harmonic generation $\beta(-2\omega; \omega, \omega)$ or the electro-optic effect $\beta(\omega; 0, -\omega)$. Second, because α, β, and γ are tensors, they can relate any Cartesian component of the input fields to NLO response in any direction. For example, γ_{xzzz} represents the 3rd order nonlinear optical response along the *X* direction that results from the application of three fields along the *Z* direction. For an all-electric process far from resonance, Kleinmann symmetry can be applied such that the Cartesian indices can be freely permuted.[10] This simple notation allows one to convey a great deal of information in one compact term and is used extensively in *Chapter 4*.

In many cases, the nonlinear susceptibilities and coefficients themselves do not carry useful physical significance, thus it is often helpful to discuss their relationship to refractive index, *n*.

$$n(\omega) = n_0(\omega) + \frac{4\pi\chi^{(2)}}{n_0}E(0) + \frac{6\pi\chi^{(3)}}{n_0}E(0)^2 + \frac{12\pi\chi^{(3)}}{cn_0^2}I(\omega) \quad (0.4)$$

The terms contributing to $n(\omega)$ in the presence of an electric field are (in order): the linear refractive index (n_0), the Pockels effect, the Kerr effect, and the optical Kerr effect. The Pockels effect is a 2nd order ($\chi^{(2)}$) phenomenon in which the material refractive index depends on a static field, $E(0)$, and finds widespread use in electro-optic modulators, which translate digital electronic information into optical signals.[11,12] The optical Kerr effect is a 3rd order process in which light itself can change the refractive index of a material, and therefore forms the basis of many all-optical switching schemes.[7,13,14]

0.2 Design of 2nd order NLO chromophores. Organic chromophores are promising materials for electro-optic modulators, as they combine large molecular β (and therefore $\chi^{(2)}$), straightforward device incorporation, and molecular tunability.[11,12,15,16] The development of these chromophores has relied heavily on a simple yet instructive two-level model (2LM), which assumes that only the properties of the electronic ground and first excited state are needed to describe the NLO response.[10,17]

$$\beta_{2L} = \frac{\mu_{eg}^2 \Delta\mu_{eg}}{E_{eg}^2} \quad (0.5)$$

Here, β is defined by the excitation energy (E_{eg}), the transition strength (μ_{eg}), and the change in dipole moment between ground and first excited state ($\Delta\mu_{eg}$). In general, the strategy to optimize μ_{eg} and E_{eg} involves the use of an electron poor (acceptor) and an electron rich (donor) moiety connected by a planar π-conjugated system, which creates a low-lying charge transfer (CT) state with considerable transition strength. Upon excitation from *g* to *e*, a significant amount of electron density is transferred from donor to acceptor moiety, giving rise to large values of $\Delta\mu_{eg}$. Using this strategy, a library of planar D-π-A chromophores were developed to optimize β, though all efforts fell below the fundamental limit on β by a factor of at least $10^{-3/2}$.[12,15,18] Another approach, called bond length alternation, has been used to optimize the donor, acceptor, and bridging fragments to produce some of the highest β chromophores to date, although ultimately these molecules still fall within the planar D-π-A paradigm.[11,19-22] The closest approaches to the theoretical limit of β, some of which are shown in *Chapter 1*, are motivated by modulated conjugation[23,24] and valence-bond charge-transfer models,[25-27] and are structurally distinct from the typical planar D-π-A architype.

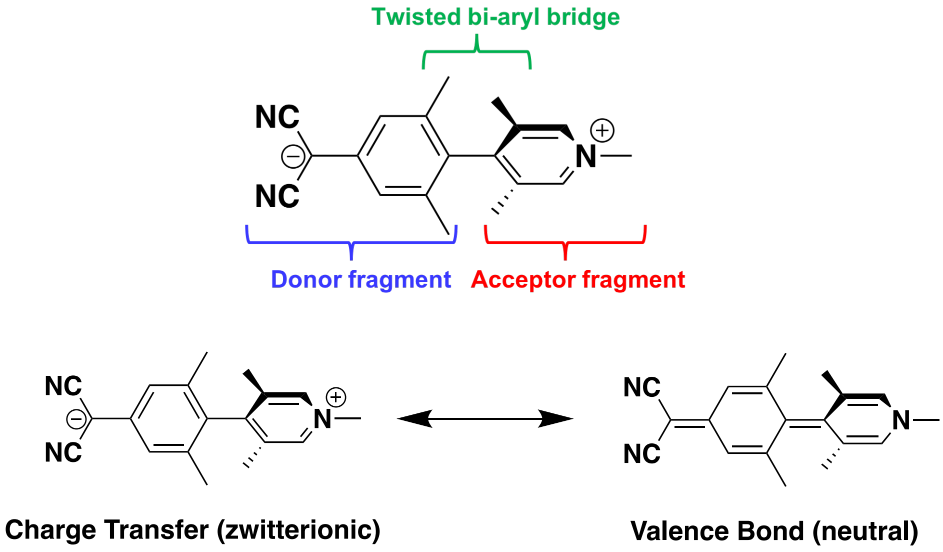

Figure 0.1. *Top*: TICT chromophore composed of anionic donor fragment, cationic acceptor fragment, and sterically enforced twisted bi-aryl bridge. *Bottom:* Charge transfer (zwitterionic) and valence bond (neutral) limiting resonance structures of twisted chromophore **TMC-2**.

Our work is focused on twisted intramolecular charge transfer (TICT) chromophores,[28-36] which are composed of a strong donor and acceptor moiety, bridged by a twisted bi-aryl fragment (Figure 0.1, *top*). A large torsional angle (generally > 70º) is enforced by steric repulsion of *ortho*-substituents on the aryl groups, and serves to isolate the donor and acceptor group, localizing nearly a full negative charge on the donor fragment. Thus, the ground state is best described by the aromatic resonance form (Figure 0.1, *bottom*), and has a very large ground state dipole moment (μ_g) of ~ 25 - 70 D.[30,33,36] The incorporation of a strongly electron accepting group, such as pyridinium or benzimidazolium leads to a relatively small excited state dipole moment, such that $\Delta\mu_{eg}$ is extraordinarily large. Experimentally, this is demonstrated by a hypsochromic shift of the CT peak in increasingly polar solvent (Figure 0.2, *left*), meaning that the large μ_g receives greater solvent stabilization than does the relatively small μ_e. The inter-aryl torsion also reduces the overlap of the donor and acceptor π-systems, resulting in low CT transition strength, generally on the order of μ_{eg} ~2 D. Increased torsion destabilizes the ground state, which in turn decreases the gap between ground and excited state energy, though experimentally it is clear that solvent stabilization reduces the magnitude of this effect.[27-30,33,36] As shown in Figure 0.2, these chromophores tend to exhibit linear optical spectra which have both the characteristic inter-fragment charge transfer (TICT) in the region of ~400-700 nm, as well as some type of strong higher-energy sub-fragment transition.

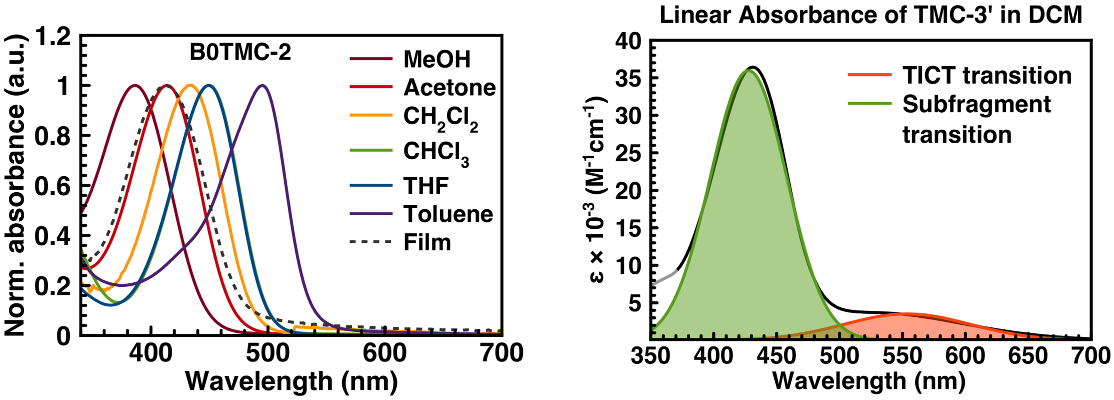

Figure 0.2. *Left*: Solvatochromic shift of the CT peak of TICT chromophore **B0TMC-2**. *Right*: Typical linear absorbance spectrum of TICT chromophore **TMC-3'** in DCM showing the weak TICT transition (orange) and stronger sub-fragment transition (green).

Several generations of TICT chromophores have been synthesized and characterized to determine β and γ (Figure 0.3), while the NLO response of many others have been explored computationally. As discussed in the sections above, the NLO-relevant parameters, μ_{eg}, $\Delta\mu_{eg}$, and E_{eg} are available from linear absorbance. However, the 2LM predicts that a molecule with typical TICT parameters $\mu_{eg} \sim 2$ D, $\Delta\mu_{eg} \sim 25$ D, and $E_{eg} \sim 2$ eV would exhibit a mundane β value of ~ 10 – 20 × 10^{-30} esu, which is much lower than the experimentally and computationally determined β values between –800 and –9800 × 10^{-30} esu.[30,33,36] So, while the 2LM is useful for outlining the relevant molecular properties, it does not accurately capture the NLO response. Valence-bond charge-transfer (VVB-CT) models provide better intuitive description of these chromophores, as described in the following section.

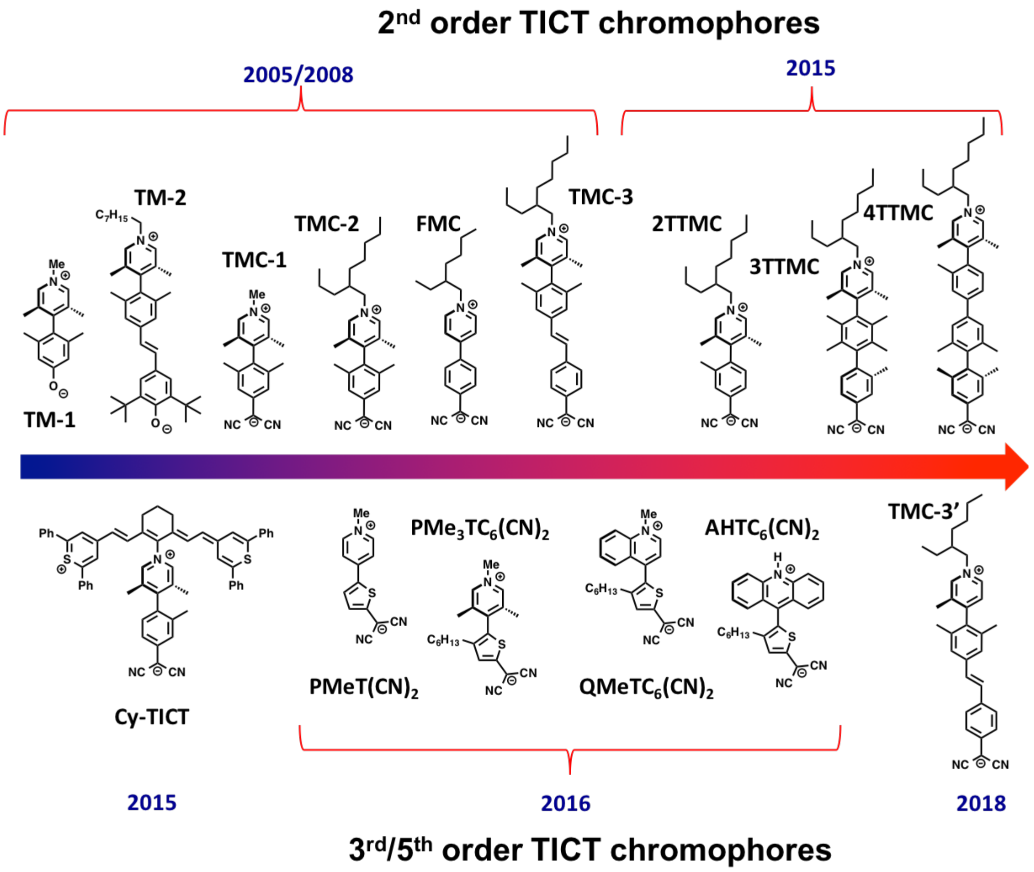

Figure 0.3. Timeline of 2nd order (*top*) and 3rd/5th order (*bottom*) TICT chromophores from references 8-14, not including structures from this work.

0.3 Valence-bond charge-transfer model of TICT chromophores. In valence-bond charge-transfer (VB-CT) models, two resonance structures are considered: a neutral "valence bond" state and a charge separated "charge transfer" state, as shown for **TMC-2** in Figure 0.1. By employing these resonance forms as the basis set of a two-state Hamiltonian, one can express the ground and excited state energy, dipole moment, and transition moments in terms of the energy between the VB and CT form (*V*, in eV), the coupling between the states (*t*, in eV) and the dipole moment of the CT state (μ, in D). These values can then be used to define the diagonal components of α, β and γ.[37]

$$\alpha_{zz} = 2t^2\mu^2/\left(\sqrt{V^2+4t^2}\right)^3 \tag{0.6}$$

$$\beta_{zzz} = 6t^2\mu^3V/\left(\sqrt{V^2+4t^2}\right)^5 \tag{0.7}$$

$$\gamma_{zzzz} = 24t^2\mu^4(V^2-t^2)/\left(\sqrt{V^2+4t^2}\right)^7 \tag{0.8}$$

This approach can directly account for torsional angle, θ, by roughly estimating that t = cos(θ)[38] such that β can be expressed as a function of θ for various values of V using eq. 0.7 (Figure 0.4). In a chemical context, θ is related to the amount of steric hindrance and environmental factors, and V depends on the electron affinity of the acceptor group, and the ionization energy of the donor moiety. From Figure 0.4, it is clear that for the appropriate donor/acceptor group pairing, β can improve by over an order of magnitude upon changing from a planar to highly twisted conformation. While this model does not exactly reproduce experimental values for TICT chromophores, it provides a sound qualitative justification of enhanced β upon twisting.

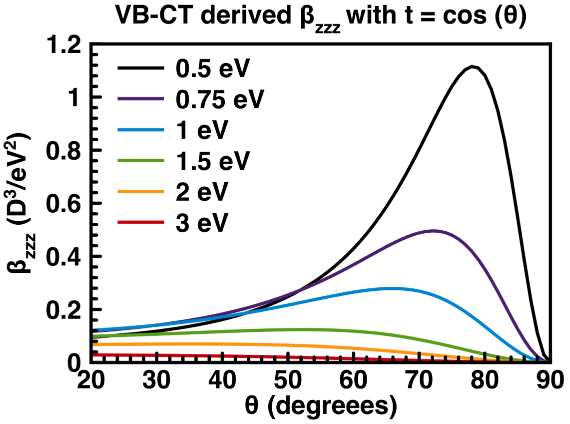

Figure 0.4. Dependence of β_{zzz} on torsional angle, modeled as t = cos(θ), with varied V from 0.5 to 3 eV and μ = 1 D.

Consistent with the simple VB-CT model, as well as recent work on modulated conjugation,[23,24] TICT chromophores exhibit some of the highest β values in open literature, several of which even approach the fundamental limits on β.[12] However, the high performance of twisted chromophores is lost in polar solvents, and aggregate formation in concentrated solutions and polymeric matrices leads to a severe reduction in β. For example, the record holding chromophore **TMC-3** exhibits $\mu\beta \sim -488{,}000 \times 10^{-48}$ esu in dilute DCM solution, $< -100{,}000 \times 10^{-48}$ esu in polar DMF solution, and in highly concentrated solution the response is essentially zero.[30] The issue of poor performance in polar solvent is addressed in *Chapter 1* through new chromophore design, and in *Chapter 2* organic salt additives are proposed to mitigate aggregation in solution and the solid state.

0.4 TICT chromophores for 3rd order NLO. 3rd order NLO materials are desirable for their nonlinear refraction, Re(γ), or nonlinear absorption, Im(γ). Im(γ) allows materials to be transparent to non-intense light, but strongly absorb intense light of the same wavelength, making them useful for optical power limiting.[39] Such materials are of critical importance for eye and sensor protection. Re(γ) causes intensity dependent changes in refractive index (the optical Kerr effect), which allows for the control of "light with light", which is useful for all-optical switching schemes.[7]

The first report of 3rd order response in TICT chromophores by He et al. showed that archetypal chromophore **TMC-2** exhibits Re(γ) = 1.4×10^{-33} esu at 800 nm, accompanied by a very small Im(γ) = 3.43×10^{-35} esu.[40] The large Re(γ)/Im(γ) ratio, and relatively large magnitude of Re(γ) indicates that TICT chromophores are good candidates for all-optical switching. Covalent coupling of **TMC-2** to cyanine dye **IR-1061** showed further synergistic enhancement of γ, though at the expense of optical transparency in the near IR region.[34] Further efforts focused on increasing the electron donating ability of the dicyanomethanide donor fragment, enhancing the acceptor group aromaticity, and reducing the torsional angle.[35] Experimental results revealed that structural changes which raised the HOMO energy resulted in large increases in NLO response, though they were accompanied by a bathochromic shift of the linear absorbance, which eroded the optical transparency window.

Re(γ) is commonly related to tunable parameters by a 3-level truncation of the SOS expression (eq. 0.9), which has three terms referred to as negative (N), dipolar (D), and two-photon (TP) reading left to right.[41] This static model does not account for resonant enhancement, though it demonstrates the continued importance of E_{01}, μ_{01}, and $\Delta\mu_{01}$. A more complete version of this expression can also account for near resonance conditions, which is critically important to balancing linear and nonlinear absorbance with Re(γ). However, eq 0.9 is adequate for describing response far from resonance.

$$\gamma = -{\mu_{01}^4}/{E_{01}^3} + {\mu_{01}^2 \Delta\mu_{01}^2}/{E_{01}^3} + {\mu_{01}^2 \mu_{12}^2}/{E_{01}^2 E_{02}} \qquad (0.9)$$

It appears that the main contribution to Re(γ) in TICT chromophores arises from the D term, as the $\Delta\mu_{01}$ is large relative to transition moments μ_{01} and μ_{12}, which could not reasonably lead to large N and TP terms. In *Chapter* 3, we extend the dipole moment of **TMC-2** by adding a stilbene fragment, in hopes of further enhancing the D term. The resulting chromophore exhibits hybrid stilbene/TICT attributes leading to higher-order NLO effects, though the computed NLO response indicates improvement in Re(γ) from the structural modification.

0.5 Magneto-electric NLO response. Historically, it was thought that the magnetic field of light could not lead to optical nonlinearities at non-relativistic intensities. However, recent evidence of magneto-electric (M-E) nonliterary in transparent, unstructured dielectrics, and subsequent development of the theory behind such effects has clearly shown that M-E effects are a relevant and unexplored branch of nonlinear optics.[9,42-46] A detailed description of M-E nonlinearity is given in *Chapter 4*, which outlines some of the first published structure-property relationships in this field.

Chapter 1. Unprecedented Large Hyperpolarizability of Twisted Chromophores in Polar Media

Reproduced with permission from:

Lou, Alexander J.-T.; Righetto, Stefania; Barger, Christopher; Zuccaccia, Cristiano; Cariati, Elena; Macchioni, Alceo; Marks, Tobin J. *Journal of the American Chemical Society* **2018**, **DOI**: 10.1021/jacs.8b04320.

The work was performed in collaboration with the co-authors listed above.

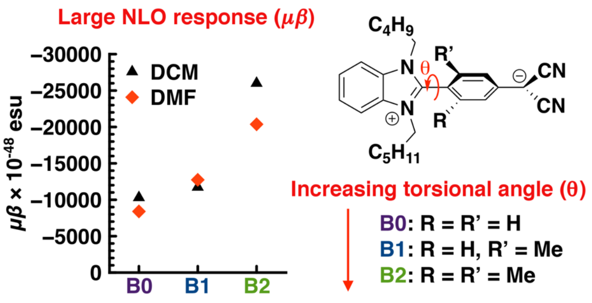

Abstract. Twisted intramolecular charge transfer (TICT) chromophores can exhibit the exceptional second order nonlinearities ($\mu\beta$) required for high-performance electro-optic (E-O) materials. However, in low-polarity solvents, centrosymmetric aggregate formation reduces $\mu\beta$ dramatically, while TICT chromophores in de-aggregating polar solvents suffer decreased response from environmentally driven changes in electronic structure. Here we report a series of benzimidazolium-based TICT chromophores with inter-aryl torsional angles between 64-77°. The most twisted of these, **B2TMC-2**, exhibits a large $\mu\beta_{\mathrm{vec}} = -26{,}000 \times 10^{-48}$ esu in dilute non-polar solution (1907 nm), and a similarly large $\mu\beta_{\mathrm{vec}} = -20{,}370 \times 10^{-48}$ esu in polar solvent as measured by DC electric-field induced second harmonic generation (EFISH). Sterically enforced inter-aryl torsional angles are observed by single crystal X-ray diffraction and solution phase Nuclear Overhauser Effect (NOE) NMR, and spectroscopic characterization reveals a zwitterionic/aromatic ground state electronic structure associated with the high $\mu\beta$. We show that increasingly disrupted conjugation is correlated with increased $\mu\beta$, even at intermediate twist angles. The excellent performance and reduced aggregation in polar solvents opens new avenues for bridging microscopic and macroscopic performance of these chromophores.

1.1 Introduction. Second order organic nonlinear optical (NLO) materials are of great interest for their ability to generate, process, and switch optical signals for applications such as image reconstruction and optical telecommunication.[11,12] In order to create useful optoelectronic devices, the constituent organic chromophores must possess a large molecular hyperpolarizability ($\mu\beta$), optical transparency, chemical and thermal stability, and be effectively incorporated into device-ready materials. To date, organic materials have demonstrated excellent electro-optic coefficients in excess of 100 pm/V, as compared to 32 pm/V in the ubiquitous inorganic device material,

$LiNbO_3$.[12,30,47-50] Organic molecules have the attraction of being readily tuned structurally and electronically, and chromophores with large $\mu\beta$ can be rationally designed using structure-property relationships developed over several decades.

In the past, the majority of second order NLO designs have followed a simple paradigm in which the chromophores are composed of donor and acceptor functionalities, bridged by a planar π-system. These "push-pull" systems typically possess a low-lying strongly polarized, charge transfer (CT) state, and can therefore be described by the simple "two-state model", which provides a qualitative relationship between β and tunable molecular properties (eq. 1.1).[10] Here β is related to the CT energy (E_{eg}), transition dipole moment (μ_{eg}), and the change in state dipole moment ($\Delta\mu_{eg} = \mu_e - \mu_g$).

$$\beta = \frac{\Delta\mu_{eg}\mu_{eg}^2}{E_{eg}^2} \qquad (1.1)$$

Another approach, known as bond-length alternation (BLA), manipulates the contributions of CT limiting resonance forms to the ground state electronic structure in order to enhance $\mu\beta$.[20,51,52] BLA based chromophores (see **CLD-1**, Figure 1.1) generally contain donor and acceptor groups bridged by extended, planar, polyene backbones. Such structures have been critical to the elucidation of structure-property relationships and can exhibit $\mu\beta$ in excess of $17,600 \times 10^{-48}$ esu.[53] However, these BLA chromophores are often limited by photochemical and oxidative instability and rely on low-lying CT states which erode the optically transparent window in the near IR.[53,54] Other approaches such as multi-dimensional chromophores,[55,56] modulated conjugation,[24] and auxiliary donor/acceptors[57] have also afforded promising increases in hyperpolarizability.

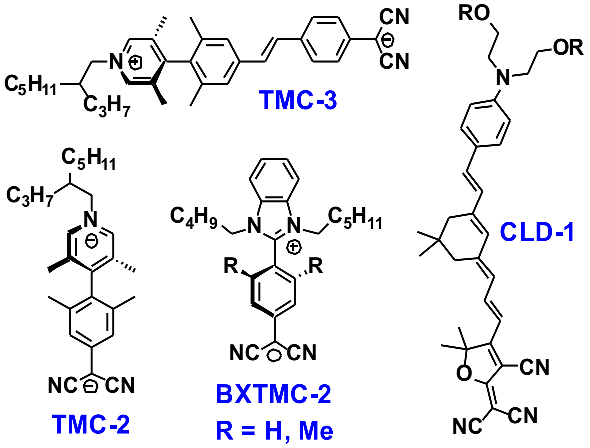

Figure 1.1. TICT chromophores **TMC-2** and **TMC-3**, BLA inspired **CLD-1**, and **BXTMC-2** chromophores in this work.

In 1997, Albert et al. challenged the notion that planarity was a prerequisite to large $\mu\beta$, suggesting that a twisted intramolecular charge transfer (TICT) chromophore could surpass previous efforts.[28] Following this report, TICT chromophore **TMC-3** was experimentally shown to exhibit $\mu\beta_{vec} = -488{,}000 \times 10^{-48}$ esu (in dilute DCM solution) (Figure 2),[28-31,33,36] exceeding the previous best $\mu\beta$/MW by a factor of ~20×, and approaching the fundamental limits on β proposed by Kuzyk et al.[12] The exceptional NLO response stems from a twisted bi-aryl bridge fragment and aromatic stabilization of the charge separated ground state, which leads to a low-lying CT (small E_{eg}) and large $\Delta\mu_{eg}$.[27] Further experimental work on TICT chromophores focused on, (1) the impact of torsional angle;[36] (2) adding multiple twisted fragments;[33] (3) extending the conjugation.[30]

Nevertheless, while the NLO response of TICT chromophores is extraordinarily high in dilute, non-polar solution, these chromophores suffer from dipole driven aggregation, yielding anti-parallel dimers for which $\mu\beta = 0$.[30] This tendency poses a challenge when attempting to translate solution phase properties to host-guest polymer matrices, where high effective chromophore concentration is required for useful bulk response.[30,31] While polar environments can provide stabilizing interactions which disrupt aggregate formation, they also severely depress the NLO response of the aforementioned TICT chromophores. For example, at low concentrations, the maximum $\mu\beta_{\mathrm{vec}}$ of **TMC-3** in polar DMF is about 1/5 of that in DCM (Figure 1.2).[31]

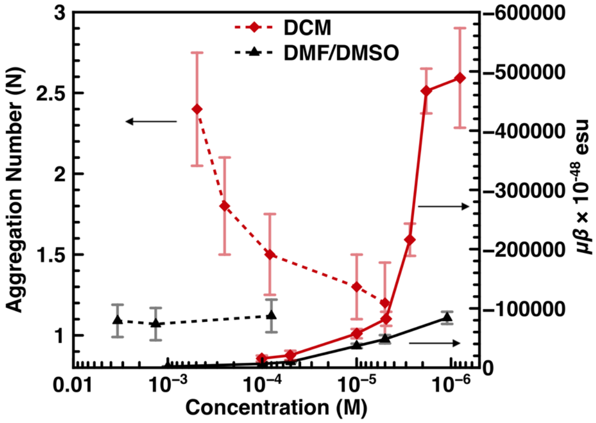

Figure 1.2. EFISH derived $\mu\beta_{\mathrm{vec}}$ (solid lines) and PGSE NMR-derived aggregation number (dotted lines) of **TMC-3** as a function of concentration in DCM (red diamonds), DMSO-d$_6$ (black dotted line), and DMF (solid black lines). Figure reproduced from Ref. 31.

The desire to translate molecular performance to bulk has been a long-standing goal within the community; past approaches include Langmuir-Blodgett films, polled polymers, layer-by-layer self-assembly, modification of the dielectric environment, and co-chromophore incorporation.[10,11,18,58-60] However, as we will discuss herein, structural modification of the chromophores themselves is, in this case, a necessary and productive strategy.

In the present study, we substitute the pyridinium acceptor fragment in **TMC-2** with a benzimidazolium acceptor, leading to changes in electronic structure and allowing the strategic placement of two sterically demanding alkyl substituents. The steric interaction of these alkyl substituents with *ortho*-methyl groups creates a significant twist angle between the donor and acceptor π-ring planes. The new **BXTMC-2** family (Scheme 1.1) exhibits excellent stability, solubility, and NLO performance. We show that unlike previous TICT generations, these chromophores perform well in polar media, opening routes towards device incorporation which were previously unavailable for TICT chromophores. Furthermore, we characterize the key structural properties of these systems and use this information to augment previous observations of NLO response in relation to disrupted conjugation and intrinsic chromophore efficiency.

Scheme 1.1. Synthesis and structures of BXTMC-2 chromophores.

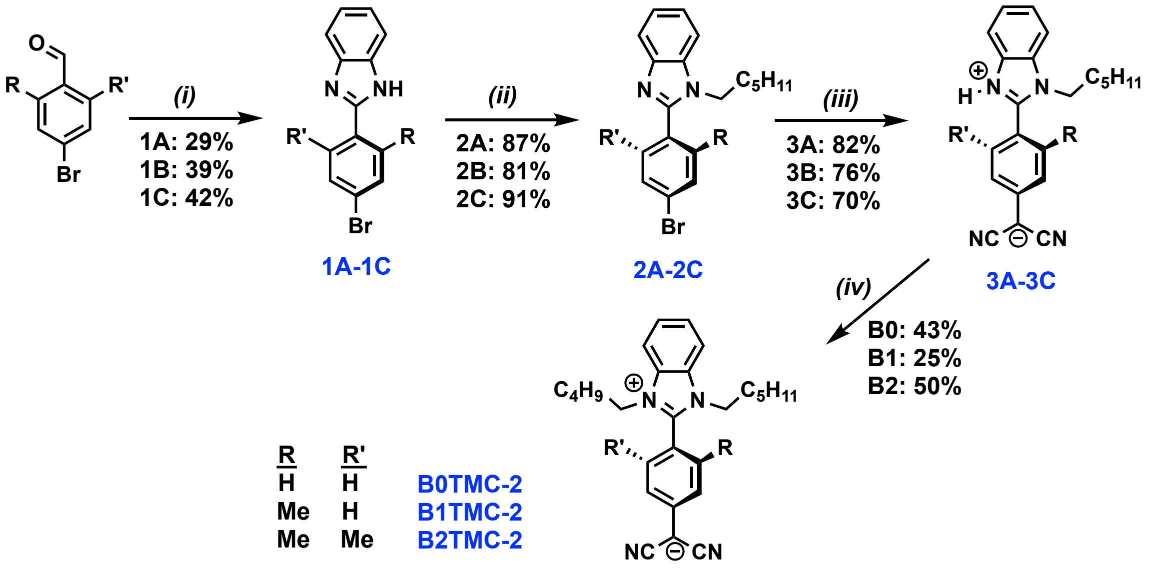

*Reagents and conditions: *(i)* phenylenediamine, 1,4-dioxane, bubbling air at 85° C; *(ii)* KO^{t}Bu, $C_6H_{13}Br$, KI (cat.), THF 60° C; *(iii)* malononitrile, NaO^{t}Bu, $Pd(PPh_3)_4$, DME, 85° C; *(iv)* KO^{t}Bu then $C_5H_{11}OTf$ in acetone at 0° C.

1.2 Results. Having synthesized a series of benzimidazolium based TICT chromophores with varied expected torsional angles, we investigate their solid state and solution phase properties. Particular attention is paid to changes accompanying increased steric encumbrance, and to the relationship of **BXTMC-2** to **TMC-2**. Single crystal X-ray diffraction and NMR spectroscopy are used to determine the molecular geometry, including the bi-aryl torsional angle. Linear optical absorbance in a range of solvents, vibrational spectroscopy, and electrochemical measurements provide a detailed description of the electronic structure and the environmental dependence thereon. Nonlinear optical measurements using DC electric-field induced second harmonic generation (EFISH) are then used to determine $\mu\beta_{\mathrm{vec}}$ and to assess aggregation tendencies.

1.2.1 Synthesis of BXTMC-2 chromophores. The synthesis of the **BXTMC-2** family (Scheme 1.1) begins with condensation of phenylene diamine with the desired 4-bromo-benzaldehydes in the presence of air to form intermediates **1A-1C**. The acidic protons are then removed, and selective *N*-alkylation is performed with 1-bromohexane. The aryl bromides in molecules **2A-2C** can be efficiently converted to the corresponding dicyanomethanide functionalities via a Pd-catalyzed coupling with malononitrile. The products of this reaction (**3A-3C**) appear by NMR to be the zwitterionic isomer, where the acidic malononitrile proton migrates to the benzimidazole ring. As such, it is then necessary to treat structures **3A-3C** with base prior to alkylation to yield the final **BXTMC-2** products, and to perform alkylation at low temperature to ensure selectivity. The identity and purity of the final products was confirmed by a standard battery of spectroscopic and physical methods as described below.

1.2.2 BXTMC-2 solution structures by ^{1}H and ^{15}N NMR. ^{1}H NMR spectra of the **BXTMC-2** chromophores in DMSO-d$_6$ (Figure 1.3) shows two sets of signals in the aromatic region; (1) resonances at $\delta_H = 7.6 – 8.2$ ppm associated with the electron-deficient benzimidazolium acceptor fragment; (2) and signals at $\delta_H = 6.6 – 7.5$ ppm for the electron-rich aryl donor fragment. H$_c$ in DMSO-d$_6$ shifts to higher field with increased bi-aryl torsion, from **B0TMC-2** ($\delta_H = 6.97$ ppm) to **B1TMC-2** ($\delta_H \sim 6.82$ ppm) and **B2TMC-2** ($\delta_H = 6.68$ ppm) indicating an increased electron-richness in that molecular fragment. Both increasing the NOE NMR determined twist angle (see more below) and addition of electron donating methyl groups likely contribute to these shifts. The acceptor peaks (H_e, H_f) do not appear to be very sensitive to such changes, and exhibit $\Delta\delta_H < 0.1$ ppm between **B0-** and **B2TMC-2**.

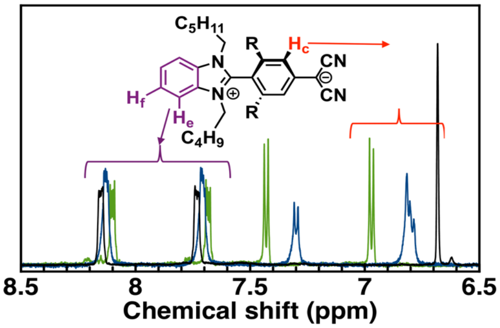

Figure 1.3. ^{1}H NMR spectra of **BXTMC-2** in DMSO-d$_6$: **B0TMC-2** (green), **B1TMC-2** (blue) and **B2TMC-2** (black). Peaks related to H_c are bracketed in red; H_e and H_f are in purple.

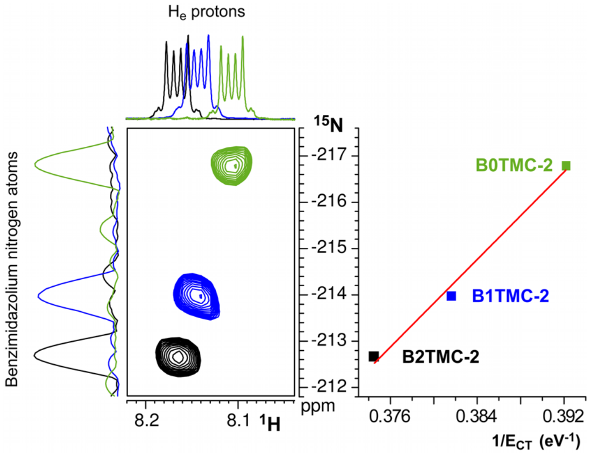

Figure 1.4. *Left*: Superimposed ^{1}H,^{15}N HMBC NMR spectra of **BXTMC-2** in DMSO-d$_6$. *Right*: Trend of δ_{15N} (ppm) as a function of the inverse of the HOMO-LUMO energy gap (1/E_{CT}).

In contrast to the above ^{1}H aromatic chemical shift trends, the ^{15}N chemical shifts (δ_{15N}) of benzimidazolium resonances (Figure 1.4, left) are displaced significantly and systematically within the **BXTMC-2** series, with δ_{15N} increasing from **B0-** (-216.8 ppm) to **B1-** (-214.0 ppm) and **B2TMC-2** (-212.7 ppm). The observed δ_{15N} trend reasonably reflects increasing accumulation of positive charge at the benzimidazolium nitrogen atoms on progressing from **B0TMC-2** to **B2TMC-2,**[61-63] and indicates an increasing contribution of the aromatic resonance form to the ground-state structure.[64,65] This is consistent with an increased de-shielding along the series as demonstrated by the linear shift of δ_{15N} with trends in the HOMO-LUMO energy gap (E_{CT}, Table 1.2), according to the Ramsey equation (Figure 1.4, right).[66-68] Comparison of relative δ_{15N} values indicates a larger variation of the bi-aryl torsion between **B0-** and **B1TMC-2** than between **B1-** and **B2TMC-2**, in agreement with NOE data (see below).

1.2.3 Crystallographic characterization of BXTMC-2 chromophores. Single crystal diffraction characterization provides insight both into the molecular geometries of the chromophores, as well as the modes of solid state intermolecular interactions operative (Figures 1.5 and 1.6). Large bi-aryl torsional angles of 70, 89, 79 are observed for **B0-**, **B1-**, and **B2TMC-2** respectively, confirming the steric contribution of both H/CH_2 and CH_3/CH_2 repulsions. Two key bond distances are also examined (Figure 1.5). First, the bridging (ring)C-C(ring) bond distance is 1.465(4), 1.474(8), and 1.478(4) Å for **B0-**, **B1-**, and **B2TMC-2**, respectively. The (ring)C-C(ring) bond lengths are more similar to those observed for bi-mesitylene (1.501 Å)[69] and bi-aryls (1.487 Å)[70] than typical C=C bonds (~1.33 Å),[71] indicating that all three molecules are best described by linked aromatic structures rather than as quinones. The lengthening which accompanies added methyl groups likely results both from torsion, which reduces double bond character, and steric repulsion. Structural data are summarized in Table 1.1.

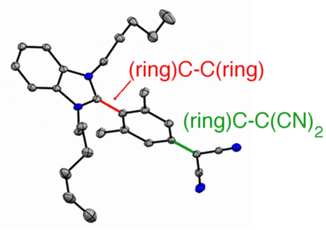

Figure 1.5. ORTEP drawing of chromophore **B2TMC-2** with 30% probability ellipsoids showing key bond metrical parameters.

The second key bond distance, (ring)C-C(CN)$_2$, is found to be 1.445(4), 1.438(8), and 1.450(4) Å for **B0**-, **B1**-, and **B2TMC-2** respectively (Table 1.1). These values are longer the analogous bond lengths found in quinoidal TCNQ (1.373 Å),[72] suggesting that the dicyanomethanide group supports significant negative charge. The increase in bond length between **B1-** and **B2TMC-2** is indicative of increased aromatic character, consistent with the observed lengthening of the ring(C)-(C)ring bond. The similarity of **B0-** and **B1TMC-2** ring(C)-C(CN)$_2$ distances may be a coincidental result of different packing structures; **BoTMC-2** exhibits close contact between donor and acceptor of adjacent molecules potentially stabilizing the negative charge.

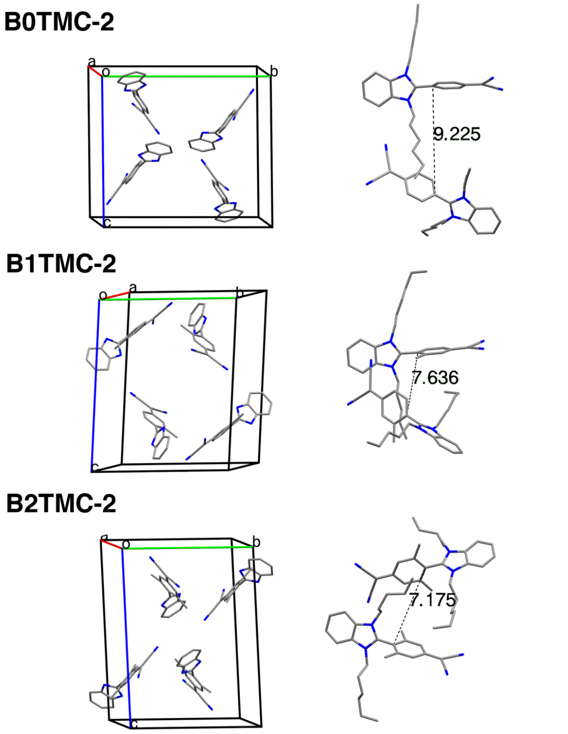

Figure 1.6. Crystal structures of the **BXTMC-2** chromophore series. *Left*: packing of the tetrameric centrosymmetric unit cells (alkyl groups excluded for clarity). *Right*: Closest packed dimeric structures with relevant packing distances measured in Å.

Table 1.1. Crystallographic bond and intermolecular packing distances

	Distance (Å)			
	(ring)C-C(ring)	(ring)C-C(CN)$_2$	Packing distance	Bi-aryl torsion
B0TMC-2	1.465(4)	1.445(4)	9.225(6)	70
B1TMC-2	1.474(8)	1.438(8)	7.636(8)	89
B2TMC-2	1.478(4)	1.450(4)	7.175(4)	79

The **BXTMC-2** crystal structures all exhibit anti-parallel dimer packing within the centrosymmetric tetramers which constitutes the unit cell (Figure 1.6). The distance between the bridging carbon on the donor ring of the anti-parallel aligned pairs provides an estimate of the closeness of the intermolecular interaction. This distance contracts on progressing from **BoTMC-2** (9.220(6) Å) to **B1TMC-2** (7.636(8) Å) and **B2TMC-2** (7.175(4) Å), suggesting stronger intermolecular interactions, particularly in **B2TMC-2**. This trend is in agreement with a computed increase in ground state dipole moment, which is likely a driving force in these interactions. There is no evidence of co-crystalized solvent associated with these structures, and the unit cells lack solvent accessible voids.

1.2.4 Nuclear Overhauser effect (NOE) NMR characterization of chromophore structures in solution. ^{1}H-^{1}H NOE NMR experiments, which measure through space dipolar coupling, were undertaken in DMSO-d$_6$ to estimate the average twist angle in solution for the **BXTMC-2** chromophore series. For **B2TMC-2**, NOE measurements were carried out by irradiating the Me singlet (δ_H = 1.93 ppm at 298K) and measuring NOEs at both H_a and H_c (Scheme 1.2). For **B0TMC-2**, the H_d doublet (δ_H = 7.44 ppm at 298K) was irradiated and NOEs were measured on H_a. In the case of **B1TMC-2** both the Me singlet (δ_H = 2.02 ppm at 298K) and the H_d doublet (δ_H = 7.31 ppm at 298K) were irradiated, and the following NOEs were quantified: Me-H_c, Me-H_a, and H_d-H_b. From the measured NOEs, average values of cross relaxation rate constants ($<\tau_{IS}>$)[73] at different temperatures and average internuclear distances $<r_{IS}>$[74] were obtained using the methodology described previously.[30]

Scheme 1.2. **BXTMC-2** chromophore structures and labeling scheme showing *syn* and *anti* configurations.

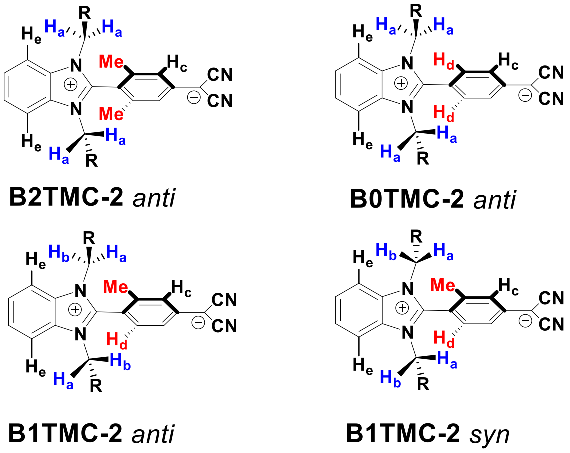

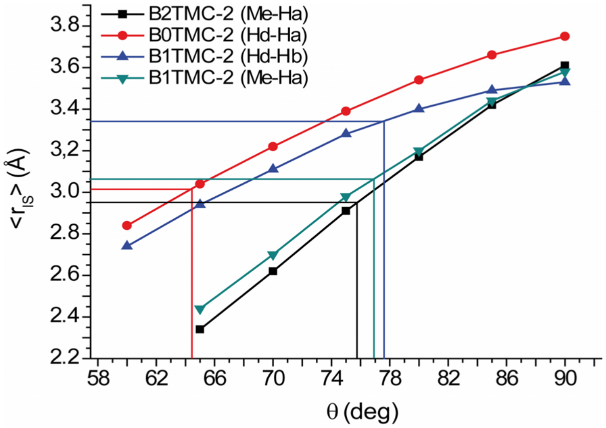

Figure 1.7. Computed average distance $<r_{IS}>$ for **B0TMC-2** (H_d-H_a), **B1TMC-2** (Me-H_a and H_d-H_b) and **B2TMC-2** (Me-H_a) chromophores in the solid state as a function of dihedral twist angle (θ). The cross points indicate the experimentally NOE-derived distances and the corresponding average twist angle in solution.

In order to correlate the average internuclear distance measured in solution between aromatic (Me or H_d groups) and benzimidazole (H_a and H_b protons) moieties with the average twist angle (θ) in solution, average internuclear distances were computed, under r_{IS}^{-6} averaging,[75] for seven static conformations (θ approximately equal to 60°, 65°, 70°, 75°, 80°, 85° and 90°) starting from the solid state X-ray structures of the **BXTMC-2** series. Considering the simplified approach, the computed average distances, reported in Figure 1.5, are somewhat biased toward shorter distances (i.e., toward the distance of closest approach); consequently, the derived twist angles in solution (cross points in Figure 1.5) are somewhat underestimated, and should be better considered as a lower limit for θ. There is no doubt that **B0TMC-2** exhibits the smallest twist angle (64°) in solution (Figure 1.7). However, **B1-** and **B2TMC-2** are found to have very similar twist angles (77-78° and 76°, respectively), according to the present analysis. From this analysis, it is clear that both Me/CH_2 and H/CH_2 interactions play a significant role in bi-aryl torsion. The similarity of the **B1-** and **B2TMC-2** torsional angles is addressed in the discussion section.

1.2.5 Infrared (FTIR) vibrational spectroscopy. **BXTMC-2** compounds were characterized by FTIR both as solids and in DCM solution. The key feature of these spectra is the characteristic C≡N stretching, ν(C≡N), with a lower energy side component, presumably the symmetrically and anti-symmetrically coupled modes (Figure 1.8). In the solid state, **B1-** and **B2TMC-2** exhibit ν(C≡N) = (2168, 2133 cm^{-1}) while **B0TMC-2** exhibits a slightly higher energy side band at 2128 cm^{-1}. The energy and splitting of the bands is similar to a phenyl malononitrile anion (ν(C≡N) = 2163, 2117 cm-1),[76] indicating that the dicyanomethanide groups in **BXTMC-2** bear a large amount of electron density.

In solution, all **BXTMC-2** chromophore molecules display significantly higher energy ν(C≡N) stretching modes than as solids, and ν(C≡N) falls in energy from **B0-** (2176 cm^{-1}) to **B1**- (2174 cm^{-1}) and **B2TMC-2** (2172 cm^{-1}). This trend indicates a slight increase in electron density on the dicyanomethanide group accompanying the addition of methyl groups. The low energy side band is also higher in energy than in the solid state (2139 cm^{-1} for all compounds). These observations suggest that the **BXTMC-2** chromophores exhibit predominantly zwitterionic character both in solution and solid state.

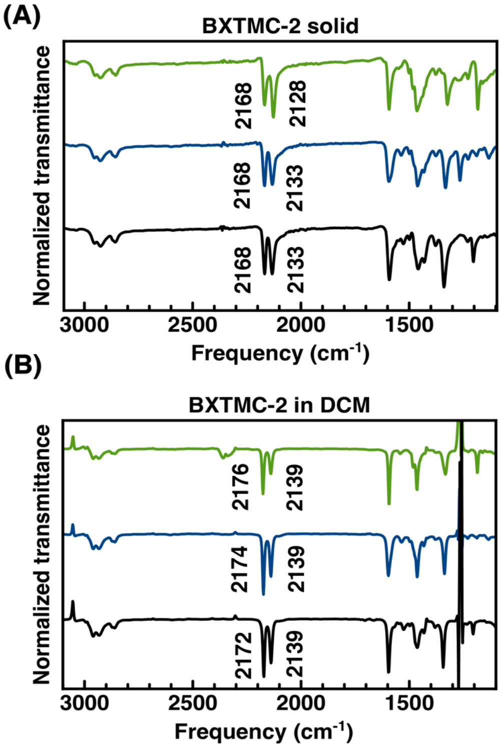

Figure 1.8. FTIR vibrational spectra of **B0TMC-2** (green), **B1TMC-2** (blue), and **B2TMC-2** (black); (A) solid (ATR); (B) DCM solution.

1.2.6 Linear optical absorption spectroscopy as a function of solvent. The solution optical absorption of the **BXTMC-2** family (Figure 1.9A) all exhibit a broad low-lying charge transfer (CT) absorption (434 nm – 408 nm) and a higher energy transition (315 nm – 328 nm). The intensity of the CT peak decreases from $\varepsilon = 24{,}928\ M^{-1}cm^{-1}$ in **BoTMC-2** to $\varepsilon = 8156\ M^{-1}cm^{-1}$ in **B2TMC-2**. Such reduction in transition intensity suggests increasingly disrupted conjugation, which is in agreement with reduced NOE and crystallographic torsional angles for **B0TMC-2**, but not for **B1** and **B2TMC-2**. This discrepancy is addressed in detail in the Discussion Section. By integrating the CT peaks, one can also extract transition moments (μ_{eg}), which reveal relatively large transition strengths of 5.45 D in **B0TMC-2** and 3.43 D in **B2TMC-2** as compared to 2.1 D in **TMC-2** (Table 1.2). The fall in transition intensity is accompanied by a ~27 nm hypsochromic shift from **B0TMC-2** to **B1TMC-2** to **B2TMC-2** in DCM. The higher energy excitation, attributed to a sub-fragment transition, also undergoes a ~13 nm bathochromic shift, along with a slight increase in transition strength from **B0TMC-2** to **B2TMC-2**. The behavior in Figure 1.9A is typical of TICT chromophores; as conjugation is disrupted, both sub-fragments of the molecule become isolated and their own characteristic transitions begin to dominate.[36]

Table 1.2. **BXTMC-2** optical absorption and electrochemical data.[a]

	λ_{CT} (nm)	E_{CT} (DCM[f]) (eV)	$\Delta\lambda$ (nm)[h]	E (ACN)[g]		μ_{eg}(D)[d]	μ_g(D)[b]	$\Delta\mu_{eg}$(D)[c]
				E_{ox} (V)	E_{red} (V)			
B0TMC-2	434	2.55	-64	0.24	-1.94	5.45	21.2	-12.3
B1TMC-2	415	2.62	-65	0.36	-2.03	4.72	23.5	-13.0
B2TMC-2	408	2.67	-57	0.34	-2.10	3.43	24.6	-13.7
TMC-2[e]	556	2.18	~-180	0.39	-1.56	2.10	29.8	-21.4

[a]All values reported are measured in DCM solution except where noted otherwise. [b] calculated using CAM-B3LYP/6-31G**. [c] extracted from linear absorption using the McRae equation, see SI for details. [d] extracted from linear absorption, see SI for details. [e] data from ref. 5. [f] optical HOMO-LUMO gap estimated from onset of CT absorption [g] measured from signal onset [h] Solvent shift from $CHCl_3$ to MeOH

Solvent-dependent spectra (Figure 1.9B) reveal negative solvatochromic shifts of the CT band, meaning that CT energy (E_{CT}) increases with solvent polarity (the shift between MeOH and $CHCl_3$ is reported as $\Delta\lambda$ in Table 2). Such shifts indicate that the ground state dipole moment is larger than that of the first excited state ($\Delta\mu_{eg} < 0$), and therefore is stabilized by the increase in solvent polarity. The value of E_{CT} is determined by Gaussian fitting of the CT peak to deconvolute from the sub-fragment transition (Table 1.2). The McRae equation then provides a simple means to calculate $\Delta\mu_{eg}$ by plotting the change in E_{CT} in various solvents against a solvent polarity function $f(\varepsilon, n)$.[77-79]

$$v - v_0 = -m \times f(\varepsilon, n^2) \tag{1.2}$$

Here n is refractive index and ε is the solvent dielectric constant, and $v - v_0$ is the difference between the CT frequency (in cm^{-1}) in a given solvent and in vacuum. By relating the slope, m, to $\Delta\mu_{eg}$, an increase in $\Delta\mu_{eg}$ from -12.3 D in **B0TMC-2** to -13.7 D in **B2TMC-2** is calculated (Table 1.2). UV-Vis absorption spectra of neat films are found in all cases to be similar to those in acetone solution, demonstrating that the molecules behave comparably as solids and in relatively polar solutions.

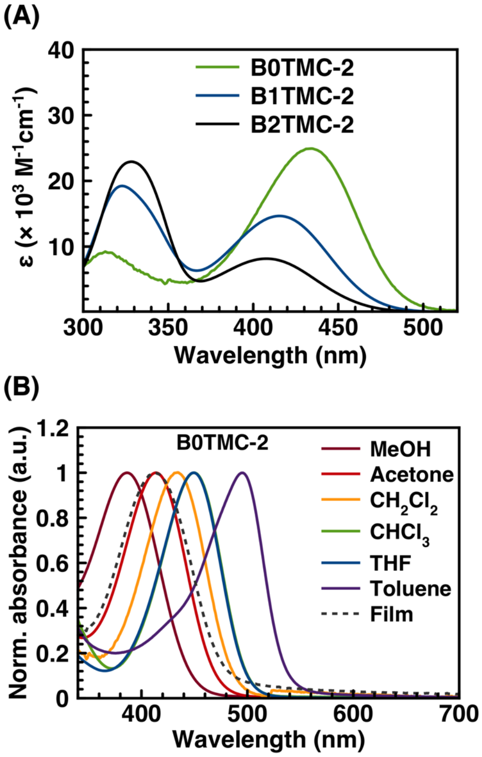

Figure 1.9. UV-Vis linear optical absorption spectra of **BXTMC-2** chromophores. (A) **BXTMC-2** chromophores in DCM solution; (B) **B0TMC-2** in the indicated solvents and as film.

1.2.7 BXTMC-2 cyclic voltammetry. Chromophores **B1-** and **B2TMC-2** exhibit reversible reduction at -2.03 and -2.10 V, respectively, while the reduction of **B0TMC-2** is irreversible at -1.94 V (Table 1.2). Oxidation is irreversible for all chromophores, with an onset between 0.24 – 0.36 V. From the oxidation and reduction potentials, the HOMO-LUMO gaps are estimated to be 2.18, 2.39, and 2.44 eV for **B0-**, **B1-**, and **B2TMC-2,** respectively; on average ~0.3 eV lower than the optical E_{CT}, possibly reflecting some mixed character in the optical transitions and solvation reorganization in redox processes.[80]

1.2.8 NLO measurements. Measurements of $\mu\beta_{vec}$, the product of the chromophore dipole moment (μ) and the vector part of the molecular first-order hyperpolarizability β_{vec} tensor along the μ direction, were performed by the solution-phase DC EFISH method, which provides direct information on the intrinsic molecular nonlinear optical (NLO) response via eq. 1.3.

$$\gamma_{EFISH} = (\mu\beta/5kT) + \gamma(-2\omega; \omega, \omega, 0) \tag{1.3}$$

Here, $\mu\beta/5kT$ is the dipolar orientational contribution, and $\gamma(-2\omega;\omega,\omega,0)$, the third-order term at frequency ω of the incident light, is the electronic contribution to γ_{EFISH}, which is negligible for molecules of the type investigated here.[81] EFISH measurements at 1907 nm were performed over a concentration range in DCM and DMF to determine, (1) trends in the monomeric response of the **BXTMC-2** chromophores in highly dilute solutions; (2) the dependence on solvent environment; (3) the effect of aggregation in different solvent environments. It is well known that highly polar TICT chromophores have a strong tendency to aggregate in solution,[30] so the most dilute reliable measurement for each chromophore was taken to be representative of monomeric $\mu\beta_{vec}$. Note that this value reflects the lower bound of $\mu\beta_{vec}$, particularly in the case of **B1TMC-2** for which larger values were recorded at higher dilution but with greater uncertainty. Measurements in DCM reveal very large monomeric $\mu\beta_{vec}$= -26,000×10^{-48} esu for **B2TMC-2**, and $\mu\beta_{vec}$ of -11,730 and -10,300×10^{-48} esu for **B1TMC-2** and **B0TMC-2** respectively (Figure 1.10A). The response of **B2TMC-2** is on the order of the monomeric response of **TMC-2** (Figure 1.1; $\mu\beta_{vec}$=-24,000×10^{-48} esu), despite increases in E_{CT} and a reduced $\Delta\mu_{eg}$.

EFISH measurements on **B2TMC-2** solutions in polar DMF (Figure 1.10B) reveal an NLO response of $\mu\beta_{vec}$= -20,370×10^{-48} esu, which is similar to the measured value in DCM, and about 4× higher than **TMC-2** (-5,620×10^{-48} esu) under the same conditions. **B1TMC-2** shows a similarly high value of $\mu\beta_{vec}$= -12,740×10^{-48} esu in DMF compared to -11,730×10^{-48} esu in DCM (Table 1.3). These observations are in sharp contrast to all previous TICT chromophores, which suffer massively decreased NLO responses in polar solvents (Figures 1.1 and 1.10B).

With the exception of **B0TMC-2**, a significant decrease in $\mu\beta_{vec}$ is observed with increasing concentration in the range of 10^{-5} – 10^{-3} M in DCM. This behavior is consistent with the formation of centrosymmetric aggregates (for which $\mu\beta_{vec}$ = 0), and mirrors previous observations on **TMC-2** in DCM (Figure 1.10). The concentration dependence of NLO response is much more pronounced in the most twisted chromophore (**B2TMC-2)** than in the least twisted (**B0TMC-2)**, likely reflecting the dipole moment enhancement which accompanies bi-aryl torsion. The use of more polar DMF appears to mitigate these effects, and shifts the decreases in NLO response towards higher concentrations (Figure 1.10B).

Table 1.3. EFISH results for **BXTMC-2** chromophores in DCM and DMF at 1907 nm

	μB (esu × 10^{-48})[a]		β (esu × 10^{-30})[b]	
	DCM	DMF	DCM	DMF
B0TMC-2	-10,300	-8,400	-486	-396
B1TMC-2	-11,730	-12,740	-499	-542
B2TMC-2	-26,000	-20,370	-1,056	-828
TMC-2[c]	-24,000	-5,620	-805	-189

[a] Highest dilution with reliable data is used to estimate $\mu\beta_{\text{vec}}$. [b] calculated using DFT derived dipole moments in Table 1. [c] data from ref. 5.

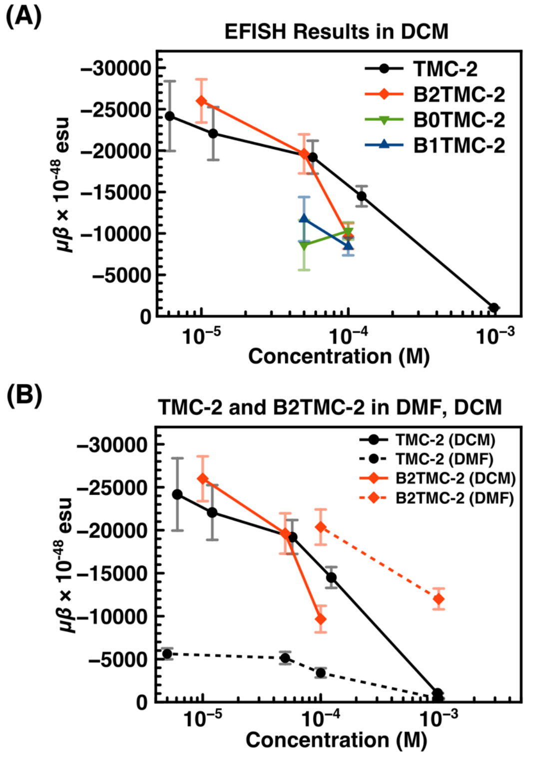

Figure 1.10. EFISH measurements of **BXTMC-2** chromophores at 1907 nm (A) in DCM, with **TMC-2** data from ref. 5; (B) comparison of $\mu\beta$ in DCM (solid lines) and DMF (dashed lines) for **B2TMC-2** and **TMC-2**.

1.3 Discussion.

1.3.1 Synthesis of the BXTMC-2 family. The synthetic route in Scheme 1 used to create **BXTMC-2** chromophores offers some significant advantages over the previous generations; (1) the final product here can be obtained in only 4 steps; (2) there is an opportunity to introduce asymmetric or functionalized sidechains; (3) introduction of the steric bulk in two separate steps leads to high yields and a further degree of synthetic flexibility. By forming the benzimidazolium acceptor group via annulation rather than coupling, we avoid repeated use of aryl halide functionality, significantly reducing the number of required synthetic steps. Furthermore, **BXTMC-2** family exhibits excellent thermal stability, with thermogravimetric analysis derived decomposition temperatures in excess of 310 °C (Figure S1.5).

1.3.2 BXTMC-2 electronic structure. The ground state electronic structure of **BXTMC-2** chromophores can be represented as a hybrid of aromatic and quinoidal resonance forms (Figure 1.11). As shown in the Results section, all three **BXTMC-2** chromophores are best described by some mix of zwitterionic/aromatic (ZA) and quinoidal/neutral (NQ) structures. The crystallographic (ring)C-C(ring) bond lengths are similar to those found in bi-aryls and bi-mesitylene, and vibrational frequencies of the $C(CN)_2$ group show that the donor group bears an

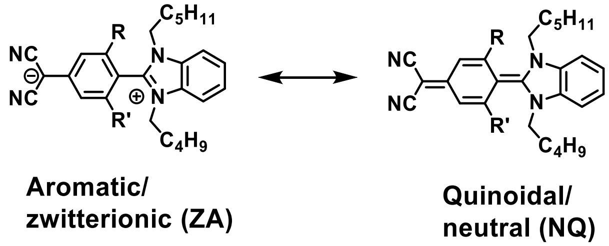

Figure 1.11. Quinoidal and aromatic contributions to the **BXTMC-2** electronic structure.

essentially full negative charge. This is consistent with previous work by Isborn et al., which notes that even at modest twist angles, aromatic stabilization of the donor and acceptor imparts dominant ZA character in similar molecules.[82] However, there is also evidence here supporting a subtle increase in ZA character from **B0-** to **B1-** and **B2TMC-2**. Shifts of the ^1H and ^{15}N NMR resonance positions, increased solvatochromic shifts, lengthening of crystallographically derived (ring)C-C(ring) bond distances, and increased $\nu(C{\equiv}N)$ energies support the trend in ZA character increasing in the progression, **B0-** < **B1-** < **B2TMC-2**.

While both crystallographic and NOE characterization data definitively show that Me/CH_2 interactions lead to larger twist angles (θ) than do H/CH_2, they also indicate similar θ for **B1-** and **B2TMC-2**. This is in contrast to the decrease in the measured CT transition moment (μ_{eg}) for **B2-** versus **B1TMC-2**, which suggests a reduction of conjugation. The reason for this observed discrepancy may relate to the dynamic nature of θ. Although the two chromophores have similar average θ by NOE, they are able to access a range of θ through thermal excitation of the vibrational ring-twisting mode. As added Me/CH_2 interactions are shown to increase twisting, it is reasonable that **B2TMC-2**, with twice the steric resistance, is less able to access smaller θ values than **B1TMC-2** at a given temperature. So, despite having similar average θ, thermal energy more easily populates less twisted configurations with large μ_{eg} for **B1TMC-2**, leading to larger observed CT absorption than for **B2TMC-2**. It should be noted that quantum computation indicates that the **BXTMC-2** chromophores will exhibit similar θ values in DCM and DMSO, and so we have successfully accessed intermediate θ in polar and nonpolar solution which are less than 80°, but still deviate significantly from planarity.

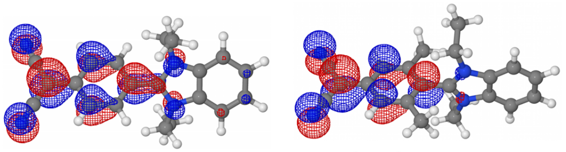

HOMO (θ = 40) HOMO (θ = 90)

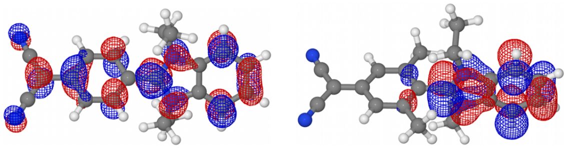

LUMO (θ = 40) LUMO (θ = 90)

Figure 1.12. HOMO and LUMO contours of **BXTMC-2** chromophores with 40° and 90° twist angles.

1.3.3 Comparison to TMC-2 and previous TICT chromophores. Comparison to other TICT chromophores sheds light on the impact of the benzimidazolium group as compared to other acceptors previously employed. The transition moments, even in **B2TMC-2** ($\varepsilon = 8156\ \text{M}^{-1}\text{cm}^{-1}$) are markedly greater than those reported for **TMC-2** ($\varepsilon = 1840\ \text{M}^{-1}\text{cm}^{-1}$) and **TMC-3** ($\varepsilon = 2090\ \text{M}^{-1}\text{cm}^{-1}$), likely reflecting the reduced torsional angles. The enhanced transition moment may also relate to the change in acceptor group, which dictates the attributes of the LUMO. Electronic structure calculations show that a large portion of the LUMO electron density is located on the bridging carbon, yielding a strong overlap with HOMO located on the donor fragment, particularly at intermediate torsional angles (Figure 1.12).

The **BXTMC-2** CT transition in the 407-434 nm range is at much higher energy than that of previous twisted chromophores (λ_{CT} = 569 nm for **TMC-2**), due to the ~0.5 eV increase of the LUMO level as compared to **TMC-2**. This constitutes a significant advantage; a device utilizing **BXTMC-2** chromophores could operate without linear loss in a far broader spectral window. In fact, the absorption edge in polar solvents is close to the visible region cutoff, making a high performance photonic device material with visible region transparency a distinct possibility.

Despite relatively large ground state dipole moments, the **BXTMC-2** chromophores are less sensitive to solvent environment than any previous second order NLO TICT chromophore. The maximum measured solvatochromic shift (measured from $CHCl_3$ to MeOH) of **B2TMC-2** is -57 nm, as compared to ~-180 nm for **TMC-2**, showing that replacement of the pyridinium fragment with benzimidazolium significantly reduces the dependence of the relative energy level spacing on the dielectric environment. Several factors may contribute to this observation: (1) the positioning of the bulky alkyl groups may reduce solvent interactions with the acceptor moiety; (2) the reduced CT distance versus **TMC-2** decreases the dipole moment and therefore the importance of solvent stabilization; (3) the benzimidazolium acceptor provides more effective stabilization of the ground state positive charge than previous acceptor groups.

1.3.4 Monomeric NLO response in DCM and DMF. The contribution of both CH_2/H and CH_2/CH_3 steric interactions to the bi-aryl torsion allows access to intermediate solution twist angles which were not available in previous studies. The present evidence suggests that twist angle is directly related to $\mu\beta_{vec}$, and that the highest nonlinear response is achieved above 70°. The justification for large NLO response of this nature is now well-known to arise from the ZA/NQ balance in the molecule.[29,35] Twisting, or otherwise disrupting conjugation, serves to simultaneously destabilize the ground state, stabilize the excited state, and create very large charge separation leading to giant dipole moments. The large NLO response is a consequence of these factors, as shown by extensive experimental and computational work. This concept has also been demonstrated by recent theoretical work showing enhanced β with disrupted conjugation, as provided by large torsional angles.[23,24]

In the past, TICT chromophores performed poorly in polar environments, despite marked decreases in aggregation.[30,36] For **TMC-2**, NLO response was shown both experimentally and computationally to peak in moderately polar solvents, then diminish with increasing polarity. This behavior was attributed to the stabilization of the zwitterionic ground state relative to the excited state manifold in highly polar environments.[29,83,84] In the case of **B2TMC-2**, the high NLO response observed in DMF is likely a result of reduced sensitivity to solvent polarity, as evidenced by relatively weak solvatochromic shifts (Δλ in Table 1.2). Of the TICT chromophores characterized to date, **B2TMC-2** shows the highest reported nonlinearity to date in DMF at 10^{-3} M (the highest measured concentration), highlighting the newfound ability to benefit from polar environments. It should be noted that according to the two-level model, changes in the linear absorption should lead to decreased NLO response in DMF versus DCM. However, it was previously noted that the two-level model does not always properly capture the impact of the dielectric medium.[60]

1.3.5 Concentration-dependence of NLO response. In DCM, the aggregation tendencies of **B2TMC-2** and **TMC-2** are similar; high responses observed at low concentrations quickly diminish in the range of 10^{-4} – 10^{-5} M. The observed aggregation tendencies are consistent with the tightly packed centrosymmetric unit cells in the crystal structures of **B1TMC-2** and **B2TMC-2**. The relatively short linear alkyl groups used here do not prevent interactions between the donor group and the face of the benzimidazolium fragment, as evidenced by the crystallographic packing. However, the design of **BXTMC-2** allows for facile modification of the sidechains; adding branched or dendritic groups has proven effective in the past, and may be used to prevent close access to the face of the acceptor moiety.[36,85] Aggregation of **B2TMC-2** is less favorable in DMF, as shown by a decrease in NLO response which occurs at higher concentrations, in the range of 10^{-3} – 10^{-4} M. Such improvements are encouraging, but clearly must be supplemented by the aforementioned chemical modification of the sidechains. Should this strategy prove effective in mitigating aggregation, it could be combined with the use of polar matrices, which had not been compatible with large NLO response in TICT chromophores until this point.

Table 1.4. Computed theoretical (β_{max}) and intrinsic (β_{int}), and EFISH (β_{EFISH}) hyperpolarizability in DCM at 1907 nm

	β (× 10^{-30} esu)		
	β_{EFISH}	β_{max}	β_{int}
B0TMC-2	-486	-3370	0.14
B1TMC-2	-499	-3070	0.16
B2TMC-2	-1056	-2870	0.37

1.3.6 Intrinsic NLO response. In order to compare systems of different size and properties, it is useful to examine the intrinsic hyperpolarizability defined by Kuzyk as β_{int} = (observed β)/(theoretical maximum, β_{max}), for a structure with a particular number of polarizable electrons and a characteristic low-lying optical transition.[12] **B2TMC-2** yields a remarkably high $\beta_{int} = 0.37$, which is one of the largest values ever reported in the open literature (Table 4). Even modestly twisted **B0TMC-2** exhibits a large $\beta_{int} = 0.14$, still remarkably higher than the vast majority of efforts which lie below $10^{-3/2}$. Thus, the **BXTMC-2** chromophore series has proven capable of large NLO response arising from the efficient application of a small number of electrons.

1.4 Conclusions. A new series of twisted π-system electro-optic chromophores was synthesized by expeditious new routes and shown to be qualitatively similar to previous TICT generations, with large ground state dipole moments, low-lying CT transitions, and primarily zwitterionic/aromatic character. The same theories which justified NLO response in the past also apply here, as evidenced by the dependence of $\mu\beta$ on twist angle. The introduction of steric hindrance using a benzimidazole moiety permits access to intermediate torsional angles and demonstrates the effect of experimentally twisting in this range for the first time.

The highlight of the present work is the strong NLO performance of chromophore **B2TMC-2** in DMF, which represents a 5× increase over archetypical chromophore **TMC-2**. We recognize that it is now possible to perform EFISH and E-O measurements in highly polar environment, opening new pathways to address detrimental aggregation. We are now pursuing promising directions involving modification of solvent polarity through addition of organic salts, means of artificially increasing polymer matrix polarity, and introduction of dendritic sidechains. The use of highly polar matrices may be a key factor in preventing aggregate formation and realizing the exciting full potential of TICT chromophores.

Chapter 2. Organic Salts Suppress Aggregation and Enhance Hyperpolarizability of a π-Twisted Chromophore

Lou, Alexander J.-T.; Righetto, Stefania; Cariati, Elena; Marks, Tobin J. *Manuscript in preparation*.

This work was performed in collaboration with the co-authors listed above.

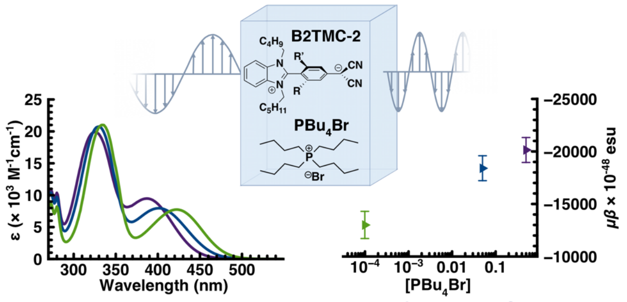

PBu$_4$Br addative increases $\mu\beta$ of B2TMC-2

Abstract. Twisted intramolecular charge transfer (TICT) chromophores exhibit extraordinary hyperpolarizability, β, and are therefore promising candidates for electro-optic devices. However, they are limited by aggregate formation which severely diminishes β in concentrated solutions or polymer matrices. Here we report the impact of organic salt additives on the linear and nonlinear optical response of a recently developed high-β TICT chromophore, **B2TMC-2**. Addition of $Bu_4P^+Br^-$ to **B2TMC-2** solutions in $CHCl_3$ causes halochromic blue-shifting of the charge transfer absorption maximum to < 400 nm, primarily resulting from strong interactions between $Bu_4P^+Br^-$ and the **B2TMC-2** cationic terminus. DC electric-field induced second harmonic generation (EFISH) measurements in $Bu_4P^+Br^-/CHCl_3$ reveal a large $\mu\beta = -22{,}160 \times 10^{-48}$ esu in dilute solution**,** which is unprecedented for any chromophore with such a broad optical transparency window. Moreover, $Bu_4P^+Br^-$ is shown here to mitigate **B2TMC-2** aggregate formation, preserving high $\mu\beta$ in concentrated solutions. Including $Bu_4P^+Br^-$ can beneficially modify the chromophore environment in solution and polymer films; we anticipate that given the diverse array of available organic salts, these interactions can be improved and extended to other chromophores.

2.1 Introduction. Electro-optic (E-O) materials are of interest for applications in telecommunications, image processing, and sensing.[11] The E-O response in organic materials depends, among other factors, on the hyperpolarizability (β) of the individual molecular constituents. Therefore, intense investigations have concentrated on designing suitable chromophores with high β values and low optical absorbance at telecommunication wavelengths.[52] Our efforts focus on twisted π-system intramolecular charge transfer (TICT) chromophores, composed of donor and acceptor moieties separated by a twisted bi-aryl fragment.[30] Their remarkable β values arise from a large ground state dipole moment (μ) and careful balancing of aromatic/zwitterionic and quinoidal/neutral electronic structure contributions, which are primarily dictated by the degree of bi-aryl torsion (Figure 2.1, *bottom*).[86] However, while TICT chromophores exhibit very large $\mu\beta$ values in dilute solution, translating this performance to device-ready materials has proven challenging; the large μ that is critical to high β also drives the formation of centrosymmetric aggregates for which $\mu\beta$ approaches zero. Thus, TICT chromophores do not realize their full potential in concentrated solutions or in host-guest polymer/chromophore films.[33] Previously, polar solvents such as DMF were shown to suppress aggregation, but also increased the HOMO/LUMO energy gap resulting in unacceptably reduced $\mu\beta$.[30] Only recently we reported a new chromophore **B2TMC-2** (Figure 2.1, *top*), which combines reduced aggregation and good performance ($\mu\beta \sim -20{,}730 \times 10^{-48}$ esu) in polar solvents such as DMF.[32] This development motivates the approach described here.

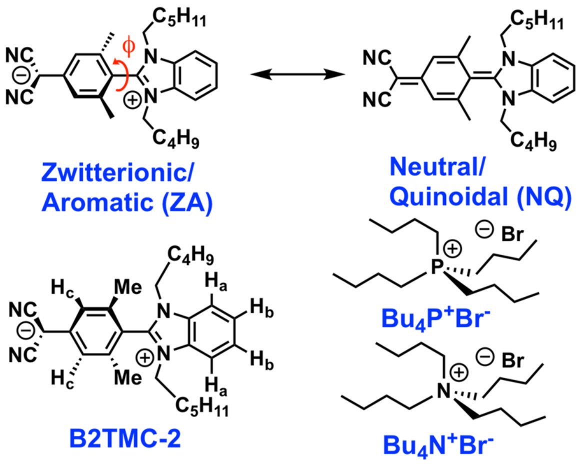

Figure 2.1. *Top*: TICT chromophore **B2TMC-2** (with labeled aromatic protons) and organic salts $Bu_4P^+Br^-$ and $Bu_4N^+Br^-$. *Bottom*: Aromatic and quinoidal resonance forms of **B2TMC-2**.

In this work, we seek to mitigate TICT aggregation with organic salt additives (Figure 2.1), which may modify the effective solvent polarity[87-89] and introduce new coulombic interactions that compete with electrostatic driven aggregation.[90,91] Tetrabutylphosphonium bromide ($Bu_4P^+Br^-$)

and tetrabutylammonium bromide ($Bu_4N^+Br^-$) are selected as model salts due to their excellent stability, compatibility with organic solvents and polymers, and lack of visible absorption.

2.2 Influence of $Bu_4P^+Br^-$ and $Bu_4N^+Br^-$ on linear absorption spectra, aromatic ^{1}H NMR chemical shifts, and solution vibrational frequencies. The linear absorbance spectrum of **B2TMC-2** (Figure 2.2A) is characterized by a charge transfer (CT) absorption (λ_{CT} = 425 nm in $CHCl_3$) and a strong sub-fragment transition at ~320-340 nm. In 1.0 M $Bu_4P^+Br^-/CHCl_3$, λ_{CT} blue-shifts to 391 nm, which is identical to an acetone solution. Based on the similar polarity of acetone ($E_T(30)$ = 42.2 kcal/mol) and $Bu_4P^+Br^-$ itself ($E_T(30)$ = 43.5 kcal/mol) as assessed by solvatochromic shift of Reichardt's Dye, we expect this is essentially the limiting value of λ_{CT}.[32,92] The analogous ammonium salt yielded similar results; in 1.0 M $Bu_4N^+Br^-/CHCl_3$, **B2TMC-2** exhibits λ_{CT} = 395 nm (see Appendix). Note that changes in λ_{CT} are purely a result of salt-induced effects rather than aggregation, as confirmed by the absence of spectral changes upon dilution from 10^{-4} to 10^{-6} M **B2TMC-2** in pure $CHCl_3$.

To confirm that this behavior persists in a glassy polymer matrix, host/guest films were fabricated from poly(methylmethacrylate) host polymer (PMMA, $\varepsilon = 3.2 – 3.5$), with ~15% (w/w) **B2TMC-2** and $Bu_4P^+Br^-$ ranging from ~2 - 30 % (w/w). The hypsochromic shift from the pure PMMA/**B2TMC-2** film (λ_{CT} = 398 nm) to a film with 30 % $Bu_4P^+Br^-$ (λ_{CT} = 385 nm) is smaller than in solution, but clearly indicates persistent $Bu_4P^+Br^-$/**B2TMC-2** interactions in the film. This demonstrates one of the main advantages of these additives; unlike a volatile organic solvent, $Bu_4P^+Br^-$ (a solid) can be used to tune the properties of a host polymer matrix.

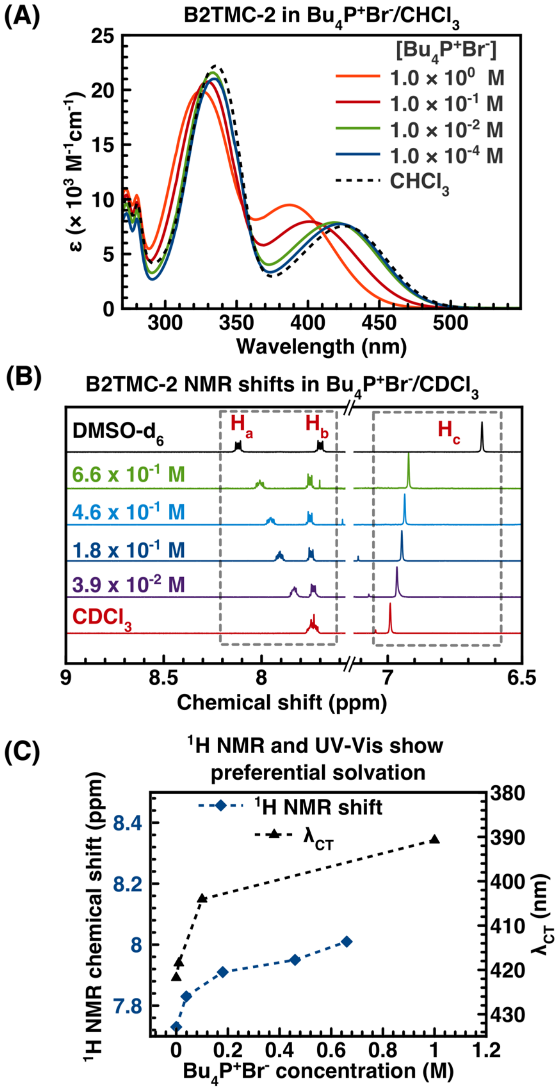

Figure 2.2. (A) Linear optical absorbance spectra of a 1.0 × 10^{-4} M $CHCl_3$ solution of **B2TMC-2** with varied $Bu_4P^+Br^-$ concentrations; (B) Aromatic region ^{1}H-NMR chemical shifts of **B2TMC-2** in $CDCl_3$ solutions as a function of the indicated $Bu_4P^+Br^-$ concentrations (labelling according to Figure 2.1) with the chemical shifts in DMSO shown for reference; (C) Acceptor group ^{1}H-NMR chemical shifts and λ_{CT} as a function of $Bu_4P^+Br^-$ mol %. Concentrations refer to the amount of $Bu_4P^+Br^-$ in solution.

The twisted bridge in **B2TMC-2** serves to decouple the respective fragments, so that changes in the donor fragment ^{1}H NMR chemical shifts (δ_{Hc}) do not strongly impact the acceptor resonances (δ_{Ha} and δ_{Hb}), and *vice versa*. This segmentation allows for individual assessment of salt/donor and salt/acceptor effects. A solution with ~0.7 M $Bu_4P^+Br^-$ exhibits a ~0.07 ppm up-field shift of δ_{Hc}

relative to pure $CHCl_3$ solution, indicating increased electron density on the donor fragment (Figure 2.2B). Meanwhile, the acceptor peak H_a shifts 0.26 ppm down-field in the same solution, corresponding to increased electron deficiency of the acceptor fragment (Figure 2.2B). A parallel experiment using $Bu_4N^+Br^-$ reveals essentially identical trends (see Appendix). In both cases, the absence of multiple sets of signals rules out the formation of covalent salt/chromophore bonds.

FT-IR vibrational spectroscopy was performed on solutions of **B2TMC-2** in pure $CHCl_3$, and with 0.05, 0.1, and 0.5 M $Bu_4P^+Br^-$. There is a noticeable decrease in the energy of the cyano group stretching, $\nu(C{\equiv}N)$, from 2175 cm^{-1} in pure $CHCl_3$ to 2172 cm^{-1} in 0.5 M $Bu_4P^+Br^-$ corresponding to slightly increased electron density on the carbanion.

2.3 Anion-driven halochromism and preferential solvation. Halochromism is defined by Reichardt et al. as the change in λ_{CT} resulting from *specific*, *coulombic* interactions between a salt and a chromophore (loose ion-pair formation), in the absence of covalent bond formation.[93] In **B2TMC-2**, such interactions would raise the ionization potential of the donor group or lower the electron affinity of the acceptor group, accounting for the observed negative shift in λ_{CT}.[93] The large magnitude of the aforementioned salt-induced changes in δ_{Ha} relative to δ_{Hc} is indicative of a dominant *specific* coulombic interaction between the **B2TMC-2** cationic acceptor group and Br^-. This is likely a result of the bulky Bu_4P^+ *n*-butyl groups, which limit its electrostatic interactions with both the Br^- anion and the anionic **B2TMC-2** donor group, consistent with the small observed shifts in $\nu(C{\equiv}N)$ noted above.[93,94] The weak ion-pairing between Bu_4P^+ and Br^- increases the availability of the Br^- anion to interact with the acceptor group resulting in a large change in δ_{Ha} and λ_{CT}. Thus, the spectroscopic evidence supports that the $Bu_4P^+Br^-$ and $Bu_4N^+Br^-$ /**B2TMC-2** systems exhibits *genuine negative halochromism*, and that the shift in λ_{CT} primarily results from the decreased electron affinity of the benzimidazolium fragment. The relative strength of the acceptor/Br^- interaction is supported by the comparison of the reported crystallographic distances between the charged atoms of representative ion pairs (see Figure S2.6); Bu_4N^+/dicyanomethanide (~4.7-5.6 Å)[95,96] > benzimidazolium/dicyanomethanide of neighboring **B2TMC-2** molecules (~4.5 Å)[32] > Bu_4P^+/Br^- (~4.1-4.4 Å)[97] > benzimidazolium/Br^- (~3.8-4.1 Å).[98,99] The shorter ion pair distance generally reflects a stronger coulombic interaction.

Halochromism is often accompanied by preferential solvation, meaning that the solvation shell of **B2TMC-2** has a disproportionally high amount of $Bu_4P^+Br^-$ compared to the bulk solution composition.[100,101] This manifests as large spectroscopic changes at low concentration, which begin to approach a limiting value at < 20 mol % $Bu_4P^+Br^-$ (Figure 2.2C), presumably as the salt saturates the **B2TMC-2** solvent shell. As such, further addition of $Bu_4P^+Br^-$ is unlikely to result in significant spectroscopic changes.

2.4 EFISH measurements of solution NLO response. Measurements of $\mu\beta_{vec}$, the product of the μ and the vector part of the molecular first-order hyperpolarizability β_{vec} tensor along the μ direction, were performed by the solution-phase DC electric field induced second harmonic generation (EFISH) method, which provides direct information on the intrinsic molecular nonlinear optical (NLO) response via eq 2.1. Here, $\mu\beta/5kT$ is the dipolar orientational

$$\gamma_{EFISH} = (\mu\beta/5kT) + \gamma(-2\omega;\ \omega,\ \omega,\ 0) \qquad (2.1)$$

contribution, and $\gamma(-2\omega;\omega,\omega,0)$, the third-order term at frequency ω of the incident light, is the electronic contribution to γ_{EFISH}, which should be negligible for the type of molecules investigated here.[81] To isolate the monomeric **B2TMC-2** response in various environments and the impact of $Bu_4P^+Br^-$ on aggregation, EFISH measurements were performed on **B2TMC-2** in five $CHCl_3$

solutions having varied concentrations of $Bu_4P^+Br^-$: **A** (10^{-4} M, ~0.04 mg/mL $Bu_4P^+Br^-$**)**, **B** (0.05 M, ~20 mg/mL), **C** (0.1 M, ~40 mg/mL), **D** (0.5 M, ~200 mg/mL), and pure $CHCl_3$ (Figure 2.3). All measurements were performed in anhydrous solvent to ensure that the ion pairs remain intact, and control experiments indicated that salt itself has a negligible contribution to the measured $\mu\beta_{vec}$.

It is well established that the inverse relationship between concentration and $\mu\beta$ in TICT chromophores is a result of chromophore aggregation, so the most dilute measurements are taken to be representative of monomeric β_{vec}.[30] Solution **B** (5.0×10^{-5} M) exhibits $\beta_{vec} = -923 \times 10^{-30}$ esu, indicating that **B2TMC-2** maintains high monomeric β_{vec} in the presence of $Bu_4P^+Br^-$ as compared to pure DMF(-828×10^{-30} esu) or DCM (-1056×10^{-30} esu).

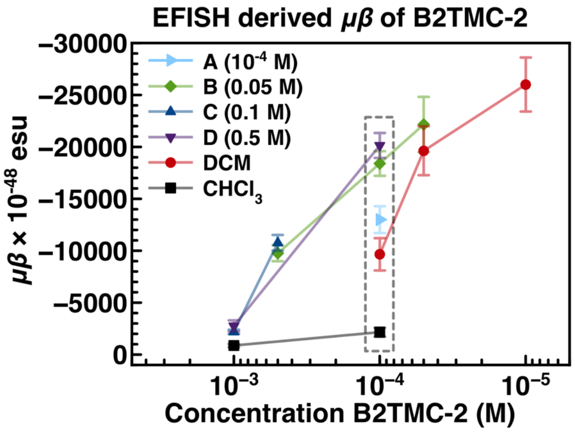

Figure 2.3. EFISH derived $\mu\beta_{vec}$ as a function of **B2TMC-2** concentration, at the indicated $Bu_4P^+Br^-$ concentrations in $CHCl_3$ and in DCM: **A** (10^{-4} M), **B** (0.05 M); **C** (0.1 M); **D** (0.5 M). Lines are drawn to guide the eye.

The effects of aggregation are qualitatively evidenced by the decrease in $\mu\beta_{vec}$ with increasing **B2TMC-2** concentration (Figure 2.3). In solutions **B-D**, this characteristic diminution is shifted to higher concentrations of **B2TMC-2**, thereby extending the threshold for high $\mu\beta_{vec}$ by at least 5× relative to $CHCl_3$ solutions. The 10^{-4} M **B2TMC-2** solutions offer a striking comparison; $\mu\beta_{vec}$ of solutions **B** and **D** (~ -20,000 × 10^{-48} esu) far exceeds that of heavily aggregated $CHCl_3$ (-2,160 × 10^{-48} esu) and DCM (-9,660 × 10^{-48} esu) solutions. Even solution **A** (-13,000× 10^{-48} esu) exhibits major enhancement, despite the low concentration of $Bu_4P^+Br^-$ (10^{-4} M).

2.5 Role of $Bu_4P^+Br^-$ in improved NLO response. It is well known that $\mu\beta_{vec}$ is related to CT energy, transition strength and change in state dipole moment, all of which are reflected by linear absorbance.[11] However, while salt-induced changes in these parameters certainly influence $\mu\beta_{vec}$, they cannot reasonably account for the observed drastic improvements. Therefore, the increased response in solutions **A-D** must arise predominantly from the influence of $Bu_4P^+Br^-$ on aggregation tendencies of **B2TMC-2**.

The proposed mechanism of disaggregation relates to the competition of dipolar and coulombic chromophore/chromophore interactions with coulombic salt/chromophore interactions. In salt-free, moderately polar solvents, the dominant stabilizing interaction of TICT chromophores is the formation of centrosymmetric dimers, as supported by spectroscopic and crystallographic data.[30,32] The addition of $Bu_4P^+Br^-$ introduces a new set of stabilizing interactions, evidenced by strong halochromic shifts, which are in direct competition with the columbic donor/acceptor attraction. In similar to polyzwitterion/salt systems, this type of coulombic interaction also screens the dipole-dipole attractions that contribute to aggregation.[102,103] This suppression of aggregate forming chromophore/chromophore interactions prevents the presence of centrosymmetric structures, leading to enhanced $\mu\beta_{vec}$. Furthermore, preferential solvation causes disaggregating effects to manifest at very low concentration, as seen in solution **A**. The addition of more $Bu_4P^+Br^-$ improves $\mu\beta_{vec}$, although the similarity of solutions **B-D** reflects the saturation of $Bu_4P^+Br^-$ in the solvation shell or the limit on interaction strength of this particular salt/chromophore pairing.

2.6 Conclusions. We have shown that $Bu_4P^+Br^-$ can significantly increase the solution phase $\mu\beta_{vec}$ of **B2TMC-2** by introducing coulombic interactions which compete with **B2TMC-2** aggregation. $Bu_4P^+Br^-$ appears to function similarly in host/guest polymer films and can therefore be applied to E-O devices. Reducing the steric bulk of the cation, using an alkali or alkaline earth metal cation and organic anion, or employing multiply charged ions may improve the strength of the coulombic interactions, perhaps leading to further improvements. In addition to suppressing aggregation, salt additives provide an opportunity to blue-shift λ_{CT}, which could lead to organic E-O modulators with very wide operating windows and reduced likelihood of photochemical damage.[54] Our exploration of salt modifiers to polymer and solvent environment serves as a proof of concept which may doubtless be expanded to a greater variety of salts and chromophores to draw more general conclusions.

Chapter 3. Two-Photon Induced Excited State Refraction in a TICT/Stilbene Hybrid Chromophore

Lou, Alexander J.-T.; Benis, Sepehr; Gao, Munan; Baev, Alexander; Kim, David; Van Stryland, Eric; Hagan, David; Marks, Tobin J. *Manuscript in preparation.*

This work was performed in collaboration with the co-authors listed above.

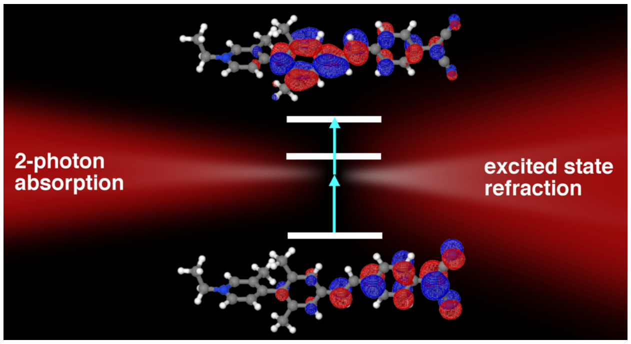

Abstract. Twisted intramolecular charge transfer (TICT) chromophores have exhibited promising 3rd order nonlinear optical (NLO) response, which is potentially useful for all-optical switching. It is therefore valuable to study the impact of structural modifications on NLO response and expand the diversity of known TICT structures. Here we have synthesized a hybrid molecule that incorporates a stilbene and TICT motif and explored its 3rd and 5th order NLO responses. Solution Z-scan measurements in CH_2Cl_2 reveal modest two-photon absorption at 1100 and 800 nm ($\sigma_{2PA} > 90$ GM), which is several times larger than any pure TICT chromophore measured to date, and is attributed to states residing on the stilbene fragment. The nonlinear refractive index increases with light intensity, revealing that the mechanism is a 5th order process involving two-photon induced excited state refraction (2PA-ESR). The ESR cross section ($\sigma_{ESR} \sim 10^{-16}$ cm^2) accounts for almost all of the contribution to nonlinear refraction and indicates an excess polarizablity of the 2-photon excited state, which is a direct result of the unique hybrid TICT/stilbene character. This work yields further insight into the 3rd order NLO response of TICT chromophores and demonstrates that subtle structural modifications can have a significant impact on their functionality.

3.1 Introduction. Over the past few decades there have been several reports of high-order nonlinear optical (NLO) responses in semiconductors and organic chromophores, which involve excited-state nonlinearities induced by two-photon absorption (2PA).[104-107] Such materials are of interest, as they exhibit intensity-dependent nonlinear refraction (NLR) and nonlinear absorption (NLA) which is potentially useful for all-optical signal processing and optical power limiting respsectivly.[7,13,108-110] The high-order contribution to NLR arises via a sequential, 5th order process, in which 2PA is followed by excited-state refraction (ESR).[105,111] This effect (sometimes denoted $\chi^{(3)}:\chi^{(1)}$) is quantified on the molecular scale by an ESR cross-section (σ_{ESR}) and 2PA cross-section

σ_{2PA}. The initial 2PA process is a relatively common phenomenon in organic chromophores and the design principles are now well understood for several structure types.[112] σ_{ESR} can theoretically be observed in any molecule for which the ground and excited state polarizablity differs, although literature reports of σ_{ESR} and its contribution to NLR are somewhat scarce.[104-107,113]

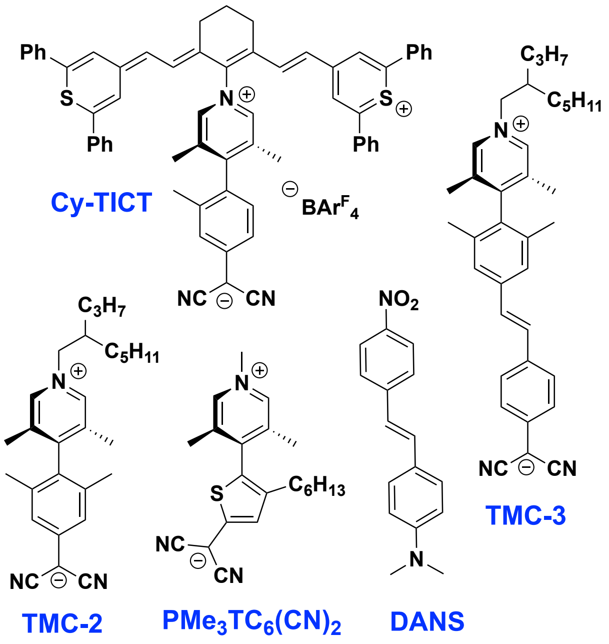

Figure 3.1. Archetypal TICT chromophore **TMC-2**, thiophene derivative **$PMe_3TC_6(CN)_2$**, TICT/stilbene chromophore **TMC-3'**, cyanine/TICT hybrid **Cy-TICT**, and donor/acceptor stilbene **DANS**.

The more commonly reported mechanism of NLR comes from the direct 3rd order nonlinearity, which occurs on a very short timescale,[41] and manifests in bulk materials as the bound-electronic nonlinear refractive index n_2. In molecular materials this property is related to the second hyperpolarizability, γ, of the constituent chromophores. Strategies to enhance γ include bond length alternation (BLA), which involves balancing neutral and charged contributions to the ground state, creation of 2-D chromophores,[114,115] inclusion of auxiliary heterocyclic donor moieties, and optimization of the chromophore environment.[12,15,21,35,90,116-119] Our previous work has focused on the design of twisted intramolecular charge transfer (TICT) chromophores which feature a donor and acceptor fragment connected by a twisted bi-aryl bridge. The degree of bi-aryl torsion leads to localization of the HOMO and LUMO on the donor and acceptor fragment respectively, which results in a very large ground state dipole moment (α_g), low charge transfer energy (E_{ge}) and generally low CT transition dipole moment (μ_{ge}).[28,36,40] Several modifications of the archetypal chromophore **TMC-2** (Figure 3.1), such as donor and acceptor group substitution (**$PMe_3TC_6(CN)_2$**) and coupling to a cyanine dye (**Cy-TICT**), lead to improvement γ. [34,35,40]

In this work, we investigate the impact of adding a stilbene fragment to archetypal chromophore **TMC-2,** to form **TMC-3'**. In the past, this modification greatly enhanced 2nd order NLO response in **TMC-3,** primarily due to the increase ground state dipole moment.[30,31] Here, the added stilbene fragment serves to introduce significant 2PA to the TICT system and activates 5th order nonlinearities. We have performed Z-scan measurements on **TMC-3'** at multiple intensities and wavelengths in order to ascertain (1) the 2PA cross-section (σ_{2PA}) and (2) the presence and dispersion of σ_{ESR} induced by 2PA. In order to understand the trend and magnitude of σ_{ESR} we have pursued electronic structure calculations which show that the hybrid nature of the molecule is accountable the differences between **TMC-3'** previous TICT systems.

3.2 Experimental methods.

3.2.1 Nonlinear optical characterization by Z-scan. The 3rd and 5th nonlinear optical response of **TMC-3'** was measured by the Z-scan method, which probes the change in absorption and refraction of a sample as a function of local light intensity.[120] This experiment operates in two modes referred to as open aperture (OA), which reveals the nonlinear absorption cross section (δ_{NLA}), and closed aperture (CA) used to determine nonlinear refraction (δ_{NLR}). In this work, we have used a dual arm Z-scan (DA Z-scan) setup, which allows for the simultaneous measurement of solvent and solution, making it possible to subtract the solvent signal while directly accounting for beam fluctuations.[121] DA Z-scan can improve the signal-to-noise ratio (SNR) by an order of magnitude compared to single arm Z-scan.[121] In order to determine both the dispersion and origin of NLA and NLR, measurements were performed using several intensities at 800, 1100, and 1300 nm. **TMC-3'** solutions were prepared in dry CH_2Cl_2 at ~1 mM concentration. Further details of nonlinear optical measurements are presented in Appendix section S3.2.

3.2.2 Computational methods and polarizability calculations. Model **TMC-3'** analogues were optimized in the gas phase and with PCM (CH_2Cl_2) at the B3LYP/6-31G** level. Optimized torsional angles of ~90° in CH_2Cl_2 are in good agreement with previous work and crystallographic data.[30,33,40] Molecular second hyperpolarizability, γ, was calculated in the Amsterdam Density Functional package using CAM-B3LYP/6-31+G*.[122] TDDFT was performed in Q-Chem using CAM-B3LYP/6-31+G** on **TMC-3'** structures with constrained bi-aryl dihedral angles of 65°, 70°, 75°, 80°, 85°, 89°.[123]

Calculation of polarizabilities (α) can be performed using expressions obtained from perturbation of a molecular dipole moment (μ) with an electric field (F) (eq. 3.1). The finite field

$$\mu(F) = \mu_0 + \alpha F + \frac{1}{2}\beta F^2 + \cdots \tag{3.1}$$

(FF) method involves the calculation of state dipole moments at applied static fields, fitting the results with eq 1. This method is advantageous for determining excited-state polarizabilities because it does not depend on higher excited-state characteristics, which are often unreliable.[124-127] However, it does not provide specific information about the relative contribution of specific states, nor does it account for frequency dependence of polarizablity. A complementary approach is the sum-over-states (SOS) method (eq. 3.2), which directly correlates the property of interest to characteristics of specific states; the full expression for α of state *n* is given by eq. 3.2. Here *n* and *m* represent different electronic states, μ is the transition moment between states, and E_{nm} is the difference in energy.

$$\alpha_n(\omega) = \sum_{n \neq m} \left[\frac{\langle \psi_m | \hat{\mu} | \psi_n \rangle^2}{E_{nm} - \hbar\omega} \right] \tag{3.2}$$

In this work, we employ the SOS approach to calculate polarizabilities from experimental data, and the FF method to calculate the change in static polarizability by computing ground and excited-state dipole moments in the presence of static fields ranging from -0.001 to 0.001 au in 0.0001 au increments. Small fields were used both to limit the contribution of higher-order terms, and to prevent reordering of the relevant states, which are somewhat closely spaced. Even so, careful interpretation of the state dipoles was required to obtain accurate results. The results were fit with the Taylor (or polynomial) method, including the hyperpolarizability (β) term.

3.3 Results and discussion.

3.3.1 Chromophore design and synthesis. The synthetic pathway (Scheme 3.1) developed here focuses on high yields and synthetic flexibility, allowing for better synthetic route towards **TMC-2** and **TMC-3** derivatives. Based on crystallographic and computational evidence, we have pursued a key tri-*ortho*-methyl biaryl fragment, which provides a comparable steric effect to the more synthetically challenging tetra-*ortho*-methyl moiety.[33] The synthesis begins with conversion of 2,5-dibromo-1,3-dimethylbenzene to **1** via regio-selective lithiation followed by treatment with dimethylformamide. The aryl bromide in **1** is then catalytically converted to BPin using $PdCl_2(PPh_3)_4$. Suzuki coupling of sterically hindered substrates **2** and 4-chloro-3-methylpyridine HCl is achieved using Buchwald's Sphos ligand to yield the key intermediate **3**. We elected to use a robust and *E*-selective Horner-Wadsworth-Emmons reaction with diethyl-4-bromobenzylphosphonate to form structure **4**. Catalytic coupling of **4** to malononitrile in the presence of $Pd(PPh_3)_4$ and NaH, subsequent alkylation with 2-octyldecyl triflate, and basification affords **TMC-3'** in an overall yield of 32% over six steps. The product and key intermediates were characterized by ^{1}H NMR, ^{13}C NMR, elemental analysis, and mass spectrometry. This synthetic pathway represents a significant improvement on previous efforts, with a reduction of total steps from 13 to 6, and produces a molecule which is sufficiently soluble to make highly concentrated solutions needed for NLO characterization.

Scheme 3.1. Synthesis of **TMC-3'**

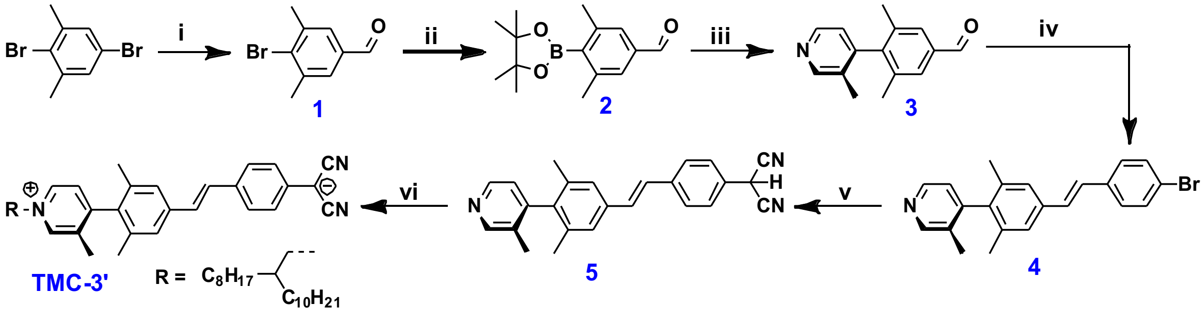

Conditions: (i) (a) n-BuLi, -78 °C, THF (b) DMF; (ii) $Pd(PPh_3)_2Cl_2$, B_2pin_2, KOAc, 1,4-dioxane; (iii) 4-bromopyridine*HCl, $Pd_2(dba)_3$/SPhos, K_3PO_4, toluene/water; (iv) diethylbromobenzylphosphonate, KOtBu, THF; (v) $NaCH(CN)_2$, $Pd(PPh_3)_4$, NaH, DME; (vi) ROTf in CH_2Cl_2 then NaOMe in MeOH.

3.3.2 Vibrational spectroscopy. The strength and frequency of CN stretching modes, *v*(CN), are diagnostic of electron density located on the dicyano methanide group. Here we observe *v*(CN) = 2162 cm^{-1} and a low energy side component at 2112 cm^{-1} in the solid state (Figure S3.1). Similar bands of 2164 and 2118 cm^{-1} were found in **TMC-3**, and the quantitative agreement of *v*(CN) to that of a phenylmalononitrile carbanion (*v*(CN) = 2163, 2117 cm -1) suggests that the dicyanomethanide fragment in **TMC-3'** supports nearly a full negative charge, consistent with a zwitterionic ground state.[30,128]

3.3.3 Linear optical absorbance of TMC-3'. The linear optical absorption of **TMC-3'** in CH_2Cl_2 (Figure 3.2A) is characterized by an intense sub-fragment charge transfer (SFCT) at 425 nm (ε = 32,000 M^{-1} cm^{-1}) and a weaker inter-fragment charge transfer (ICT) band at 542 nm (ε = 2130 M^{-1} cm^{-1}). The two low-energy excitations highlight the hybrid nature of **TMC-3'**; the ICT excitation is similar in energy and strength (μ_{01} = 2.3 D) to that of **TMC-2** (560 nm in CH_2Cl_2), while the SFCT excitation has a large transition moment (μ_{02} = 8.3 D) typical of a donor/acceptor stilbene.[112,129] Comparison of the change in ICT ($\Delta\lambda \sim -77$ nm) and SFCT ($\Delta\lambda = -32$ nm) peak maxima in CH_2Cl_2 and MeOH solutions suggest that the magnitude of the state dipole moments increase in the order of $\mu_{ICT} < \mu_{SFCT} < \mu_g$. The linear absorbance characteristics of **TMC-3'** are nearly identical to previously reported **TMC-3**, which exhibits ICT and SFCT strengths of 2040 and 38,400 M^{-1} cm^{-1} respectively, and an equivalent solvatochromic shift of the SFCT peak (Figure 3.2B).[33]

As was previously identified by PGSE NMR experiments on **TMC-3**, the large μ_g of these chromophores causes a tendency towards aggregate formation, even in relatively dilute solutions.[30,33] Here, this is evidenced by the hyspochromic shift of the ICT band upon concentration from 10^{-6} to 10^{-4} M in CH_2Cl_2 (Figure 3.2C). Although it is difficult to de-convolute the weak ICT peak from the much stronger SFCT peak, we can estimate that the hypsochromic shift of the ICT peak between dilute solutions (~10^{-6} M) and concentrated Z-scan solutions (>10^{-3} M) is in excess of 0.2 eV.

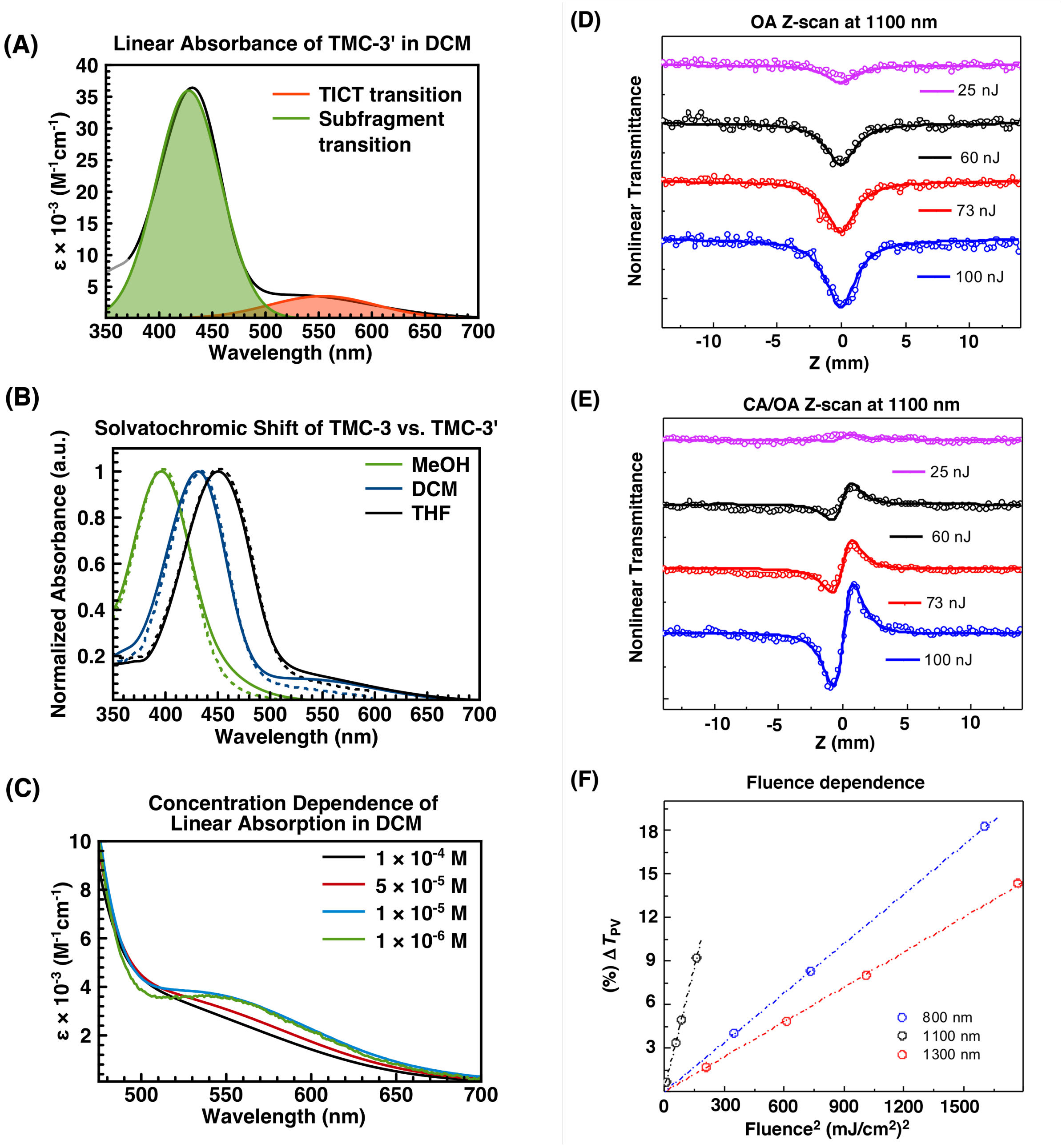

Figure 3.2. (A) Fitting of ICT and SFCT peaks of **TMC-3'** ($\sim 10^{-5}$ M) in CH_2Cl_2 (B) Comparison of solvatochromic shift of **TMC-3’** (solid lines) and **TMC-3** (dotted lines). (C) Concentration dependent absorption of **TMC-3’** in CH_2Cl_2, focused on the ICT peak. (D) OA Z-Scan results of **TMC-3’** in CH_2Cl_2 at 1100 nm with 2PA fitting (E) Closed aperture results at 1100 nm fit for 2PA-ESR (F) Normalized transmission of CA versus square of the fluence for three different wavelengths, indicating quadratic dependence of the NLR on the fluence. (Z-scan results for 800 nm and 1300 nm are reported in S3.2).

3.3.4 NLO characterization by Z-Scan measurements. OA measurements were performed at different pulse fluences and frequencies. The linear scaling of the signal versus pulse fluence indicates two-photon absorption (2PA) is the dominant mechanism in NLA, as evidenced by good fitting of experimental data with a 2PA model. This is also consistent with significant σ_{2PA} found by quantum computation (*vida infra*). OA measurements (Figure S3.2) revealed a small 2PA cross section of σ_{2PA}~5 GM at 1300 nm, and higher values of ~100 GM at 1100 and 800 nm (Table 3.1, Figure 3.2D). These values of σ_{2PA} exceed those of TICT chromophores **TMC-2** (8.9 GM at 775 nm) and **$PMe_3TC_6(CN)_2$**.[35,40] They are similar to σ_{2PA} of donor/acceptor stilbene molecules, such as DANS (~200 GM maximum in CH_2Cl_2), and significantly smaller the best known 2P absorbers (> 1000 GM).[112,129,130]

Table 3.1. Comparison of **TMC-3'** and **TMC-2** Z-scan results in CH_2Cl_2

	TMC-3'			**TMC-2**	
Wavelength (nm)	800	1100	1300	~775	~1170
σ_{ESR} (x 10^{-16} cm^2)	2.2	4.8	7.2	----	----
σ_{NLA} (GM)	102	92	< 7.0	8.9	< 1.5
Linear transmittance	~0.99	~0.99	~0.99	~0.98	~0.99

CA measurements (Figure 3.2E and S3.2) reveal NLR at all measured wavelengths. The magnitude of the response was determined to depend quadratically on the fluence of the input beam, indicating the presence of a higher-order nonlinearity (Figure 3.2F). Measurements were performed to obtain CA/OA signals as small as %5 to avoid higher order nonlinearities. Based on the significant observed 2PA we hypothesize that the underlying mechanism for NLR is a sequential 5th order process involving 2PA followed by ESR. This model (discussed in Appendix section S3.2) leads to much better fitting than a pure 3rd order model, and because the intercept in

Figure 3A is effectively zero, the contribution of 3rd order nonlinear refraction due to the bound electrons (and therefore γ) is very small. Fitting of the CA/OA Z-scan results with a $\chi^{(3)}$: $\chi^{(1)}$ model, reveals $\sigma_{ESR} = 2.2 \times 10^{-16}$, $4.8\ 10^{-16}$, 7.2×10^{-16} cm^2 at 800, 1100, 1300 nm respectively.

3.3.5 Computed two-photon absorption cross section and excited state character. Quantum computation reveals that $\sigma_{2PA} = 841$ GM at ~1000 nm and that the 2P excited state corresponds to the LUMO+3 orbital (Figure 3.4), which resides on the central and donor ring. The transition from HOMO to LUMO+3 is similar to the CT which occurs in DANS, meaning that the central ring in **TMC-3'** functions similarly to the terminal acceptor moiety of simple donor/acceptor stilbenes. Thus, it is unsurprising that the magnitude and position of this transition is comparable to simple stilbenes of this type.[129-131]

3.3.6 Origins of excited state refraction in ground and excited state polarizability. The change in refractive index given by σ_{ESR} is related to the difference in ground (α_g) and excited state (α_e) polarizability via eq. 3.3, where λ is the wavelength in cm, and *n* is the refractive index of the solvent.[132]

$$\sigma_{ESR} = \frac{4\pi^2}{\lambda}\frac{(n^2+2)^2}{9n}\left(\alpha_e - \alpha_g\right) \tag{3.3}$$

$$\alpha_g(\omega) \approx \mu_{01}^2\left[\frac{1}{E_{01}-\hbar\omega} + \frac{1}{E_{01}+\hbar\omega}\right] + \mu_{02}^2\left[\frac{1}{E_{02}-\hbar\omega} + \frac{1}{E_{02}+\hbar\omega}\right] \tag{3.4}$$

The full sum-over-states expression for α (eq. 3.2) can be truncated to a three-state model (eq. 3.4) and used to derive α_g from the lowest two excited states of **TMC-3'**, which can be unambiguously obtained from linear absorbance spectra in CH_2Cl_2 (Figure 3.2A). Here, E_{0m} and μ_{0m} are the energy and transition strength respectively, and ω is the frequency. Substitution into eq. 3.4 reveals α_g(800 nm)= 2.99×10^{-22}, α_g(1100 nm) = 2.47×10^{-22}, α_g(1300 nm) = 2.35×10^{-22} cm^3, and that the majority of the polarizability comes from the SFCT, which is a relatively intense transition.

Table 3.2. Calculated polarizability, dipole moment, and hyperpolarizability of **TMC-3'** at 85°

State	μ (D)	α (10^{-22} esu)	β (10^{-33} esu)	σ_{ESR} 10^{-17} cm^2
Ground	53.5	2.97	-7520	---
ICT	3.8	0.83	4620	-8.96
SFCT	34.0	3.48	-9540	2.13

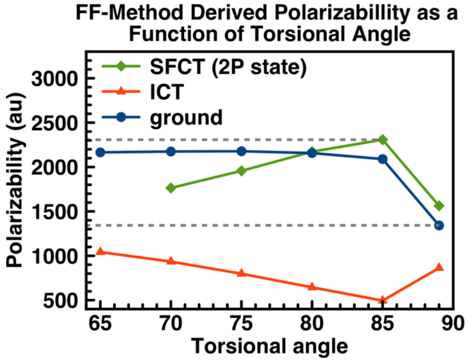

Figure 3.3. Computed static α of the ground, SFCT, and ICT states via the FF method, as a function of torsional angle (θ).

The finite field (FF) method, described in the Experimental Section, relies only on the computed energy or dipole moment of the excited state, and is therefore insensitive to the potentially erratic computed properties of the higher states. Fitting of the field-dependent dipole moments (Figures SX) reveals that the polarizability of the ground and SFCT state (α_{sfct}) are similar at the static limit, and that both exceed the ICT state polarizability (Table S3.1). Furthermore, these calculations reveal that α_g and α_{sfct} are highly sensitive to torsional angle (θ) of the bi-aryl fragment (Figure 3.3). There is a sharp increase in polarizability upon relaxation from 89° to 85°, concurrent with greater delocalization of the relevant orbitals (Figure 5, LUMO+3). Assuming a ground state θ = 89°, and an excited state θ = 85°, σ_{ESR} based on static α_g and α_{sfct} could exceed 9.73×10^{-17} cm^2.

The FF computed α_g at $\theta = 89°$ is close to the SOS value calculated from experimental spectra (Table S3.2), supporting that the ground state is highly twisted. This is in agreement with previous experimental evidence showing that the tri-*ortho*-methyl fragment leads to very large twist angles near 90°.[33] Thus, even the slightest relaxation of θ upon excitation would result in a significant increase in α_{sfct} and σ_{ESR}. Such relaxation is well established in the context of TICT chromophores and is therefore a distinct possibility, particularly as the LUMO+3 orbital exhibits some quinoidal character (Figure 3.4).[133,134] Unfortunately, the FF method is unable to account for the effects of resonant enhancement. As the 2-photon excited state is expected to be close in energy to the higher excited states, it is likely that the α_{sfct} is resonantly enhanced in the relevant spectral region, thereby also increasing σ_{ESR}.

3.3.7 TICT/Stilbene hybrid molecular orbitals. Molecular orbital pictures (Figure 3.4) provide a useful qualitative view of the three relevant orbitals: (1) The HOMO, which is mainly localized on the donor fragment, and has little to no electron density on the acceptor side of the twisted bridge; (2) The LUMO mainly resides on the pyridinium ring with a small amount of electronic density on the twisted bridge; (3) The LUMO+3 orbital, which resides in the center of the molecule, and is relatively delocalized compared to the HOMO and LUMO. The relaxation of the bi-aryl twist angle leads to even greater delocalization of LUMO+3 onto the acceptor fragment (Figure 3.4). This qualitative picture highlights the unique character of the **TMC-3'** chromophore. Planar stilbenes are typically smoothly conjugated such that the HOMO and LUMO are both relatively delocalized over large portions of the π-system.[130] **TMC-3'**, has a segmented electronic structure as a result of the twisted bi-aryl fragment, which localizes HOMO and LUMO, thereby limiting their polarizability. Excitation to the stilbene excited state accesses the more delocalized LUMO+3 orbital, which overlaps both acceptor and donor based higher excited states, leading to increased polarizability. We note that the characteristics of the LUMO+3 orbital are likely sensitive to the electron accepting or donating character of the central ring.

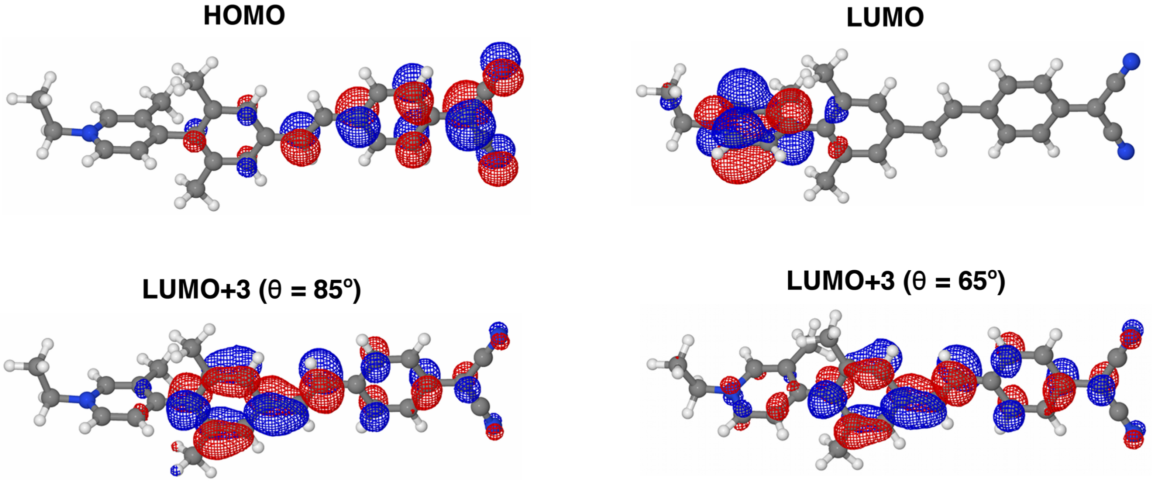

Figure 3.4. MO pictures of **TMC-3’** (85°) calculated at the CAM-B3LYP/6-31+G** level, cutoff set to 0.03.

3.3.8 Computation of 3rd order nonlinear optical response. Quantum computation allows us to assess the 3rd order response in the absence of confounding factors, namely aggregation, which complicate the analysis of structure-property relationships as discussed below. Calculations of Re(γ) were performed at wavelengths ranging from 775 to 1500 nm in order to encompass the technologically relevant window and to include regions of one- and two-photon enhancement (Table 3.3). Model compound **TMC-3’-EH** shows enhanced Re(γ) and a change in sign around 1000 nm, which coincides with the two-photon resonance of the ICT state, indicating that the observed nonlinearity is dominated by the ICT contribution rather than the SFCT one. Re(γ) is uniformly larger in **TMC-3’- EH** than **TMC-2**, with the exception of ~775 nm where **TMC-2** benefits from significant one-photon enhancement. At the static limit, Re(γ) of **TMC-3’-EH** is two orders of magnitude larger than that of **TMC-2**.

The off-resonant results can be understood in the context of a 3-state description (eq. 3.5) of Re(γ), where μ_{0n} is the transition moment between states 0 and n, E_{0n} is the energy gap, and $\Delta\mu_{01}$ is the change in state dipole moment. As $\Delta\mu_{01} >> \mu_{01}$ for TICT chromophores, the second (dipolar) term is the primary contributor to Re(γ). Thus, the observed increase in off-resonant Re(γ) is result of the extended π-system length, which causes $\Delta\mu_{01}$ to increase by ~25 D versus in **TMC-2**.

$$\gamma = -\frac{\mu_{01}^4}{E_{01}^3} + \frac{\Delta\mu_{01}^2\mu_{01}^2}{E_{01}^3} + \frac{\mu_{01}^2\mu_{12}^2}{E_{01}^2 E_{02}} \tag{3.5}$$

Table 3.3. Dispersion of average second hyperpolarizability of **TMC-3'-EH** and **TMC-2** computed with CAM-B3LYP/6-31+G**

Wavelength (nm)	**TMC-3'-EH** (10^5 au)	**TMC-2** (10^5 au)
775	-135.4	~10000
900	-178.9	---
1000	1992.5	940.6
1305	50.0	13.3
1550	33.1	2.9
Inf	19.9	0.1

The computed values of Re(γ), are much larger than the experimental results. This discrepancy may be related to the intermolecular aggregation interactions in the Z-scan solutions which are absent in the computation. As noted earlier, there is significant aggregation which can blue-shift the ICT energy >0.2 eV. By eq. 5, this will result in at least a ~25% decrease in Re(γ). It is difficult to reliably ascertain the exact peak position in Z-scan solution due to overlap with the much stronger SFCT band, but based on the solvatochromic shift between CH_2Cl_2 and MeOH, a ~80 nm (0.5 eV) blue shift would not be unreasonable, and would result in a ~50% decrease in Re(γ). In an effort to confirm this theory, Re(γ) was computed for the head-to-tail (HT) dimer of **TMC-3'-EH**, a motif which constitutes the central unit in the crystallographic cell of similar compounds.

The resulting Re(γ) = 27.8 × 10^5 au (normalized per chromophore) is similar to that of the monomeric species. However, a true comparison would include a higher order aggregate including solvent effects, which unfortunately is an extensive undertaking outside the scope of this work.

3.4 Conclusions. We have investigated the 3rd and 5th order nonlinear optical response of the hybrid TICT/stilbene chromophore, **TMC-3'**, finding that the orbitals related to the stilbene fragment lead to significant 2PA not previously observed in TICT systems. In contrast to previous TICT results, the NLR here is almost entirely related to the change in polarizability between the ground and 2P excited state, which may in turn depend strongly on the identity of the central aromatic ring, as well as the ground and excited state torsional angles. Experimental results on highly aggregated solutions differ significantly from the computed 3rd order response of monomeric species, which indicate that the stilbene fragment is a productive modification for increasing Re(γ). This work suggests that while extended conjugation may ultimately increase Re(γ), it also introduces strong dipolar aggregation which impacts the 3rd order NLO response, and that the identity of the conjugated linker plays a central role in 2PA.

Chapter 4. Molecular Design Principles for Magneto-Electric Materials: All-Electric Susceptibilities Relevant to Optimal Molecular Chromophores

Reproduced with permission from:

Lou, Alexander J.-T.; Dreyer, Elizabeth; Rand, Stephen; Marks, Tobin J. *Journal of Physical Chemistry C*, **2017**, *121*, 16491-16500.

This work was performed in collaboration with the co-authors listed above.

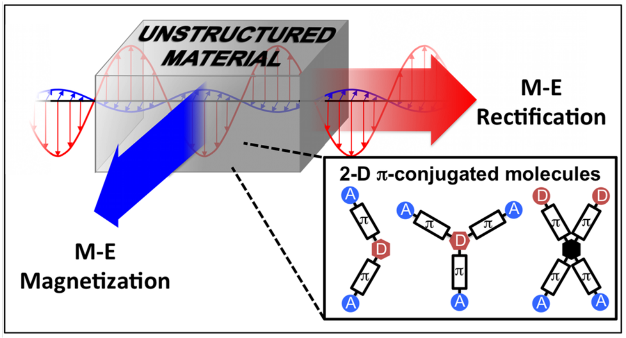

Abstract. Magneto-electric (M-E) response at the molecular level arises from the interaction of matter with the electric and magnetic fields of light, and can manifest itself as nonlinear M-E magnetization (M_{NL}) or M-E rectification (P_{NL}). However, there is presently a limited understanding of how molecular material properties impact M-E response. Here we investigate the relationship between M-E nonlinear coefficients and the third-order electric susceptibility, $\chi^{(3)}$, finding that M_{NL} is proportional to $\chi_{xxxx}^{(3)}$, while P_{NL} scales with $\chi_{zzxx}^{(3)}$ due to a cascaded nonlinearity. By applying a sum-over-states (SOS) expression for the elements of $\chi^{(3)}$ to valence-bond charge-transfer (VB-CT) models, we formulate practical guidelines for the design of materials expected to exhibit enhanced M-E properties. On this basis, we predict that many conventional nonlinear optical chromophores with large values of $\chi_{xxxx}^{(3)}$ may be suitable for generating optical magnetism at low intensities. In the case of M-E rectification, analysis of *Λ*-shaped, *X*-shaped, and octupolar VB-CT models suggests that their molecular structures can be tuned to enhance the response by maximizing $\chi_{zzxx}^{(3)}$. In particular, octupolar molecules with a predominantly CT character ground state and *Λ* -shaped chromophores with weakly conjugated bridges between donor and acceptor moieties should promote off-diagonal nonlinearity and M-E rectification.

4.1 Introduction. A multitude of useful phenomena arise from the interaction of matter with intense light fields. Those resulting from the electric field component of the light are the subject of conventional nonlinear optics (NLO), have been studied for several decades, and find application in a myriad of photonics technologies.[1-5,135-138] However, dynamic magnetic interactions are also possible, and can give rise to unique properties such as negative permeability,[139] negative refraction,[140] and the prospects of completely new phenomena or capabilities, including cloaking and super lensing.[141-145] Thus far, magnetic interactions have only been demonstrated in specialized photonic nanostructures and ultra-high energy systems.[146] In unstructured materials, it has long been presumed that the strength of magnetic interactions is unavoidably weak, so that the possibility of nonlinear magneto-electric interactions has gone unexplored. It was only recently that the dynamic magneto-electric (M-E) effects previously neglected in the common description of polarization were shown to be surprisingly strong in dielectric liquids and crystalline solids.[46,147]

Dynamic M-E effects (Figure 4.1) can manifest as magnetization $M_y(\omega)$ or rectification $P_z(\omega)$, both of which have exciting potential applications. Of particular interest here is the possibility of converting light to electricity via M-E rectification, in a capacitive manner that avoids the fundamental limitations of conventional photovoltaic (PV) technologies and substantially circumvents the co-generation of heat.[8] Furthermore, optical magnetization may enable the generation of internal magnetic fields useful for extending the distance over which carrier spin orientation is preserved in spintronic circuitry, or enable ultrafast reading and writing of magnetic memories, or induce negative permeability in natural dielectric materials.[9] The generation of strong, high frequency magnetic fields has been challenging historically,[139] so any advances in magnetism at optical frequencies are likely to afford unforeseen applications.

Polarization contributions from the M-E susceptibility (χ_{ME}) can be described classically by considering the combined forces of electric and magnetic fields, $E_x(\omega)$ and $H_y(\omega)$, exerted on a bound electron by light propagating along the z-axis (Figure 4.1). The induced motion can be

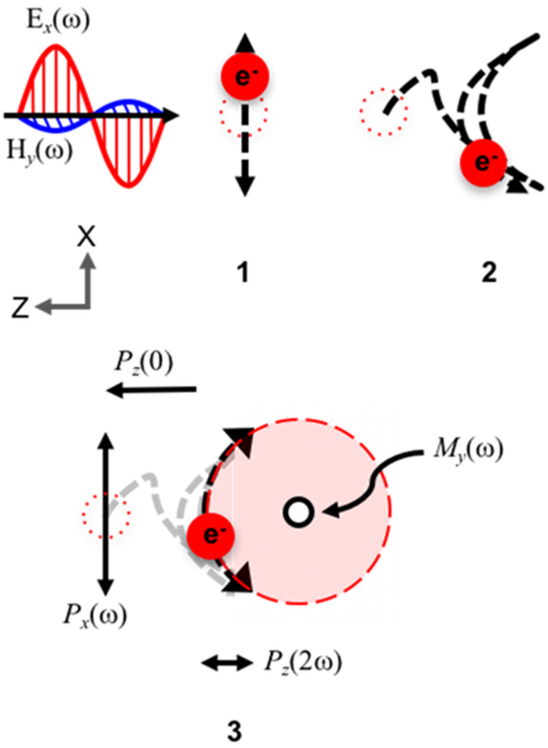

Figure 4.1. Classical depiction of M-E polarization with light propagating from right to left. (1) E-field only initiates motion in the x direction, (2) Lorentz force and parametric enhancement causes displacement along z, (3) final arc-like trajectory produces magnetization in the y direction. Dashed lines depict electron motion and displacement; the labeled arrows are components of polarization and magnetization. The dotted red outlined circle indicates the starting position of the bound electron.

understood as follows: (1) $E_x(\omega)$ initiates electronic motion and displacement parallel to the electric field; (2) the orthogonal $H_y(\omega)$ field imparts a Lorentz force that deflects the motion in the direction of propagation (z-axis); (3) As a result, an electron initially at rest is induced to follow an arc-like trajectory in the xz plane, producing three M-E nonlinearities: magnetization $M_y(\omega)$ rectification $P_z(0)$, and second harmonic generation $P_z(2\omega)$. These three magneto-electric moments thus arise from a 2-step (2-photon) high-field process in which the electric field interaction takes place first, and the magnetic field interaction is second, making them proportional to the electric dipole transition moment.[9] The discovery of these M-E effects calls for a more complete description of nonlinear response that includes second- and third-order M-E contributions ($\chi_{ME}^{(2)}$ and $\chi_{ME}^{(3)}$), as well as conventional first ($\chi^{(1)}$), second ($\chi^{(2)}$), and third-order ($\chi^{(3)}$) all-electric terms (eqs. 4.1 - 4.2).

$$\begin{aligned} P_{NL} &= \varepsilon_0 \left\{ \chi^{(1)} E(\omega) + \chi^{(2)} E(\omega) E(\omega) + \chi^{(3)} E(\omega) E(\omega) E(\omega) + \ldots \right\} \\ &\quad + (1/c) \left\{ \chi_{ME}^{(2)} H(\omega) E(\omega) + \chi_{ME}^{(3)} E(\omega) H(\omega) E(\omega) + \ldots \right\} \end{aligned} \tag{4.1}$$

$$M_{NL} = \left\{ \chi_{ME}^{(2)} E(\omega) H(\omega) + \chi_{ME}^{(3)} E(\omega) H(\omega) E(\omega) + \ldots \right\} \tag{4.2}$$

The details of the quantum theoretical and classical description, as well as numerical simulations of M-E nonlinearity in model systems have been reported in the literature[42,46,148] and M-E magnetization has been observed experimentally as magnetic dipole (MD) scattering in dielectric liquids, crystals and glasses.[43] Recent investigations[42,43] have shown that the strength of induced magnetic scattering depends on the details of the molecular structure, notably the moment of inertia in the case of small molecules in liquids. However, to date, few tools have been available to understand structure-property relationships in M-E materials at the molecular level, and to direct the development of materials with enhanced M-E coefficients for rectification and magnetization. In this contribution, we derive and exploit new relationships between the M-E coefficients for rectification and magnetization and elements of the third-order susceptibility $\chi^{(3)}$ in order to develop useful design criteria. For example, the static polarization created within centrosymmetric materials by M-E rectification is shown to mediate a cascaded nonlinearity combining rectification and an induced electro-optic response that yields nonlinear refraction. An equivalence is established between the M-E coefficient for rectification and the off-diagonal element $\chi_{zzxx}^{(3)}$ of the third-order susceptibility tensor. A similar equivalence is found between the M-E coefficient for magnetization and the diagonal element $\chi_{zzxx}^{(3)}$. These results permit us to employ empirical information and theoretical analysis of structure-function relationships in $\chi^{(3)}$ materials to predict the performance of magneto-electric materials at the molecular level.

In contrast to the scarcity of studies of M-E material response at the molecular level, the design of materials with large $\chi^{(3)}$ values has been an area of intense interest for several decades, and is now a relatively mature field in terms of understanding structure-property relationships.[7] Therefore, establishing a link between magneto-electric and well-studied third-order susceptibilities is highly desirable. To make an explicit connection with chemical models, we begin by recognizing that the macroscopic NLO susceptibility $\chi^{(3)}$ of bulk materials reflects the microscopic second hyperpolarizability γ of their molecular constituents.

$$\chi^{(3)}(-\omega;\omega,-\omega,\omega) = NL^4(\omega)\gamma(-\omega;\omega,-\omega,\omega) \qquad (4.3)$$

In eq. 3,[10] N is the number density of chromophores and $L^4(\omega)$ is the Lorentz local-field factor for a third-order process. In the past, design of high performance NLO chromophores (Figure 4.2) relied on qualitative but pragmatic structure-property relationships, such as the chemically intuitive Sum-Over-States (SOS) expression.[13,35,40,149] The commonly used three-state version of the SOS expression for the diagonal element γ_{xxxx} of the second hyperpolarizability is given by eq. 4.4.[41,109,150]

$$\gamma_{xxxx} \propto -\frac{(\mu_{01}^{x})^4}{E_{01}^3} + \frac{(\mu_{01}^{x}\Delta\mu_{01}^{x})^2}{E_{01}^3} + \frac{(\mu_{01}^{x}\mu_{12}^{x})^2}{E_{01}^2 E_{02}} \qquad (4.4)$$

Here, μ_{ij} is the transition dipole moment between states i and j, $\Delta\mu_{ij}$ is the difference between the state dipole moments μ_i and μ_j, and E_{ij} is the transition energy. Several well-known approaches to increasing γ_{xxxx} stem from this model, such as bond length alternation (BLA), judicious choice of donor and acceptor moieties, disrupted conjugation, or a combination of these approaches.[13,23,34,35,40,151,152]

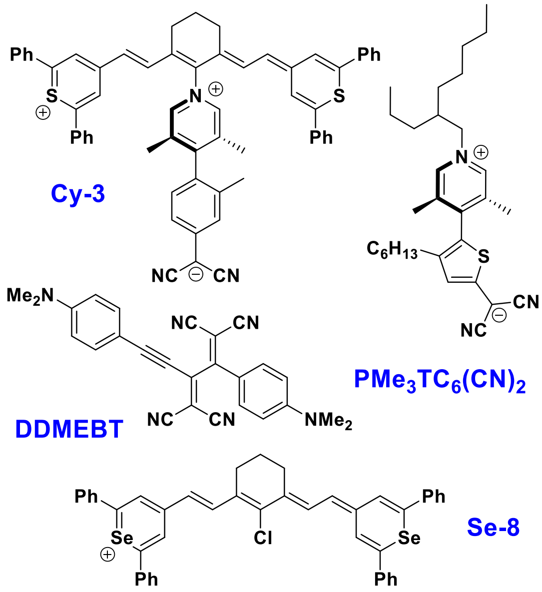

Figure 4.2. Known high-performance third-order NLO chromophores. Hybrid cyanine-twisted π-system (TICT) chromophore, **Cy-3**; TICT chromophore, **PMe$_3$TC$_6$(CN)$_2$**; cross-conjugated chromophore, **DDMEBT**; high performance cyanine chromophore, **Se-8**, are representative materials that emerged by applying a "designer" approach to enhancing NLO response.

In this work, we focus on heuristic valence-bond charge-transfer (VB-CT) models to provide a broadly applicable approach to enhancing specific elements of $\chi^{(3)}$. VB-CT models[153-158] provide a physical description of molecular electronic structure based on the relative contributions of VB and CT resonances to the ground state, and are particularly well-suited to capture the most salient features of molecular NLO response. Previously, the SOS based analysis of dipolar, Λ-shaped, octupolar, and tetrahedral push-pull VB-CT models afforded an improved understanding of lower order polarization in such molecules. The same models can be used to understand third-order polarization.[155-158] In order to create design rules for enhanced M-E rectification or magnetization, we therefore draw on the predictions of a simplified SOS expression applied to VB-CT models for the second hyperpolarizability, γ, after establishing a link between the M-E susceptibilities of main interest here, $\chi_{ME}^{(2)} \equiv \chi^{(eme)}$ and $\chi_{ME}^{(3)} \equiv \chi^{(meme)}$, and elements of the all-electric third-order susceptibility $\chi^{(3)}$.

4.2 Theoretical links between 2nd order and 3rd order nonlinear optical susceptibilities. In this section, we establish an explicit connection between magneto-electric coefficients for P_{NL}, M_{NL} and individual elements of the all-electric susceptibility $\chi^{(3)}$. The constitutive relations for the two magneto-electric (M-E) processes of interest are first expressed in terms of equivalent electric fields. They are then compared with expressions for all-electric four-wave mixing polarizations driven by the same input fields. Finally, correspondences are identified between the various coefficients. In this section, we summarize the results for both M-E rectification and magnetization.

Unlike the polarizations of conventional nonlinear optics that only take electric field components into account, the moments described by constitutive relations of M-E processes contain magnetic fields. For these processes to be compared with all-electric nonlinearities, their fields must be converted to equivalent electric fields in accordance with Maxwell's equations. For *x*-polarized light propagating along the *z*-axis the transverse components are found from Faraday's Law to be related by

$$H_y^* = -E_x^* / \eta_0, \tag{4.5}$$

where η_0 is the electromagnetic impedance. This relation is therefore used throughout the present work to convert the moments encountered in M-E rectification and M-E magnetization to equivalent, all-electric expressions.

We begin by clarifying notation and the order of the two main susceptibilities on which this analysis focuses. The susceptibility governing ME rectification mediates a second-order polarization

$$P_{NL} = (1/c)\chi^{(eme)} H^{*} E \tag{4.6}$$

as given in eq. 4.1. The coefficient $\chi^{(eme)}$ has superscripts that specify the electric (*e*) or magnetic (*m*) character of the fields involved in the nonlinearity, ordered from right to left in sequence. Thus *eme* specifies an electric field followed by a magnetic field, ultimately producing an electric polarization. The second-order induced magnetization M_{NL} has a similar form (eq. 4.7).

$$M_{NL} = \chi^{(mme)} H^{*} E . \tag{4.7}$$

However, the tensor element $\chi^{(mme)}$ for radiative magnetization vanishes in centrosymmetric media when conventional symmetry analysis is applied and is small even when dynamic symmetry-breaking[148] is taken into account. Classically, the largest non-vanishing contribution to transverse (radiative) magnetization at the optical frequency is therefore of higher order, namely

$$M_{NL} = \chi^{(meme)} E H^{*} E . \tag{4.8}$$

In eqs. (4.6) and (4.8), magneto-electric responses, P_{NL} and M_{NL}, are driven jointly by the electric field *E* and the magnetic field *H* of light,[148,159,160] but their frequencies differ since the former is second-order while the latter is third-order. P_{NL} is obtained by combining field components E and H^{*} at frequencies ω and $-\omega$ respectively to form a static field. *M* on the other hand oscillates at the optical frequency ω since it results from the combination of three optical frequencies ($\omega = \omega - \omega + \omega$).

Introducing equivalent fields as prescribed by eq. (4.5), the amplitude of M-E rectification becomes

$$P_z^{(2)} = -\varepsilon_0 \chi_{zyx}^{(eme)} E_x^* E_x . \tag{4.9}$$

The indices on the susceptibility tensor refer to the original orientation of the fields, not the equivalent fields, because this element is determined by the actual input field directions rather than their equivalents. Also, there is no Einstein convention regarding repeated indices once index assignments have been made. Cascaded M-E rectification with induced electro-optic response results in the third-order polarization

$$P_z^{(3)}(\omega) = \varepsilon_0 \left\{ \frac{[\chi_{zyx}^{(eme)}(0;-\omega,\omega)]^2}{\varepsilon_{zz}(0)-1} \left(\frac{E_x^*(-\omega)E_x(\omega)}{E_z^*(-\omega)E_z(\omega)} \right) \right\} E_z(\omega) E_x^*(-\omega) E_x(\omega). \tag{4.10}$$

For third-order M-E magnetization, eq. (4.8) immediately leads to the equivalent expression

$$M_y^{(3)} = -(\chi_{yxyx}^{(meme)} / \eta_0) E_x E_x^* E_x . \tag{4.11}$$

To make a comparison between magneto-electric rectification or magnetization and all-electric nonlinear polarizations, it is just as important to convert the left-hand sides of the constitutive relations to polar vector fields as the right sides. While this is already the case in eq. 4.10, it is not true in eq. (4.11), where the left-hand side is an axial vector. Hence the magnetization must also be converted to an equivalent electric field consistent with Maxwell's equations. An argument based on Ampere's Law is used to show that $M_y = -cP_x$. Substitution of this into eq. (4.11) yields a satisfactory all-electric equivalent expression for third-order magnetization, which is

$$P_x^{(3)}(\omega) = \varepsilon_0 \chi_{yxyx}^{(meme)} E_x(\omega) E_x^*(-\omega) E_x(\omega) \tag{4.12}$$

Finally, by comparing the polarizabilities in eqs. (4.10) and (4.12) with four-wave mixing expressions with the same input driving fields, the key results of this paper may be obtained.

Magneto-electric coefficients $\chi_{zyx}^{(eme)}$ and $\chi_{yxyx}^{(meme)}$ are found to obey the following equivalence relations with respect to third-order, all-electric susceptibility elements.

$$\left\{\frac{[\chi_{zyx}^{(eme)}(0;-\omega,\omega)]^2}{\varepsilon_{zz}(0)-1}\left(\frac{E_x^*(-\omega)E_x(\omega)}{E_z^*(-\omega)E_z(\omega)}\right)\right\} = \chi_{zzxx}^{(3)} \tag{4.13}$$

$$\chi_{yxyx}^{(meme)} = \chi_{xxxx}^{(eeee)} \tag{4.14}$$

The expressions in eqs. (4.13) and (4.14) establish specific relationships between M-E susceptibilities and third-order susceptibilities which are non-zero in all crystal classes. Due to the extensive prior work on measurement and prediction of third-order susceptibility elements, including analysis of the relationship between structure and function at the molecular level, these connections allow us to formulate guidelines for detailed design of magneto-electric materials at the molecular level. The equivalence relations also imply that magneto-electric rectification and magnetization are universally allowed in dielectric materials of arbitrary crystal symmetry.

4.3 Designing molecular materials to enhance $\mathbf{M_{NL}}$. Given eq. (4.14), we may develop design criteria for enhanced M-E magnetization based on the objective of maximizing the diagonal third-order tensor component $\chi_{xxxx}^{(3)}$ (or the second hyperpolarizability element γ_{xxxx}). Serendipitously, γ_{xxxx} governs the response of the vast majority of third-order NLO chromophores, which are essentially one-dimensional in nature (Figure 4.2), and derive their nonlinearities from low-energy excitations within a π-conjugated backbone.[12,110] A great deal of experimental effort has been directed to optimizing γ_{xxxx} over the past few decades, so we may immediately conclude that *based on the equivalence relations developed in Section 2, those molecules which exhibit large diagonal third-order nonlinearities are likely to have a large M-E magnetization coefficient.*

4.4 Designing molecular materials to enhance $\mathbf{P}_{\mathbf{NL}}$. The relationship between M-E rectification and off-diagonal third-order tensor components $\chi^{(3)}_{zzxx}$ (or γ_{zzxx}), shown in eq. (4.13), is more challenging to exploit for material design. Historically, far less attention has been paid to the off-diagonal elements of γ, as they have no special significance in conventional NLO. To identify promising classes of molecules, we first draw upon literature concerning the lower order polarization, β. Although it is well known that the specific requirements for enhanced γ_{xxxx} and β_{xxx} are different, the general prerequisites for large β_{xxz} and β_{zxx} are similar to those for γ_{zzxx}.[51,161] Both require transition and/or state dipole moments along two axes, and therefore a two-dimensional molecular structure. Thus, we select X-shaped, Λ-shaped, and octupolar molecules as subjects of investigation, based on several literature reports of large off-diagonal hyperpolarizabilities.[55,162-168] Figure 4.3 shows examples of high performance and archetypal 2-D chromophores that exhibit the basic attributes required for large γ_{zzxx}. In this section, we identify some intriguing design guidelines for γ_{zzxx} based on the structure types in Figure 4.3 by applying a three-state SOS/VB-CT model.

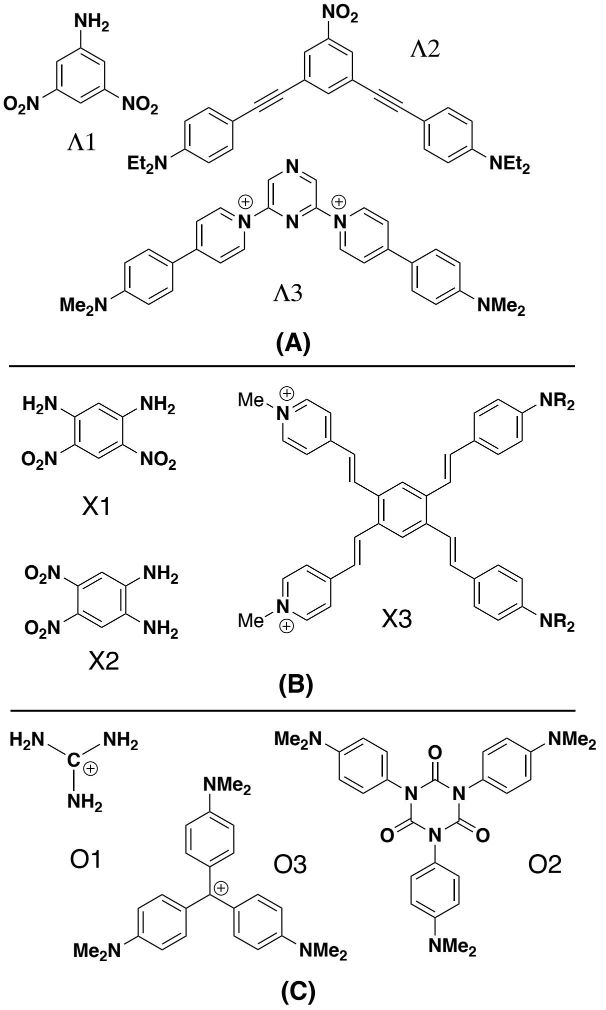

Figure 4.3. Examples of chromophores exhibiting large off-diagonal hyperpolarizability. **Λ1**, **X1**, **X2**, **O1, O2** are archetypal chromophores; the remaining structures represent more elaborate extensions. Counterions are omitted for clarity. **A**) Λ-shaped[163,164]; **B**) X-shaped[165]; **C**) octupolar[55,162].

4.4.1 Three-state SOS expression and VB-CT approach. To identify specific molecular attributes leading to enhanced γ_{zzxx}, we compute γ_{zzxx} for Λ-shaped, octupolar, and X-shaped VB-CT models using a three-state SOS expression. The VB and CT resonances of these systems are shown in Figure 4.4. Using these resonances as a basis set we can construct a three-state Hamiltonian (see eq. (4.15) below) for Λ-shaped and X-shaped molecules, from which we derive transition moments, excitation energies, and state dipole moments required to evaluate γ_{zzxx}. A similar four-state Hamiltonian

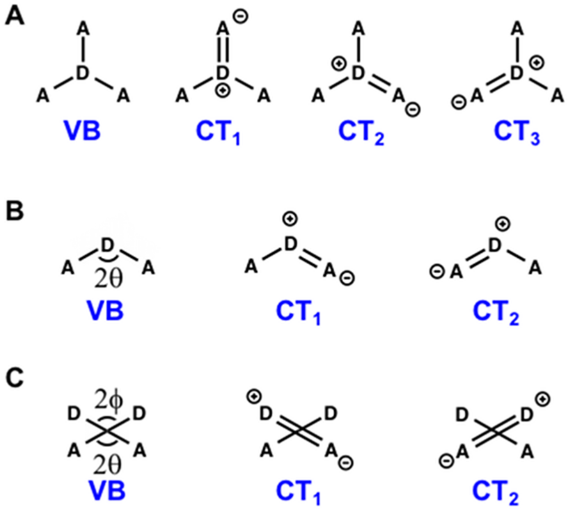

Figure 4.4. VB and CT contributions to γ_{zzxx} in the (A) octupolar; (B) Λ-shaped; (C) X-shaped structures used for this analysis.

yields the same information for octupolar molecules. We define E_{VB} and E_{CT} as the energies of the VB and CT configurations and $\Delta E = E_{VB} - E_{CT}$. $T = \langle CT_1|H|CT_2\rangle$, and $t = \langle VB|H|CT_1\rangle = \langle VB|H|CT_2\rangle$ are the transfer integrals, which represent the mixing of CT₁/CT₂ and CT/VB states respectively.

$$H = \begin{pmatrix} E_{VB} & -t & -t \\ -t & E_{CT} & -T \\ -t & -T & E_{CT} \end{pmatrix} \tag{4.15}$$

One key metric in this analysis is the charge transfer character of the ground state, denoted l, which quantifies the weight of the CT configuration in the ground state. In literature l is defined as in eq. (4.16) below, where $n+1$ is the order of the Hamiltonian matrix.[155]

$$l \equiv \frac{1}{2n} - \frac{\Delta E - (n-1)T}{2n\sqrt{(\Delta E - (n-1)T)^2 + 4nt^2}} \tag{4.16}$$

The relevant transition and state dipole moments for dipolar, quadrupolar, octupolar, and *Λ*-shaped VB-CT models are available in the literature.[155-158]

In general, three essential states are found to be sufficient in describing NLO response,[150,155,169] so in order to calculate γ_{zzxx}, we consider a three-state expression derived from the full SOS theory.[110,170] This expression is

$$\begin{aligned}
\gamma_{zzxx} = {} & -4\left[\frac{\left(\mu_{01}^{z}\right)^{2}\left(\mu_{01}^{x}\right)^{2}}{E_{01}^{3}}+\frac{\left(\mu_{02}^{z}\right)^{2}\left(\mu_{02}^{x}\right)^{2}}{E_{02}^{3}}+\frac{\mu_{01}^{x}\mu_{01}^{z}\mu_{02}^{x}\mu_{02}^{z}}{E_{01}^{2}E_{02}}+\frac{\mu_{01}^{x}\mu_{01}^{z}\mu_{02}^{x}\mu_{02}^{z}}{E_{01}E_{02}^{2}}\right] \\
& +2\left[\frac{\mu_{01}^{x}\mu_{01}^{z}\Delta\mu_{01}^{x}\Delta\mu_{01}^{z}}{E_{01}^{3}}+\frac{\left(\mu_{01}^{z}\right)^{2}\left(\Delta\mu_{01}^{x}\right)^{2}}{E_{01}^{3}}+\frac{\mu_{02}^{x}\mu_{02}^{z}\Delta\mu_{02}^{x}\Delta\mu_{02}^{z}}{E_{02}^{3}}+\frac{\left(\mu_{02}^{z}\right)^{2}\left(\Delta\mu_{02}^{x}\right)^{2}}{E_{02}^{3}}\right] \\
& +2\left[\frac{\mu_{01}^{x}\mu_{01}^{z}\mu_{12}^{x}\mu_{12}^{z}}{E_{01}^{2}E_{02}}+\frac{\left(\mu_{01}^{z}\right)^{2}\left(\mu_{12}^{x}\right)^{2}}{E_{01}^{2}E_{02}}+\frac{\mu_{02}^{x}\mu_{02}^{z}\mu_{12}^{x}\mu_{12}^{z}}{E_{01}E_{02}^{2}}+\frac{\left(\mu_{02}^{z}\right)^{2}\left(\mu_{12}^{x}\right)^{2}}{E_{01}E_{02}^{2}}\right] \\
& +2\left[\begin{array}{l}\dfrac{\mu_{01}^{z}\Delta\mu_{01}^{x}\mu_{12}^{z}\mu_{02}^{x}}{E_{01}^{2}E_{02}}+2\dfrac{\mu_{01}^{x}\Delta\mu_{01}^{z}\mu_{12}^{z}\mu_{02}^{x}}{E_{01}^{2}E_{02}}+\dfrac{\mu_{01}^{x}\Delta\mu_{01}^{z}\mu_{12}^{x}\mu_{02}^{z}}{E_{01}^{2}E_{02}} \\ +\dfrac{\mu_{02}^{z}\Delta\mu_{02}^{x}\mu_{12}^{z}\mu_{01}^{x}}{E_{01}E_{02}^{2}}+2\dfrac{\mu_{02}^{x}\Delta\mu_{02}^{z}\mu_{12}^{z}\mu_{01}^{x}}{E_{01}E_{02}^{2}}+\dfrac{\mu_{02}^{x}\Delta\mu_{02}^{z}\mu_{12}^{x}\mu_{01}^{z}}{E_{01}E_{02}^{2}}\end{array}\right] \quad . \qquad (4.17)
\end{aligned}$$

As with the three-state model for γ_{xxxx}, eq. (4.17) can be organized into distinct and physically meaningful terms (shown in brackets) the first three of which are denoted as negative, dipolar, and two-photon respectively. Although the detuning denominators in the resonant SOS expression[150] for γ suggest that M-E susceptibility is frequency-dependent and potentially resonantly enhanced, we limit our discussion to the static case.

4.4.2 Λ-Shaped molecules (Figure 4.3A). Substitution of the relevant transition moments,[158] state dipole moments, and energies into eq. (4.17) yields an expression for γ_{zzxx} for any *Λ*-shaped molecule, as given by eq. (4.18). Valence band and charge transfer state configurations are illustrated for such molecules in Figure 4.4B.

$$\gamma_{zzxx} = \mu^4 \sin^2(\theta)\cos^2(\theta)\left[\frac{2l(1-2l)^2}{\left(2T+t\sqrt{1/l-2}\right)^3}+\frac{2l^{3/2}(1-2l)^{5/2}}{t\left(2T+t\sqrt{1/l-2}\right)^2}\right] \tag{4.18}$$

In Figure 4.5 the values of γ_{zzxx} calculated from eq. (4.18) are plotted versus the CT character of the ground state, in the range $0 < l < 0.5$. Other quantities appearing in eq. (4.18) include the half-angle θ between the two CT axes (see Figure 4.4B) and the magnitude of the dipole moment θ for the CT configuration. Only two terms from eq. (4.17) are non-zero, so that γ_{zzxx} depends solely on a dipolar and “triangle” contribution. Because there is no contribution from the two-photon and negative terms, the present design rules are more likely to follow those for dipolar chromophores such as **PMe$_3$TC$_6$(CN)$_2$** (Figure 4.2) rather than chromophores relying on large transition moments of low-lying excitations as in **Se-8** (Figure 4.2) which derive their nonlinearity primarily from the negative term.[13]

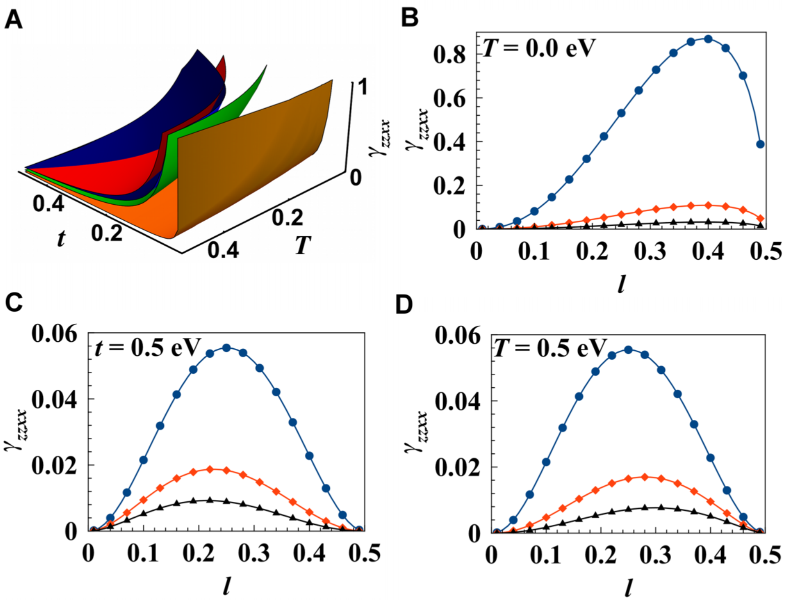

Figure 4.5. Λ-shaped and X-shaped chromophore γ_{zxzx} dependence on parameters l (charge transfer character), t, T. All values of l, t, T are expressed in eV, and γ_{zxzx} is in arbitrary units. (A) Dependence of γ_{zxzx} on t and T for $l = 0.01$ (orange), 0.1 (green), 0.2 (red), 0.3 (blue). Plots of l vs γ_{zxzx} in arbitrary units; (B) $T = 0$, $t = 0.5$ (circles), 1.0 (diamonds), 1.5 (triangles); (C) $t = 0.5$, $T = 0.5$, 1.0, 1.5; (D) $T = 0.5$, $t = 0.5$, 1.0, 1.5.

With eq. (4.18) in hand, we can investigate the dependence of γ_{zzxx} on l, t, and T (Figure 4.5). Figure 4.5A reveals an inverse relationship between γ_{zzxx} and t for all values of l. Broadly speaking, t refers the ability of the bridge connecting donor and acceptor fragments to efficiently mix the parent orbitals. In a physical sense, small values of t indicate a "purer" VB or CT character of the ground state, meaning that the resulting HOMO closely resembles one of the parent orbitals. As such, bridging motifs which result in poor electronic connectivity between donor and acceptor are likely to effectively lower t. Some of these are illustrated in Figure 4.6.

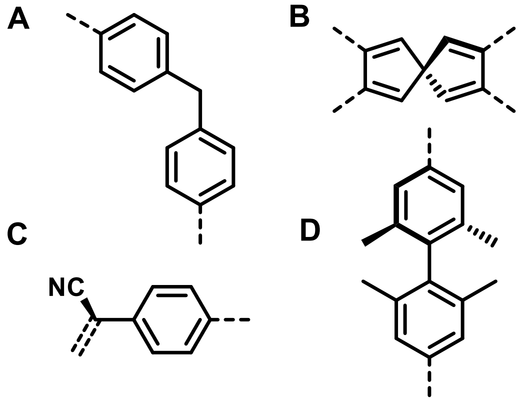

Figure 4.6. Bridging motifs exhibiting poor or disrupted conjugation. (A) spatial separation; (B) torsion enforced by structural connectivity; (C, D) torsion enforced by steric repulsion

Twisted π-systems (TICT; Figure 4.2) are well known to yield small t values, and to produce HOMOs that closely resemble the parent donor orbitals.[38,171,172] In TICT molecules, the inefficient electronic connectivity is evidenced by a weak charge transfer excitation relative to analogous planar molecules, and as the torsional angle is increased, the HOMO and LUMO become increasingly localized, consistent with decreased t.[33,36] Very large second- and third-order NLO response has been predicted and realized in donor-π-acceptor (D-π-A) chromophores with disrupted conjugation, including TICT chromophores and spiro-conjugated molecules.[28-30,40,173] Such observations are further supported by quantum graph studies of Kuzyk and Lytel, where they demonstrate that phase disruption can enhance NLO response.[23,24] Therefore, we recognize that the observed relationship in Figure 4.5A is consistent with previous experimental and theoretical work, and that t is a critical factor in enhancing γ.

At large values of l, γ_{zzxx} also exhibits an inverse dependence on T. While the same strategies can be employed to reduce T, the use of isolated D-π-A pairs can achieve the same effect. In structures such as **Λ1** (Figure 4.3A) the shared donor moiety mediates CT_1/CT_2 mixing, likely resulting in a large value of T. However, structures which contain two D-π-A pairs, such as molecule **Λ 2** (Figure 4.3A), may reasonably be approximated by $T = 0$ due to the lack of electronic connectivity.

The general dependence of γ_{zzxx} on l varies over a range of T and t values (Figures 4.5B-D). When $t = 0.5$ eV (Figure 4.5C), increasing T leads to a slight decrease in the optimal CT character; when $T = 0.5$ eV (Figure 4.5B), increasing t causes a slight increase in optimal CT character; when $T = 0$ (Figure 4.5B), very large CT character results in the largest γ_{zzxx} regardless of the t value. *For the cases shown in Figures 4.5D and 4.5C, an intermediate CT contribution is required for enhancing* γ_{zzxx}*, and in the case of Figure 5B, structures with predominantly CT character will have the highest* γ_{zzxx} *for any value of* t. The need for intermediate l suggests that a tradeoff between l and t is critical to obtaining the optimum performance since simply minimizing t would result in a purely CT or VB ground state, with $l = 0$ or $l = 0.5$. With exception of case 4.5B, careful manipulation of the bridging moiety is required to achieve the optimum performance. However, if the D-π-A pairs can be separated, then simply minimizing t could prove to be a rewarding approach. Because a large degree of CT character is desired in this case, *it is imperative that the*

CT state be lower in energy than the VB state so that it may contribute strongly to the ground state character. This point is discussed in more detail in Section 4.4.4.

The design rules pertaining to the positioning of donor and acceptor moieties are much more straightforward. By inspection of eq. (4.18) note that γ_{zzxx} increases as θ approaches 45°, although from a practical standpoint, upwards of 75% of the maximum performance can be achieved within ±15°. Therefore, systems with sp^2 hybridized carbon and *meta*-substituted six-membered aromatics (both θ = 60°), *ortho*-substituted five-membered heterocycles (θ = 36°), and *ortho*-substituted six-membered aromatics (θ = 30°) have the appropriate geometry for a large response.

4.4.3 X-shaped molecules (Figure 4.3B). If the charge transfer *between* adjacent D-π-A pairs can be neglected compared to the charge transfer *within* a pair, the effective Hamiltonians for *X*-shaped and *Λ*-shaped chromophores (Figures 4.3A, B) are identical, giving rise to the same eigenvalues and eigenfunctions. This is reasonable in the case of *meta* versus *para* CT in arenes[166] (see structure **X2**), although it may not hold for cases such as structure **X1** (Figure 4.3B), which likely requires a five-state analysis. Making the usual assumption that $\langle VB|\hat{\mu}|CT_1\rangle = \langle VB|\hat{\mu}|CT_2\rangle = \langle CT_1|\hat{\mu}|CT_2\rangle = 0$, we derive state and transition dipole moment equations and substitute them into eq. (4.15) to obtain eq. (4.19).

$$\gamma_{zzxx} = \mu^4(\sin\theta + \sin\phi)^2(\cos\theta + \cos\phi)^2 \times \left[\frac{2l(1-2l)^2}{\left(2T + t\sqrt{1/l-2}\right)^3} + \frac{2l^{3/2}(1-2l)^{5/2}}{t\left(2T + t\sqrt{1/l-2}\right)^2}\right] \tag{4.19}$$

In eq. (4.19), θ is the half-angle between the two acceptor groups, and ϕ the half-angle between the two donor substituents. Again, the optimal angle is θ = ϕ = 45°. Ultimately, the analysis at this level leads to the same results for *X*- and *Λ*-shaped chromophores in terms of dependence on *l, T,*

t, and θ (Figure 4.5). One particular difference is the separation of the two CT states; here the assumption that T is very small is implicit in our model, since the two D-π-A pairs are taken as non-interacting. In this sense, we would expect an *X*-shaped chromophore to be described best by Figure 4.5B, and to have the highest performance when l approaches ½, and t is very small.

Based on the μ^4 term in eq. 4.18, *X*-shaped chromophores offer higher potential γ_{zzxx} than *Λ*-shaped analogues due to the enhanced CT dipole moments arising from additional donor or acceptor groups. Furthermore, there is reason to expect that *X*-shaped chromophores will provide large γ_{zzxx} values judging from literature reports on two-dimensional tetraethynylenthenes (TEE). Such molecules demonstrate large γ, and although the contribution of specific tensor elements has not yet reported, the two-dimensional arrangement of donor and acceptor moieties is well-situated for off-diagonal response.[174-176]

4.4.4. Octupolar molecules (Figure 4.3C). The relevant transition moments and energies for octupolar molecules were derived by Cho et al,[156,157] and utilized for a brief investigation of γ_{zzxx}.[156] Here, we investigate this model more explicitly, particularly in terms of t and l in order to create more general guidelines. Because the relevant transition and state dipole moments all have x and z components, all terms in eq. (4.17) contribute to γ_{zzxx} for octupolar molecules. The expression reduces to

$$\gamma_{zzxx} = \frac{3\mu^4\left(l - \frac{9}{4}l^2\right)}{8\left(3T + t\left(\sqrt{1/l - 3}\right)\right)^3}. \tag{4.20}$$

In eq. (4.20) the magnitudes of t and T have little impact on the overall behavior of γ_{zzxx} with respect to l. *Across a broad range of* t *and* T*, the maximum value of* γ_{zzxx} *occurs at* $l = 1/3$. The design parameters are then straightforward; increasing CT character while lowering t and T is clearly the key to higher performance (Figure 4.7). Thus, it may be useful to employ a segmented or multiple donor/acceptor paradigm to reduce T; for example, moving from **O3** to **O2** (Figure 4.3C) allows a degree of isolation between CT states. Similar to the Λ-shaped and X-shaped cases, γ_{zzxx} exhibits an inverse dependence on t (Figure 4.7A). Therefore, the same disrupted conjugation pathways suggested in Section 4.4.2 should apply to octupolar structures as well. However, in this case there is no tradeoff between l and t, so t can simply be minimized. *Finally, the strong CT character of the ground state, in the absence of significant VB/CT mixing, requires that the CT resonance be lower in energy than the VB resonance.* Such structures with high CT character are known in the literature and can be readily identified by their strong, negative solvatochromism.[80] In these cases, the CT state may be stabilized by aromaticity, inductive effects, charge delocalization, or interactions with the chromophore environment.[177-181] Another approach is to destabilize the VB resonance by introducing geometric constraints.[28,29,182]

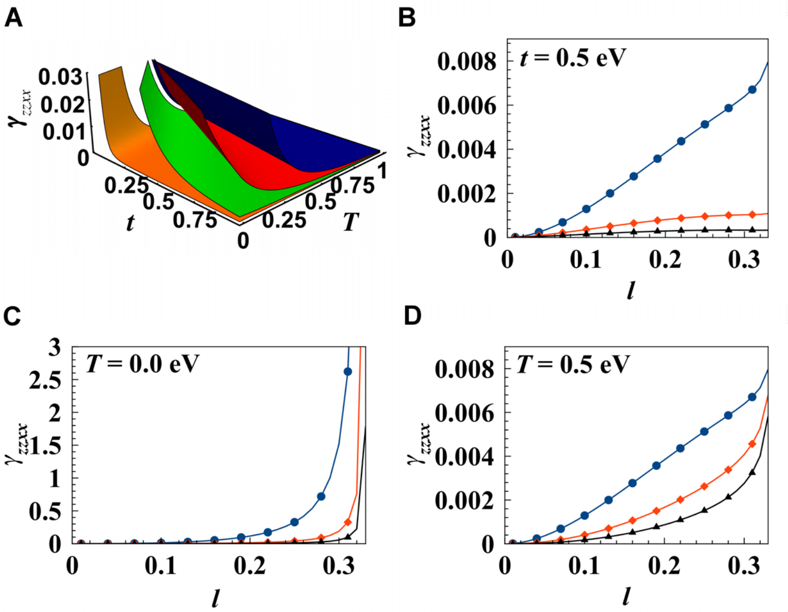

Figure 4.7. Octupolar chromophore γ_{zzxx} dependence on l, t, T. All values of l, t, T are expressed in eV and γ_{zzxx} is in arbitrary units. (A) Dependence of γ_{zzxx} on t and T for $l = 0.01$ (orange), 0.1 (green), 0.2 (red), 0.3 (blue). Plots of l vs γ_{zzxx} in arbitrary units; (B) $T = 0$, $t = 0.5$ (circles), 1.0 (diamonds), 1.5 (triangles); (C) $t = 0.5$, $T = 0.5$, 1.0, 1.5; (D) $T = 0.5$, $t = 0.5$, 1.0, 1.5.

4.4.5 VB-CT Conclusions. SOS based analysis of the VB-CT models discussed here provides intriguing molecular structure-based design criteria for optimizing molecular M-E polarization. Specifically,

(i) For each structure type, γ_{zzxx} is proportional to μ^4, so inclusion of strong donor and acceptor moieties, and extension of the CT spatial length will be beneficial insofar as it does not negatively impact VB/CT mixing.[22,57,110,183,184]

(ii) A brief inspection of ϕ and θ reveals the optimal geometry for off-diagonal response is accessible through common organic molecular structural geometries.

(iii) The complex dependency of γ_{zzxx} on l suggests that for Λ- and X-shaped chromophores, moderate to large l leads to large, positive γ_{zzxx}. For octupolar molecules, l must simply be maximized. In both cases, it is clear that enhanced CT character in the ground state must be targeted (discussed in Sections 4.4.2 and 4.4.4) by lowering the CT state energy or raising the energy of the VB state.

(iv) The inverse dependence on T and t suggests that bridging motifs (Figure 4.6) which disrupt conjugation will lead to enhanced NLO performance, though care must be taken to maintain the optimal CT character.

In general, many of the same conceptual avenues used for conventional NLO chromophores should be productively applicable to new chromophore geometries designed to achieve enhanced M-E rectification.

4.5 Summary. Magneto-electric magnetization and rectification processes at the molecular level are relatively new nonlinear effects for which the design principles are absent in the scientific literature. Here we have demonstrated a relationship between the all-electric susceptibility elements $\chi^{(3)}_{xxxx}$ and $\chi^{(3)}_{zzxx}$, and the two lowest-order magneto-electric processes, magnetization and rectification respectively, and have exploited it to outline strategies for enhancing these effects. For example, cyanines and typical 1-D donor-π-acceptor chromophores are predicted to be good candidates for M-E magnetization, given their very large values of $\chi^{(3)}_{xxxx}$. In fact, many of the current high performance third-order NLO materials are likely to exhibit strong induced M-E magnetization.

In the case of M-E rectification, the guidelines for optimal material synthesis are less specific. There has been little investigation to date of anisotropic hyperpolarizability elements such as γ_{zzxx}, so it is difficult to identify chromophores suitable for M-E rectification. Our analysis of γ_{zzxx} in VB-CT models has nevertheless identified rational design criteria for three common structure types, which are by no means exhaustive. From this result, it is clear that a significant CT contribution to the ground state is necessary, as are large static dipole moments. Extending conjugation, increasing D/A strength, and disrupting conjugation are all promising tools for tuning the CT contribution in the context of Λ-shaped, X-shaped, and octupolar molecules. On the other hand, these design rules are far from complete. Excited state charge transfer dynamics have not been addressed in this analysis, although they are likely to be an important component of M-E response. From an experimental standpoint, the finding that large static dipole moments may increase the value of $\chi^{(3)}_{zzxx}$ could prove to be problematic for the interpretation of scattering experiments, as internal moments facilitate molecular alignment by applied electric fields thereby altering the depolarization ratio which may otherwise be determined by magneto-electric processes. Nevertheless, the present work should serve as the first step towards the rational design of M-E materials exhibiting enhanced nonlinearity that can be tailored to meet specific magneto-electric applications.

References.

(1) Dalton, L. R. Nonlinear Optical Polymeric Materials: From Chromophore Design to Commercial Applications. *Adv. Polym. Sci.* **2002**, *158*, 1-76.

(2) Koos, C.; Vorreau, P.; Vallaitis, T.; Dumon, P.; Bogaerts, W.; Baets, R.; Esembeson, B.; Biaggio, I.; Michinobu, T.; Diederich, F.; al, e. All-Optical High-speed Signal Processing with Silicon–Organic Hybrid Slot Waveguides. *Nat. Photonics* **2009**, *3*, 216-219.

(3) Lee, M.; Katz, H.; Erben, C.; Gill, D.; Gopalan, P.; Heber, J.; McGee, D. Broadband Modulation of Light by Using an Electro-Optic Polymer. *Science* **2002**, *298*, 1401-1403.

(4) Raymo, F. M.; Giordani, S. All-optical Processing with Molecular Switches. *P. Natl. Acad. Sci.* **2002**, *99*, 4941-4944.

(5) Shi, Y.; Zhang, C.; Zhang, H.; Bechtel, J.; Dalton, L.; Robinson, B. H.; Steier, W. Low (Sub-1-Volt) Halfwave Voltage Polymeric Electro-optic Modulators Achieved by Controlling Chromophore Shape. *Science* **2000**, *288*, 119-122.

(6) Starosielski, N.: *The Undersea Network*; Duke University Press: Durham NC, 2015.

(7) Marder, S. R. Organic Nonlinear Optical Materials: Where We Have Been and Where We are Going. *Chem. Commun.* **2006**, 131-134.

(8) Fisher, W. M.; Rand, S. C. Optically-Induced Charge Separation and Terahertz Emission in Unbiased Dielectrics. *J. Appl. Phys.* **2011**, *109*, 064903.

(9) Rand, S. C. Quantum Theory of Coherent Transverse Optical Magnetism. *J. Opt. Soc. Am. B* **2009**, *26*, 120-129.

(10) Prasad, P. N.; Williams, D. J.: *Introduction to Nonlinear Optical Effects in Molecules and Polymers*; John Wiley & Sons: New York, 1991.

(11) Benight, S. J.; Bale, D. H.; Olbricht, B. C.; Dalton, L. R. Organic Electro-Optics: Understanding Material Structure/Function Relationships and Device Fabrication Issues. *J. Mater. Chem.* **2009**, *19*, 7466-7475.

(12) Kuzyk, M. G.; Singer, K. D.; Stegeman, G. I. Theory of Molecular Nonlinear Optics. *Adv. Opt. Photonics* **2013**, *5*, 4-82.

(13) Hales, J. M.; Barlow, S.; Kim, H.; Mukhopadhyay, S.; Brédas, J.-L.; Perry, J. W.; Marder, S. R. Design of Organic Chromophores for All-Optical Signal Processing Applications. *Chem. Mater.* **2014**, *26*, 549-560.

(14) Hales, J. M.; Zheng, S.; Barlow, S.; Marder, S. R.; Perry, J. W. Bisdioxaborine Polymethines with Large Third-Order Nonlinearities for All-Optical Signal Processing. *Jounral of the American Chemical Society* **2006**, *128*, 11362-11363.

(15) Gu, B.; Zhao, C.; Baev, A.; Yong, K.-T.; Wen, S.; Prasad, P. N. Molecular Nonlinear Optics: Recent Advances and Applications. *Adv. Opt. Photonics* **2016**, *8*, 328-369.

(16) Stegeman, G. I.; Stegeman, R. A.: *Nonlinear Optics: Phenomena Materials and Devices*; John Wiley & Sons: Hoboken, NJ, 2012.

(17) Dalton, L. Organic Electro-Optic Materials. *Pure Appl. Chem.* **2004**, *76*, 1421-14433.

(18) Kanis, D. R.; Ratner, M. A.; Marks, T. J. Design and Construction of Molecular Assemblies with Large 2nd-Order Optical Nonlinearities - Quantum-Chemical Aspects. *Chem. Rev.* **1994**, *94*, 195-242.

(19) Goodson Iii, T. G.; Pérez-Moreno, J.; Clays, K.; Kuzyk, M. G. Role of the Conjugated Spacer in the Optimization of Second-Order Nonlinear Chromophores. *Proc. SPIE* **2009**, *7413*, 741306-741306-741308.

(20) Gorman, C.; Marder, S. R. Effect of Molecular Polarization on Bond-Length Alternation, Linear Polarizatbiilty, First and Second Hyperpolarizability in Donor-Acceptor Polyenes as a Function of Chain Length. *Chem. Mater.* **1995**, *7*, 215-220.

(21) Meyers, F.; Marder, S. R.; Pierce, B. M.; Bredas, J. L. Electric Field Modulated Nonliear Optical Properties of Donor-Acceptor Polyenes: Sum-Over-States Investigation of the Relationship between Molecular Polarizabilities (a, B, g) and Bond Length Alternation. *J. Am. Chem. Soc.* **1994**, *116*, 10703-10714.

(22) Schmidt, K.; Barlow, S.; Leclercq, A.; Zojer, E.; Jang, S.-H.; Marder, S. R.; Jen, A. K. Y.; Bredas, J.-L. Efficient Acceptor Groups for NLO Chromophores: Competing Inductive and Resonance Contributions in Heterocyclic Acceptors Derived from 2-dicyanomethylidene-3-cyano-4,5,5-trimethyl-2,5-dihydrofuran. *J. Mater. Chem.* **2007**, *17*, 2944-2949.

(23) Lytel, R.; Mossman, S. M.; Kuzyk, M. G. Phase Disruption as a New Design Paradigm for Optimizing the Nonlinear-Optical Response. *Opt. Lett.* **2015**, *40*, 4735-4738.

(24) Perez-Moreno, J.; Zhao, Y.; Clays, K.; Kuzyk, M. G. Modulated Conjugation as a Means for Attaining a Record High Intrinsic Hyperpolarizability. *Opt. Lett.* **2007**, *32*, 59-61.

(25) Albert, I. D. L.; Marks, T. J.; Ratner, M. A. Rational Design of Molecules with Large Hyperpolarizabilities. Electric Field, Solvent Polarity, and Bond Length Alternation Effects on Merocyanine Dye Linear and Nonlinear Optical Properties. *J. Phys. Chem.* **1996**, *100*, 9714-9725.

(26) Albert, I. D. L.; Marks, T. J.; Ratner, M. A. Conformationally-Induced Geometric Electron Localization. Interrupted Conjugation, Very Large Hyperpolarizabilities, and Sizable Infrared Absorption in Simple Twisted Molecular Chromophores. *J. Am. Chem. Soc.* **1997**, *119*, 3155-3156.

(27) Albert, I. D. L.; Marks, T. J.; Ratner, M. A. Remarkable NLO Response and Infrared Absorption in Simple Twisted Molecular π-Chromophores. *J. Am. Chem. Soc* **1998**, *120*, 11174-11181.

(28) Albert, I. D. L.; Marks, T. J.; Ratner, M. A. Conformationally-Induced Geometric Electron Localization. Interrupted Conjugation, Very Large Hyperpolarizabilities, and Sizale Infrared Absorption in Simple Twisted Molecular Chromophores. *J. Am. Chem. Soc.* **1997**, *119*, 3155-3156.

(29) Brown, E. C.; Ratner, M. A.; Marks, T. J. Nonlinear Response Properties of Ultralarge Hyperpolarizability Twisted Pi-System Donor-Accpetor Chromophores. *J. Phys. Chem.* **2007**, *112*, 44-50.

(30) Kang, H.; Facchetti, A.; Jiang, H.; Cariati, E.; Righetto, S.; Ugo, R.; Zuccaccia, C.; Macchioni, A.; Stern, C. L.; Marks, T. J. Ultra-large Hyperpolarizability Twisted π-electron System Electro-Optic Chromophores. *J. Am. Chem. Soc.* **2007**, *129*, 3267-3286.

(31) Kang, H.; Facchetti, A.; Stern, C. L.; Rheingold, W. S.; Marks, T. J. Efficient Synthesis and Structural Characteristics of Zwitterionic Twisted π-electron System Biaryls. *Org. Lett.* **2005**, *7*, 3721.

(32) Lou, A. J.-T.; Righetto, S.; Barger, C.; Zuccaccia, C.; Cariati, E.; Macchioni, A.; Marks, T. J. Unprecedented Large Hyperpolarizability of Twisted Chromophores in Polar Media. *J. Am. Chem. Soc., submitted* **2018**.

(33) Shi, Y.; Frattarelli, D.; Watanabe, N.; Facchetti, A.; Cariati, E.; Righetto, S.; Tordin, E.; Zuccaccia, C.; Macchioni, A.; Wegener, S. L.; Stern, C. L.; Ratner, M. A.; Marks, T. J. Ultra-High-Response, Multiply Twisted Electro-optic Chromophores: Influence of π-System

Elongation and Interplanar Torsion on Hyperpolarizability. *J. Am. Chem. Soc.* **2015**, *137*, 12521-12538.

(34) Shi, Y.; Lou, A. J.-T.; He, G. S.; Baev, A.; Swihart, M. T.; Prasad, P. N.; Marks, T. J. Cooperative Coupling of Cyanine and Tictoid Twisted π-Systems to Amplify Organic Chromophore Cubic Nonlinearities. *J. Am. Chem. Soc.* **2015**, *137*, 4622-4625.

(35) Teran, N. B.; He, G. S.; Baev, A.; Shi, Y.; Swihart, M. T.; Prasad, P. N.; Marks, T. J.; Reynolds, J. R. Twisted Thiophene-Based Chromophores with Enhanced Intramolecular Charge Transfer for Cooperative Amplification of Third-Order Optical Nonlinearity. *J. Am. Chem. Soc.* **2016**, *138*, 6975-6984.

(36) Wang, Y.; Frattarelli, D. L.; Facchetti, A.; Cariati, E.; Tordin, E.; Ugo, R.; Zuccaccia, C.; Macchioni, A.; Wegener, S. L.; Stern, C. L.; Ratner, M. A.; Marks, T. J. Twisted π-Electron System Electrooptic Chromophores. Structural and Electronic Consequences of Relaxing Twist-Inducing Nonbonded Repulsions. *J. Phys. Chem. C* **2008**, *112*, 8005-8015.

(37) Bishop, D. M.; Champagne, B. t.; Kirtman, B. Relationship between static vibrational and electronic hyperpolarizabilities of π-conjugated push–pull molecules within the two-state valence-bond charge-transfer model. *The Journal of chemical physics* **1998**, *109*, 9987.

(38) Grisanti, L.; D'Avino, G.; Painelli, A.; Guasch, J.; Ratera, I.; Veciana, J. Essential State Models for Solvatochromism in Donor-Acceptor Molecules: The Role of the Bridge. *J. Phys. Chem. B* **2009**, *113*, 4718-4725.

(39) Spangler, C. W. Recent Development in the Design of Organic Materials for Optical Power Limiting. *J. Mater. Chem.* **1999**, *9*, 2013-2020.

(40) He, G. S.; Autschbach, J.; Baev, A.; Samoc, M.; Fratarelli, D. L.; Watanabe, N.; Facchetti, A.; Agren, H.; Marks, T. J.; Prasad, P. N. Twisted π-System Chromophores: Novel Pathway to All-Optical Switching. *J. Am. Chem. Soc.* **2011**, *133*, 6675-6680.

(41) Gieseking, R. L.; Mukhopadhyay, S.; Risko, C.; Marder, S. R.; Bredas, J. L. 25th Anniversary Article: Design of Polymethine Dyes for All-Optical Switching Applications: Guidance from Theoretical and Computational Studies. *Adv. Mater.* **2014**, *26*, 68-83.

(42) Fisher, A. A.; Dreyer, E. F. C.; Chakrabarty, A.; Rand, S. C. Optial Magnetization, Part II: Theory of Induced Optical Magnetism. *Opt. Express* **2016**, *24*, 26055.

(43) Fisher, A. A.; Dreyer, E. F. C.; Chakrabarty, A.; Rand, S. C. Optical Magnetization, Part I: Experiments on Radiant Optical Magnetization in Solids. *Opt. Express* **2016**, *24*, 26064.

(44) Fisher, W. M.; Rand, S. C. Dependence of Optically Induced Magnetism on Molecular Electronic Structure. *J. Lumin.* **2009**, *129*, 1407-1409.

(45) Oliveira, S. L.; Rand, S. C. Intense nonlinear magnetic dipole radiation at optical frequencies: molecular scattering in a dielectric liquid. *Phys Rev Lett* **2007**, *98*, 093901.

(46) Rand, S. C.; Fisher, W. M.; Oliveira, S. L. Optically-Induced Magnetism in Dielectric Media. *J. Opt. Soc. Am. B* **2008**, *25*, 1106-1117.

(47) S.-S. Sun; Dalton, L. R.: *Introduction to Organic Electronic and Optoelectronic Materials and Devices*; Taylor & Francis: New York, 2008.

(48) Cho, M. J.; Choi, D. H.; Sullivan, P. A.; Akelaitis, A. J. P.; Dalton, L. R. Recent Progress in Second-Order Nonlinear Optical Polymers and Dendrimers. *Prog. in Polym. Sci.* **2008**, *33*, 1013-1058.

(49) Kim, T.-D.; Luo, J.; Cheng, Y.-J.; Shi, Z.; Hau, S.; Jang, S.-H.; Zhou, X.-H.; Tian, Y.; Polishak, B.; Huang, S.; Ma, H.; Dalton, L.; Jen, A. K.-Y. Binary Chromophore Systems in

Nonlinear Optical Dendrimers and Polymers for Large Electrooptic Activities. *J. Phys. Chem. C* **2008**, *112*, 8091-9098.

(50) Cheng, Y.-J.; Luo, J.; Huang, S.; Zhou, X.; Shi, Z.; Kim, T.-D.; Bale, D. H.; Takahashi, S.; Yick, A.; Steier, W.; Jen, A. K.-Y. Donor-Acceptor Thiolated Polyenic Chromophores Exhibiting Large Optical Nonlinearity and Excellent Photostability. *Chem. Mater.* **2008**, *20*, 5047-5054.

(51) Meyers, F.; Marder, S. R.; Pierce, B. M.; Bredas, J. L. Electric Field Modulated Nonlinear Optical Properties of Donor Acceptor Polyenes: Sum-Over-States Investigation of the Relationship Between Molecular Polarizabiltiesi (a, b, and g) and Bond Length Alternation. *J. Am. Chem. Soc.* **1994**, *116*, 10703-10714.

(52) Marder, S. R.; Kippelen, B.; Jen, A. K. Y.; Peyghambarian, N. Design and Synthesis of Chromophores and Polymers for Electro-Optic and Photorefractive Applications. *Nature* **1997**, *388*, 845.

(53) Zhang, C.; Dalton, L.; Oh, M.-C.; Zhang, H.; Steier, W. Low Vπ Electrooptic Modulators from CLD-1: Chromophore Design and Synthesis, Material Processing, and Characterization. *Chem. Mater.* **2001**, *13*, 3043-3050.

(54) Galvan-Gonzalez, A.; Belfield, K. D.; Stegeman, G. I.; Canva, M.; Marder, S. R.; Staub, K.; Levina, G.; Twieg, R. J. Photodegradation of Selected π-conjugated Electro-Optic Chromophores. *J. Appl. Phys.* **2003**, *94*, 756-763.

(55) Argouarch, G.; Veillard, R.; Roisnel, T.; Amar, A.; Boucekkine, A.; Singh, A.; Ledoux, I.; Paul, F. Donor-Substituted Triaryl-1,3,5-triazinanes-2,4,6-triones: Octupolar NLO-phores with a Remarkable Transparency–Nonlinearity Trade-off. *New J. Chem.* **2011**, *35*, 2409.

(56) Kang, H.; Zhu, P.; Yang, Y.; Facchetti, A.; Marks, T. J. Self-Assembled Electrooptic Thin Films with Remarkably Blue-Shifted Optical Absorption Based on an X-Shaped Chromophore. *J. Am. Chem. Soc.* **2004**, *126*, 15974-15975.

(57) Leclercq, A.; Zojer, E.; Jang, S. H.; Barlow, S.; Geskin, V.; Jen, A. K.; Marder, S. R.; Bredas, J. L. Quantum-Chemical Investigation of Second-order Nonlinear Optical Chromophores: Comparison of Strong Nitrile-Based Acceptor End Groups and Role of Auxiliary Donors and Acceptors. *J. Chem. Phys.* **2006**, *124*, 044510.

(58) Tabor, C. E.; Dalton, L. R.; Kajzar, F.; Kaino, T.; Koike, Y. Theory-Guided Nano-Engineering of Organic Electro-Optic Materials for Hybrid Silicon Photonic, Plasmonic, and Metamaterial Devices. *Proc. SPIE* **2013**, *8622*, 86220J.

(59) Liao, Y.; Anderson, C. A.; Sullivan, P.; Akelaitis, A. J. P.; Robinson, B. H.; Dalton, L. Electro-Optical Properties of Polymers Containing Alternating Nonlinear Optical Chromophores and Bulky Spacers. *Chem. Mater.* **2006**, *18*, 1062-1067.

(60) Bale, D. H.; Eichinger, B. E.; Liang, W.; Li, X.; Dalton, L. R.; Robinson, B. H.; Reid, P. J. Dielectric Dependence of the First Molecular Hyperpolarizability for Electro-optic Chromophores. *J. Phys. Chem. B* **2011**, *115*, 3505-3513.

(61) Chen, B. C.; von Philipsborn, W.; Nagarajan, K. 15N-NMR Spectra of Azoles with Two Heteroatoms. *Helv. Chim. Acta* **1983**, *66*, 1537-1555.

(62) Marelius, D. C.; Moore, C. E.; L., A.; Rheingold, A. L.; Grotjahn, D. B. Reactivity Studies of Pincer Bis-protic N-heterocyclic Carbene Complexes of Platinum and Palladium Under Basic Conditions. *Beilstein J. Org. Chem.* **2016**, *12*, 1334-1339.

(63) Nieto, C. I.; Cabildo, P.; García, M. A.; Claramunt, R. M.; Alkorta, I.; Elguero, J. An Experimental and Theoretical NMR Study of NH-Benzimidazoles in Solution and in the Solid State: Proton Transfer and Tautomerism. *Beilstein J. Org. Chem.* **2014**, *10*, 1620-1629.

(64) Witanowski, M.; Stefaniak, L.; Webb, G. A.: *Nitrogen NMR Spectroscopy. In Annual Reports on NMR Spectroscopy*; Acedemic Press: London, 1993; Vol. 25.

(65) Mason, J.: *Nitrogen NMR. In Encyclopedia of Nuclear Magnetic Resonance*; John Wiley: London, 1996. pp. 3222.

(66) Facelli, J. C.: *Shielding Calculations: Perturbation Methods. In Encyclopedia of Nuclear Magnetic Resonance*; John Wiley: London, 1996.

(67) Ramsey, N. F. The Internal Diamagnetic Field Correction in Measurements of the Proton Magnetic Moment. *Phys. Rev.* **1950**, *77*, 567.

(68) Ramsey, N. F. Magnetic Shielding of Nuclei in Molecules. *Phys. Rev.* **1950**, *78*, 699.

(69) Frohlich, R.; Musso, H. Notiz uber die Kristallstruktur des Bimesityls. *Chem. Ber.* **1985**, *118*, 4649-4651.

(70) Allen, F. H.; Watson, D. G.; Brammer, L.; Orpen, A. G.; Taylor, R.: Typical Interatomic Distances: Organic Compounds. In *International Tables for Crystallography*, 2006; pp 790-811.

(71) Linde, D. R. A Survey of Carbon-Carbon Bond Lengths. *Tetrahedron* **1962**, *17*, 125-134.

(72) Flandrois, P.; Chasseau, D. Longueurs de Liaison et Transfert de Charge dans les Sels du Tetracyanoquinodimethane (TCNQ). *Acta Cryst.* **1977**, *B33*, 2744-2750.

(73) Zuccaccia, C.; Bellachioma, G.; Cardaci, G.; Macchioni, A. Solution Structure Investigation of Ru(II) Complex Ion Pairs: Quantitative NOE Measurements and Determination of Average Interionic Distances. *J. Am. Chem. Soc.* **2001**, *123*, 11020-11028.

(74) Macchioni, A.; Magistrato, A.; Orabona, I.; Ruffo, F.; Rothlisberger, U.; Zuccaccia, C. Direct Observation of an Equilibrium Between Two Anion-Cation Orientations in Olefin Pt(II) Complex Ion Pairs by HOESY NMR Spectroscopy. *New J. Chem.* **2003**, *27*, 455-458.

(75) Neuhaus, D.; Williamson, M.: *The Nuclear Overhauser Effect in Strucutral and Conformational Analysis*; VCH Publishers: New York, 1989.

(76) Binev, Y. I.; Georgieva, M. K.; Novkova, S. I. The Conversion of Phenylpropanedinitrile (Phenylmalononitrile) into the Carbanion, Followed by IR Spectra, Ab Initio and DFT Force Field Calculations. *Spectrochim. Acta A* **2003**, *59*, 3041-3052.

(77) McRae, E. G. Theory of Solvent Effects on Molecular Electronic Spectra. Frequency Shifts. *J. Phys. Chem.* **1957**, *61*, 562.

(78) Grabowski, Z. R.; Rotkiewicz, K.; Rettig, W. Structural Changes Accompanying Intramolecular Electron Transfer: Focus on Twisted Intramolecular Charge-Transfer States and Structures. *Chem. Rev.* **2003**, *103*, 3899.

(79) Manohara, S. R.; Kumar, V. U.; Shivakumaraiah; Gerward, L. Estimation of Ground and Excited-State Dipole Moments of 1,2-Diazines by Solvatochromic Method and Quantum-Chemical Calculation. *Mol. Liq.* **2013**, *181*, 97.

(80) Sasaki, S.; Drummen, G. P. C.; Konishi, G.-i. Recent Advanecs in Twisted Intramolecuar Charge Transfer (TICT) Fluorescence and Related Phenomena in Materials Chemisty. *J. Mater. Chem. C* **2016**, *4*, 2731-2743.

(81) Kanis, D. R.; Lacroix, P. G.; Ratner, M. A.; Marks, T. J. Electronic Structure and Quadratic Hyperpolarizabilities in Organo-Metal Chromophores Having Weakly Coupled π-Networks. Unusual Mechanisms for Second-Order Response. *J. Am. Chem. Soc.* **1994**, *116*, 10089-10102.

(82) Isborn, C. M.; Davidson, E. R.; Robinson, B. H. Ab Initio Diradical/Zwitterionic Polarizabilities and Hyperpolarizabilities in Twisted Double Bonds. *J. Phys. Chem. A* **2006**, *110*, 7189-7196.

(83) Abbotto, A.; Beverina, L.; Bradamante, S.; Facchetti, A.; Klein, C.; Pagani, G. A.; Redi-Abshiro, M.; Wortmann, R. A Distinctive Example of the Cooperative Interplay of Structure and Environment in Tuning of Intramolecular Charge Transfer in Second-Order Nonlinear Optical Chromophores. *Chem. Eur. J.* **2003**, *9*, 1991-2007.

(84) Chandra Ray, P. Remarkable Solvent Effects on First Hyperpolarizabilities of Zwitterionic Merocyanine Dyes: Ab Initio TD-DFT/PCM Approach. *Chem. Phys. Lett.* **2004**, *395*, 269-273.

(85) Hammond, S. R.; Sinness, J.; Dubbury, S.; Firestone, K. A.; Benedict, J. B.; Wawrzak, Z.; Clot, O.; Reid, P. J.; Dalton, L. R. Molecular Engineering of Nanoscale Order in Organic Electro-Optic Glasses. *J. Mater. Chem.* **2012**, *22*, 6752.

(86) Brown, E. C.; Marks, T. J.; Ratner, M. A. Nonlinear Response Properties of Ultralarge Hyperpolarizability Twisted π-System Donor-Acceptor Chromophores. Dramatic Environmental Effects on Response. *J. Phys. Chem. B* **2008**, *112*, 44-50.

(87) Beniwal, V.; Shukla, S. K.; Kumar, A. Deviation of Polarity from Linearity in Liquid Mixtures Containing an Ionic Liquid. *Phys. Chem. Chem. Phys.* **2015**, *17*, 31613-31607.

(88) Mellein, B. R.; Aki, S. N. V. K.; Landewski, R. L.; Brennecke, J. F. Solvatochromic Studies of Ionic Liquid/Organic Mixtures. *J. Phys. Chem. B* **2007**, *111*, 131-138.

(89) Sarkar, A.; Pandey, S. Solvatochromic Absorbance Probe Behavior and Preferential Solvation in Aqueous 1-Butyl-3-methylimidzaolium Tetrafluoroborate. *J. Chem. Eng. Data* **2006**, *51*, 2051-2055.

(90) Li, Z. a.; Kim, H.; Chi, S.-H.; Hales, J. M.; Jang, S.-H.; Perry, J. W.; Jen, A. K. Y. Effects of Counterions with Multiple Charges on the Linear and Nonlinear Optical Properties of Polymethine Salts. *Chem. Mater.* **2016**, *28*, 3115-3121.

(91) Machado, C.; Nascimento, M. d. G.; Rezende, M. C.; Beezer, A. Calorimetric Evidence of Aggregation of the ET(30) Dye in Alcoholic Solutions. *Thermochem. Acta* **1999**, *328*, 155-159.

(92) Harrod, B. W.; Pienta, N. J. Solvent Polarity Scales. 1. Determination of the ET and π* Values for Phosphonium and Ammonium Melts. *J. Phys. Org. Chem.* **1990**, *3*, 534-544.

(93) Reichardt, C.; Acharin-Fard, S.; Schafer, G. The Halochromism of Pyridinium N-Phenoxide Betaine Dyes in Acetonitrile Solution. *Chem. Ber.* **1993**, *126*, 143-147.

(94) Del Sesto, R. E.; Corley, C.; Robertson, A.; Wilkes, J. S. Tetraalkylphosphonium-Based Ionic Liquids. *J. Organomet. Chem.* **2005**, *690*, 2536-2542.

(95) Turner, D. R.; MacDonald, R.; Teng Lee, W.; Batten, S. R. Ammonium Salts of Carbamoyldicyanomethanide, $C(CN)_2(CONH_2)^-$: Effects of Hydrogen-Bonding Cations on Anionic Networks. *Cryst. Eng. Comm.* **2009**, *11*, 298-305.

(96) Yi, C.; Blum, C.; Liu, S.-X.; Ran, Y.-F.; Frei, G.; Neels, A.; Stoeckli-Evans, H.; Calzaferri, G.; Leutwyler, S.; D'ecurtis, S. A Layered Red-Emitting Chromophore Organic Salt. *Cryst. Growth Des.* **2008**, *8*, 3004-3009.

(97) Adamova, G.; Gardas, R. L.; Nieuwenhuyzen, M.; Puga, A. V.; Rebelo, L. P.; Robertson, A. J.; Seddon, K. R. Alkyltributylphosphonium Chloride Ionic Liquids: Synthesis, Physicochemical Properties and Crystal Structure. *Dalton Trans.* **2012**, *41*, 8316-8332.

(98) Zhuo, J.-B.; Zhu, X.-X.; Lin, C.-X.; Bai, S.; Xie, L.-L.; Yuan, Y.-F. Design, Synthesis and Anion Recognition of Ferrocene-Based Benzimidazolium Receptors. *J. Organomet. Chem.* **2014**, *770*, 85-93.

(99) Wright, A. G.; Weissbach, T.; Holdcroft, S. Poly(phenylene) and m-Terphenyl as Powerful Protecting Groups for the Preparation of Stable Organic Hydroxides. *Angew. Chem. Int. Ed.* **2016**, *55*, 4818-4821.

(100) Machado, C.; Nascimento, M. d. G.; Rezende, M. C. Solvato- and Halo-chromic Behaviour of Some 4-[(N-Methylpyridiniumyl)methylidineamino]phenolate Dyes. *J. Chem. Soc. Perkin Trans.* **1994**, *2*, 2539-2544.

(101) Machado, V. G.; Stock, R. I.; Reichardt, C. Pyridinium N-phenolate Betaine Dyes. *Chem. Rev.* **2014**, *114*, 10429-10475.

(102) Kumar, R.; Fredrickson, G. H. Theory of Polyzwitterion Conformations. *J. Chem. Phys.* **2009**, *131*.

(103) Mary, P.; Bendajacq, D.; Labeau, M.-P.; Dupuis, P. Reconciling Low- and High-Salt Solution Behavior of Sulfobetaine Polyzwitterions. *J. Phys. Chem. B* **2007**, *111*, 7767-7777.

(104) Said, A. A.; Sheik-Bahaie, D. J.; Hagan, D. J.; Wei, T. H.; Wang, J.; Young, J.; Van Stryland, E. W. Determination of Bound-Electronic and Free-Carrier Nonlinearities in ZnSe, GaAs, CdTe, and ZnTe. *J. Opt. Soc. Am. B* **1992**, *9*, 405-414.

(105) Said, A. A.; Wamsley, C.; Hagan, D. J.; Van Stryland, E. W.; Reinhardt, B. A.; Roderer, P.; Dillard, A. G. Third- and Fifth-Order Optical Nonlinearities in Organic Materials. *Chem. Phys. Lett.* **1994**, *228*, 646-650.

(106) Wang, C.; Fan, C.; Yuan, C.; Yang, G.; Li, X.; Ju, C.; Feng, Y.; Xu, J. Third- and High-Order Nonlinear Optical Properties of an Intramolecular Charge-Transfer Compound. *RSC Adv.* **2017**, *7*, 4825-4829.

(107) Zhan, C.; Zhang, D.; Zhu, D.; Wang, D.; Li, Y.; Li, D.; Lu, Z.; Zhao, L.; Nie, Y. Third- and Fifth-Order Optical Nonlinearities in a New Stilbazolium Derivative. *J. Opt. Soc. Am. B* **2002**, *19*, 369-375.

(108) Nozaki, K.; Tanabe, T.; Shinya, A.; Matsuo, S.; Sato, T.; Taniyama, H.; Notomi, M. Sub-Femtojoule All-Optical Switching Using a Photonic-Crystal Nanocavity. *Nat. Photonics* **2010**, *4*, 477-483.

(109) Bredas, J. L.; Adant, C.; Tackx, P.; Persoons, A.; Pierce, B. M. Third-Order Nonlinear Optical Response in Organic Materials: Theoretical and Experimental Aspects. *Chem. Rev.* **1994**, *94*, 243-278.

(110) Gubler, U.; Bosshard, C. Molecular Design for Third-Order Nonlinear Optics. *Adv. Polym. Sci.* **2002**, *158*, 123-187.

(111) Acioli, L. H.; Gomes, A. S. L.; Leite, J. R. R. Measurement of High-Order Optical Nonlinear Susceptibilities in Semiconductor-Doped Glasses. *Appl. Phys. Lett.* **1988**, *53*, 1788-1790.

(112) Pawlicki, M.; Collins, H. A.; Denning, R. G.; Anderson, H. L. Two-Photon Absorption and the Design of Two-Photon Dyes. *Angew. Chem. Int. Ed.* **2009**, *48*, 3244-3266.

(113) Zhan, C.; Xu, W.; Zhang, D.; Li, D.; Lu, Z.; Nie, Y.; Zhu, D. Z-scan Investigation of Fifth-Order Optical Nonlinearity Induced by Saturable-Absorption from (TBA)2Ni(dmit)2: Application for Optical Limiting. *J. Mater. Chem.* **2002**, *12*, 2945-2948.

(114) Tykwinski, R. R.; Gubler, U.; Martin, R.; Diederich, F.; Bosshard, C.; Gunter, P. Structure-Property Relationships in Third-Order Nonlinear Optical Chromophores. *J. Phys. Chem. B* **1998**, *102*.

(115) Greve, D.; Schougaard, S. B.; Geisler, T.; Petersen, J. C.; Bjornholm, T. Large Third-Order Nonlinear Optical Response from Molecuels with Effective Multidirectional Charge-Transfer Transitions: New Design of Third-Order Nonlinear Chromophores. *Adv. Mater.* **1997**, *9*, 1113-1116.

(116) Concilio, S.; Biaggio, I.; Gunter, P.; Piotto, S. P.; Edelmann, M. J.; Raimundo, J.-M.; Deidrich, F. Third-Order Nonlinear Optical Properties of In-backbone Substituted Oligo(triacetylene) Chromophores. *J. Opt. Soc. Am. B* **2003**, *20*, 1656-1660.

(117) Tabor, C. E.; Kajzar, F.; Kaino, T.; Koike, Y.; Hu, H.; Ensley, T. R.; Reichert, M.; Ferdinandus, M. R.; Peceli, D.; Przhonska, O. V.; Marder, S. R.; Jen, A. K. Y.; Hales, J. M.; Perry, J. W.; Hagan, D. J.; Van Stryland, E. W. Optimization of the Electronic Third-Order Nonlinearity of Cyanine-Like Molecules for All Optical Switching. *Proc. SPIE* **2014**, *8983*, 898303.

(118) Barlow, S.; Brédas, J.-L.; Getmanenko, Y. A.; Gieseking, R. L.; Hales, J. M.; Kim, H.; Marder, S. R.; Perry, J. W.; Risko, C.; Zhang, Y. Polymethine Materials with Solid-State Third-Order Optical Susceptibilities Suitable for All-Optical Signal-Processing Applications. *Mater. Horiz.* **2014**, *1*, 577-581.

(119) Matichak, J. D.; Hales, J. M.; Barlow, S.; Perry, J. W.; Marder, S. R. Dioxaborine- and Indole-Terminated Polymethines: Effects of Bridge Substitution on Absorption Spectra and Third-Order Polarizabilities. *J. Phys. Chem. A* **2011**, *115*, 2160-2168.

(120) Sheik-Bahae, M.; Said, A. A.; Wei, T. H.; Hagan, D. J.; Van Stryland, E. W. Sensetive Measurement of Optical Nonlinearities Using a Single Beam. *IEEE J. Quantum Electron.* **1990**, *26*, 760-769.

(121) Ferdinandus, M. R.; Reichert, M.; Ensley, T. R.; Hu, H.; Fishman, D. A.; Webster, S.; Hagan, D. J.; Van Stryland, E. W. Dual-Arm Z-scan Technique to Extract Dilute Solute Nonlinearities from Solution Measurements. *Opt. Mater. Express* **2012**, *2*, 1776.

(122) Baerends, E. J. e. a. *Amsterdam Density Functional, SCM*; Theoretical Chemistry, Vrije Universiteit: Amsterdam, The Netherlands.

(123) Shao, Y. e. a. Advances in Molecular Quantum Chemistry Contained in the Q-Chem 4 Program Package. *Mol. Phys.* **2015**, *113*, 184-215.

(124) Cai, Z.-L.; Sendt, K.; Reimers, J. R. Failure of Density-Functional Theory and Time-Dependent Density-Functional Theory for Large Extended π Systems. *J. Chem. Phys.* **2002**, *117*, 5543-5549.

(125) Furche, F.; Rappoport, D.: Density Functional Methods for Excited States: Equilibrium Structure and Electronic Spectra. In *Computational Photochemstry*; Olivucci, M., Ed.; Elsevier: Amsterdam, 2005; Vol. 16; pp 93-128.

(126) Maitra, N. T. Perspective: Fundamental Aspects of Time-Dependent Density Functional Theory. *J. Chem. Phys.* **2016**, *144*, 220901.

(127) Tozer, D. J.; Amos, R. D.; Handy, N. C.; Roos, B. O.; Serrano-Andres, L. Does Density Functional Theory Contribute to the Understanding of Excited States of Unsaturated Organic Compounds? *Mol. Phys.* **1999**, *97*, 859-868.

(128) Binev, Y. I.; Georgieva, M. K.; Novkova, S. I. The Conversion of Phenylpropanedinitrile (Phenylmalononitrile) into the Carbanion, Followed by IR Spectra, Ab Initio and DFT Force Field Calculations. *Spectrochim. Acta.* **2003**, *59A*, 3041.

(129) Tabor, C. E.; Kajzar, F.; Kaino, T.; Koike, Y.; Wicks, G.; Rebane, A.; Drobizhev, M.: Two-Photon Solvatochromism of 4-dimethylamino-4'-nitrostilbene (DANS). In *Org. Photonics Mater. and Devices XVI*, 2014.

(130) Alam, M. M.; Chattopadhyaya, M.; Chakrabarti, S. On the Origin of Large Two-Photon Activity of DANS Molecule. *J. Phys. Chem. A* **2012**, *116*, 11034-11040.

(131) Krawczyk, P. DFT Study of Linear and Nonlinear Optical Properties of Donor-Acceptor Substituted Stilbenes, Azobenzenes and Benzilideneanilines. *J. Mol. Model.* **2010**, *16*, 659-668.

(132) Li, F.; Song, Y.; Yang, K.; Liu, S.; Li, C. Measurement of the C60 Molecular Polarizability of the Excited Singlet State Using Z-Scan. *Opt. Commun.* **1998**, *145*, 53-56.

(133) Grabowski, Z. R.; Rotkiewicz, K.; Rettig, W. Structural Changes Accompanying Intramolecular Electron Transfer: Focus on Twisted Intramolecular Charge-Transfer States and Structures. *Chem. Rev.* **2003**, *103*, 3899-4031.

(134) Maus, M.; Rettig, W. The Influence of Conformation and Energy Gaps on Optical Transition Moments in Donor-Acceptor Biphenyls. *Chem. Phys.* **2000**, *261*, 323-337.

(135) Kajzar, F.; Lee, K.-S.; Jen, A. K. Polymeric Materials and their Orientation Technique for Second-Order Nonlinear Optics. *Adv. Polym. Sci.* **2003**, *161*, 1-80.

(136) Shen, Y. R. Surface Properties Probed by Second-Harmonic and Sum-Frequency Generation. *Nature* **1989**, *337*, 519-525.

(137) Dini, D.; Calvete, M. J.; Hanack, M. Nonlinear Optical Materials for the Smart Filtering of Optical Radiation. *Chem. Rev.* **2016**, *116*, 13043-13233.

(138) Chai, Z.; Hu, X.; Wang, F.; Niu, X.; Xie, J.; Gong, Q. Ultrafast All-Optical Switching. *Adv. Opt. Mater.* **2017**, 1600665.

(139) Grigorenko, A. N.; Geim, A. K.; Gleeson, H. F.; Zhang, Y.; Firsov, A. A.; Khrushchev, I. Y.; Petrovic, J. Nanofabricated Media with Negative Permeability at Visible Frequencies. *Nature* **2005**, *438*, 335-338.

(140) Hoffman, A. J.; Alekseyev, L.; Howard, S. S.; Franz, K. J.; Wasserman, D.; Podolskiy, V. A.; Narimanov, E. E.; Sivco, D. L.; Gmachl, C. Negative Refraction in Semiconductor Metamaterials. *Nat. Mater.* **2007**, *6*, 946-950.

(141) Smith, D. R.; Pendry, J. B.; Wiltshire, M. C. K. Metamaterials and Negative Refractive Index. *Science* **2004**, *305*, 788-792.

(142) Schurig, D.; Mock, J. J.; Justice, B. J.; Cummer, S. A.; Pendry, J. B.; Starr, A. F.; Smith, D. R. Metamaterial Electromagnetic Cloak at Microwave Frequencies. *Science* **2006**, *314*, 977-979.

(143) Shalaev, V. M. Optical Negative-Index Metamaterials. *Nat. Photonics* **2007**, *1*, 41-48.

(144) Pendry, J. B. Negative Refraction Makes a Perfect Lense. *Phys. Rev. Lett.* **2000**, *85*, 3966-3969.

(145) Shelby, R. A.; Smith, D. R.; Schultz, S. Experimental Verification of a Negative Index of Refraction. *Science* **2001**, *292*, 77-79.

(146) Monticone, F.; Alù, A. The Quest for Optical Magnetism: From Split-Ring Resonators to Plasmonic Nanoparticles and Nanoclusters. *J. Mater. Chem. C* **2014**, *2*, 9059-9072.

(147) Oliveria, S. L.; Rand, S. C. Intense Nonlinear Magnetic Dipole Radiation at Optical Frequencies: Molecular Scattering in a Dielectic Liquid. *Phys. Rev. Lett.* **2007**, *98*, 093901.

(148) Fisher, A. A.; Cloos, E. F.; Fisher, W. M.; Rand, S. C. Dynamic Symmetry-Breaking in a Simple Quantum Model of Magneto-Electric Rectification, Optical Magnetization, and Harmonic Generation. *Opt. Express* **2014**, *22*, 2910-2924.

(149) Hales, J. M.; Matichak, J. D.; Barlow, S.; Ohira, S.; Yesudas, K.; Bredas, J. L.; Perry, J. W.; Marder, S. R. Design of Polymethine Dyes with Large Third-Order Optical Nonlinearities and Loss Figures of Merit. *Science* **2010**, *327*, 1485-1487.

(150) Ensley, T. R.; Hu, H.; Reichert, M.; Ferdinandus, M. R.; Peceli, D.; Hales, J. M.; Perry, J. W.; Li, Z. a.; Jang, S.-H.; Jen, A. K. Y.; al, e. Quasi-Three-Level Model Applied to Measured Spectra of Nonlinear Absorption and Refraction in Organic Molecules. *J. Opt. Soc. Am. B* **2016**, *33*, 780-796.

(151) Li, Z. a.; Ensley, T. R.; Hu, H.; Zhang, Y.; Jang, S.-H.; Marder, S. R.; Hagan, D. J.; Van Stryland, E. W.; Jen, A. K. Y. Conjugated Polycyanines: A New Class of Materials with Large Third-Order Optical Nonlinearities. *Adv. Opt. Mater.* **2015**, *3*, 900-906.

(152) Michinobu, T.; May, J. C.; Lim, J. H.; Boudon, C.; Gisselbrecht, J. P.; Seiler, P.; Gross, M.; Biaggio, I.; Diederich, F. A New Class of Organic Donor-Acceptor Molecules with Large Third-Order Optical Nonlinearities. *Chem. Commun.* **2005**, 737-739.

(153) Terenziani, F.; Przhonska, O. V.; Webster, S.; Padilha, L.; Slominsky, Y.; Davydenko, I.; Gerasov, A.; Kovtun, Y.; Shandura, M.; Kachkovski, A.; al, e. Essential-State

Model for Polymethine Dyes: Symmetry Breaking and Optical Spectra. *J. Phys. Chem. Lett.* **2010**, *1*, 1800-1804.

(154) Boldrini, B.; Cavalli, E.; Painelli, A.; Terenziani, F. Polar Dyes in Solution: A Joint Experimental and Theoretical Study of Absorption and Emission Band Shapes. *J. Phys. Chem. A* **2002**, *106*, 6286-6294.

(155) Cho, M.; An, S.-Y.; Lee, H.; Ledoux, I.; Zyss, J. Nonlinear Optical Properties of Tetrahedral Donor–Acceptor Octupolar Molecules: Effective Five-State Model Approach. *J. Chem. Phys.* **2002**, *116*, 9165-9173.

(156) Cho, M.; Kim, H.-S.; Jeon, S.-J. An Elementary Description of Nonlinear Optical Properties of Octupolar Molecules: Four-State Model for Guanidinium-Type Molecules. *J. Chem. Phys.* **1998**, *108*, 7114-7120.

(157) Lee, Y.-K.; Jeon, S.-J.; Cho, M. Molecular Polarizability and First Hyperpoalrizabtility of Octupolar Molecules: Donor-Substituted Triphenylmethane Dyes. *J. Am. Chem. Soc.* **1998**, *120*, 10921-10927.

(158) Yang, M.; Champagne, B. Large Off-Diagonal Contribution to the Second-Order Nonlinearities of L-Shaped Molecules. *J. Phys. Chem. A* **2003**, *107*, 3942-3951.

(159) Balanis, C. A.: *Advanced Engineering Electromagnetics*; John Wiley & Sons, Inc:: New York, 1989.

(160) Fisher, A. A.; Cloos, E. F.; Fisher, W. M.; Rand, S. C. Dynamic Symmetry-Breaking in a Simple Quantum Model of Magneto-Electric Rectification, Optical Magnetization, and Harmonic Generation. *Opt. Express* **2014**, *22*, 789-793.

(161) Gorman, C.; Marder, S. R. Effect of Molecular Polarization on Bond-Length Alternation, Linear Polarizability, First and Second Hyperpolarizability in Donor-Acceptor Polyenes as a Function of Chain Length. *Chem. Mater.* **1995**, *7*, 215-220.

(162) Verbeist, T.; Clays, K.; Samyn, C.; Wolff, J.; Reinhoudt, D.; Persoons, A. Investigation of the Hyperpolarizability in Organic Molecules from Dipolar to Octopolar Systems. *J. Am. Chem. Soc.* **1994**, *116*, 9320-9323.

(163) Coe, B. J.; Fielden, J.; Foxon, S. P.; Helliwell, M.; Asselberghs, I.; Clays, K.; De Mey, K.; Brunschwig, B. S. Syntheses and Properties of Two-Dimensional, Dicationic Nonlinear Optical Chromophores Based on Pyrazinyl Cores. *J. Org. Chem.* **2010**, *75*, 8550-8563.

(164) Ramirez, M. A.; Cuadro, A. M.; Alvarez-Builla, J.; Castano, O.; Andres, J. L.; Mendicuti, F.; Clays, K.; Asselberghs, I.; Vaquero, J. J. Donor-(pi-Bridge)-azinium as D-pi-A+ One-Dimensional and D-pi-A(+)-pi-D Multidimensional V-Shaped Chromophores. *Org. Biomol. Chem.* **2012**, *10*, 1659-1669.

(165) Kang, H.; Evmenenko, G.; Dutta, P.; Clays, K.; Song, K.; Marks, T. J. X-Shaped Electro-optic Chromophore with Remarkably Blue-Shifted Optical Absorption. Synthesis, Characterization, Linear/Nonlinear Optical Properties, Self-Assembly, and Thin Film Microstructural Characteristics. *J. Am. Chem. Soc.* **2006**, *128*, 6194-6205.

(166) Oliva, M. M.; Casado, J.; Hennrich, G.; Navarrete, J. T. L. Octopolar Chromophores Based on Donor- and Acceptor-Substituted 1,3,5-Tris(phenylethynyl)benzenes: Impact of Meta-Conjugation on the Molecular and Electronic Structure by Means of Spectroscopy and Theory. *J. Phys. Chem. B.* **2006**, *110*, 19198-19206.

(167) Traber, B.; Oeser, T.; Gleiter, R.; Goebel, M.; Wortmann, R. d. Donor-Substituted Heptaazaphenalene as a Nonlinear Optically Active Molecule with Multiple Charge-Transfer Transitions. *Eur. J. Org. Chem.* **2004**, *2004*, 4387-4390.

(168) Wortmann, R.; Lebus-Henn, S.; Reis, H.; Papadopoulos, M. G. Off-Diagonal Second-Order Polarizability of N,N′-dihexyl-1,3-diamino-4,6-dinitrobenzene. *J. Mol. Struct.: THEOCHEM* **2003**, *633*, 217-226.

(169) Dirk, C. W.; Cheng, L.-T.; Kuzyk, M. G. A Simplified Three-Level Model Describing the Molecular Third-Order Nonlinear Optical Susceptibility. *Int. J. Quantum Chem.* **1992**, *43*, 27-36.

(170) Orr, B. J.; Ward, J. F. Perturbation Theory of the Non-linear Optical Polarization of an Isolated System. *Mol. Phys.* **1971**, *20*, 513-526.

(171) Metzger, R. M. Unimolecular Electrical Rectifiers. *Chem. Rev.* **2003**, *103*, 3803-3834.

(172) Terenziani, F.; Painelli, A.; Girlando, A.; Metzger, R. M. From Solution to Langmuir-Blodgett Films: Spectroscopic Study of a Zwitterionic Dye. *J. Phys. Chem. B* **2004**, *108*, 10743-10750.

(173) Kato, S.-i.; Beels, M. T. R.; La Porta, P.; Schweizer, W. B.; Boudon, C.; Gisselbrecht, J.-P.; Biaggio, I.; Diederich, F. Homoconjugated Push-Pull and Spiro Systems: Intramolecular Charge-Transfer Interactions and Third-Order Optical Nonlinearities. *Angew. Chem. Int. Ed.* **2010**, *49*, 6207-6211.

(174) Tykwinski, R. R.; Gubler, U.; Martin, R.; Deidrich, F.; Bosshard, C.; Gunter, P. Structure-Property Relationships in Third-Order Nonlinear Optical Chromophores. *J. Phys. Chem. B.* **1998**, *102*, 4451-4465.

(175) Gubler, U.; Spreiter, R.; Bosshard, C.; Günter, P.; Tykwinski, R. R.; Diederich, F. Two-Dimensionally Conjugated Molecules: The Importance of Low Molecular Symmetry for Large Third-Order Nonlinear Optical Effects. *Appl. Phys. Lett.* **1998**, *73*, 2396-2398.

(176) Bosshard, C.; Spreiter, R.; Gunter, P.; Tykwinski, R. R.; Schreiber, M.; Deidrich, F. Structure-Property Relationships in Nonlinear Optical Tetraethynylethenes. *Adv. Mater.* **1996**, *8*, 231-234.

(177) Kim, J. J.; Funabiki, K.; Muramatsu, H.; Shibata, K.; Kim, S. H.; Shiozaki, H.; Hartmann, H.; Matsui, M. Negative Solvatochromism of Azo Dyes Derived from (Dialkylamino)thiazole Dimers. *Chem. Commun.* **2000**, 753-754.

(178) Ishchenko, A. A.; Kulinich, A. V.; Bondarev, S. L.; Knyukshto, V. N. Electronic Structure and Fluorescent Properties of Malononitrile-Based Merocyanines with Positive and Negative Solvatochromism. *Opt. and Spec.* **2008**, *104*, 57-68.

(179) Meng, S.; Caprasecca, S.; Guido, C. A.; Jurinovich, S.; Mennucci, B. Negative Solvatochromism of Push-Pull Biphenyl Compounds: a Theoretical Study. *Theor. Chem. Acc.* **2015**, *134*.

(180) Kulinich, A. V.; Mikitenko, E. K.; Ishchenko, A. A. Scope of Negative Solvatochromism and Solvatofluorochromism of Merocyanines. *Phys. Chem. Chem. Phys.* **2016**, *18*, 3444-3453.

(181) Warde, U.; Sekar, N. NLOphoric Mono-Azo Dyes with Negative Solvatochromism and In-Built ESIPT Unit from Ethyl 1,3-dihydroxy-2-naphthoate: Estimation of Excited State Dipole Moment and pH Study. *Dyes and Pigments* **2017**, *137*, 384-394.

(182) Jacques, P.; Graff, B.; Diemer, V.; Ay, E.; Chaumeil, H.; Carre, C.; Malval, J.-P. Negative Solvatochromism of a Series of Pyridinium Phenolate Betaine Dyes with Increasing Steric Hindrance. *Chem. Phys. Lett.* **2012**, *5331*, 242-246.

(183) Alain, V.; Redoclia, S.; Blanchard-Desce, M.; Lebus, S.; Lukaszuk, K.; Wortmann, R.; Gubler, U.; Bosshard, C.; Gunter, P. Elongated Push-Pull Diphenylpolyenes for Nonlinear Optics: Molecular Engineering of Quadratic and Cubic Optical Nonlinearities via Tuning of Intramolecular Charge Transfer. *Chem. Phys.* **1999**, *245*, 51-71.

(184) Salman, S.; Brédas, J.-L.; Marder, S. R.; Coropceanu, V.; Barlow, S. Dipolar Ferrocene and Ruthenocene Second-Order Nonlinear Optical Chromophores: A Time-Dependent Density Functional Theory Investigation of Their Absorption Spectra. *Organometallics* **2013**, *32*, 6061-6068.

Chapter 1 Appendix.

S1.1 Materials and methods. All reagents were purchased from Sigma-Aldrich and used without further purification unless otherwise noted. Tetrahydrofuran (THF), dichloromethane (CH_2Cl_2), and toluene were dried by passing through a column of activated alumina under argon. The reagent 2,5-dibromo-1,3-dimethylbenzene was purchased from Combi-Blocks. 1H and 13C NMR spectra were recorded on Agilent DD MR-400 MHz, Varian Inova 500 MHz or Bruker Avance III 500 MHz spectrometers. ^{1}H,^{15}N HMBC experiments were carried out on a Bruker Avance III spectrometer, operating at 400.13 MHz and equipped with the Smartprobe, using the standard Bruker pulse program "hmbcgplpndqf". ^{15}N chemical shift is referenced to external nitromethane. Low resolution mass spectra were recorded on an Amazon SL LC-ESI mass spectrometer, elemental analysis was performed by Midwest Microlab, and optical spectra were recorded using an Agilent Cary 5000 spectrophotometer. Thermogravimetric analysis was performed with ramping at a rate of 10 °C/min.

General procedure for preparing benzimidazoles (1A-1C). A three-neck flask was fitted with a reflux condenser and a gas inlet. To the flask was added the desired bromo-benzaldehyde (1 eq) and phenylenediamine (1 eq.). 1,4-dioxane (3 mL/mmol aldehyde) was added and the solution was heated to 90 °C with continuous bubbling of air. After 24 h, the reaction is diluted into DCM and filtered to yield the desired benzimidazole.

1H-2-(4-bromobenzene)-benzimidazole (1A). Reaction of phenylenediamine (3.0 g, 27.8 mmol) and 4-bromobenzaldehyde (5.14 g, 27.8 mmol) in 50 mL 1,4-dioxane yields 2.23 g of the title compound as a yellow powder (29 % yield). ^{1}H NMR (500 MHz, d^{6}-dmso): δ 12.98 (s, 1H), 8.1 (d, J = 8.5 Hz, 2H), 7.76 (d, J = 8.5, 2H), 7.67 (d, J = 7.5 Hz, 1H), 7.53 (d, J = 7.5 Hz, 1H), 7.22 (m, 2H). MS (ESI) *m/z*: $[M+H]^+$ Calcd. for $C_{13}H_{10}N_2Br$ 273.00; Found 273.02; $[M-H]^-$ Calcd. for $C_{13}H_8N_2Br$ 270.99; Found 271.03.

1H-2-(4-bromo-2-methylbenzene)-benzimidazole (1B). Reaction of phenylenediamine (2.50 g, 23.1 mmol) and 4-bromo-2-methylbenzaldehyde (4.60 g, 23.1 mmol) in 60 mL 1,4-dioxane yields 2.60 g of the title compound as a tan powder (39 % yield). ^1H NMR (500 MHz, d^6-dmso): δ 12.68 (s, 1H), 7.69 (m, 2H), 7.64 (s, 1H), 7.58 (d, J = 8.5, 1H), 7.53 (d, J = 7.5, 1H), 7.22 (m, 2H), 2.62 (s, 3H). MS (ESI) *m/z*: $[M+H]^+$ Calcd. for $C_{14}H_{10}N_2Br$ 287.02; Found 287.00; $[M-H]^-$ Calcd. for $C_{14}H_{10}N_2Br$ 285.00; Found 284.93.

1H-2-(4-bromo-2,6-dimethylbenzene)-benzimidazole (1C). Reaction of phenylenediamine (520 mg, 4.8 mmol) and 4-bromo-2,6-dimethylbenzaldehyde (1.03 g, 4.8 mmol) in 30 mL 1,4-dioxane yields 830 mg of the title compound as a grey powder (42 % yield). ^1H NMR (500 MHz, d^6-dmso): δ 12.54 (s, 1H), 7.67 (d, J = 7.5, 1H), 7.50 (d, J = 7.5, 1H), 7.45 (s, 2H), 7.21 (m, 2H), 2.09 (s, 6H). MS (ESI) *m/z*: $[M+H]^+$ Calcd. for $C_{15}H_{14}N_2Br$ 301.03; Found 301.05; $[M-H]^-$ Calcd. for $C_{15}H_{14}N_2Br$ 299.02; Found 298.96.

General procedure for region-selective alkylation of benzimidazoles (2A-2C). To an oven dried flask was added **1A-1C**, KI and dry THF. KOtBu in THF was added slowly at room temperature, followed by 1-bromohexane. The reaction was sealed and heated at 60 °C under N_2 for 24 hours. Upon completion (as monitored by TLC Hex/EtOAc), the reaction was poured into DCM and washed with water and dried over Na_2SO_4. The crude was purified via silica gel plug, eluting with hexane followed by EtOAc/Hex.

1-hexyl-2-(4-bromobenzene)-benzimidazole (2A). Reaction of **1A** (2.0 g, 7.3 mmol), hexylbromide (12.1 g, 73.3 mmol), KOtBu (1.6 g, 14.6 mmol) and a catalytic amount of KI in 150 mL dry THF yields 2.27 g of the title compound as a reddish liquid (87 % yield). ^{1}H NMR (500 MHz, $CDCl_3$): δ 7.83 (m, 1H), 7.67 (d, J = 8.5, 2H), 7.60 (d, J = 8.5, 2H), 7.41 (m, 1H), 7.32 (m, 2H), 4.21 (t, J = 8, 2H), 1.81 (m, 2H), 1.23 (m, 6H), 0.85 (t, J = 7, 3H). MS (ESI) *m/z*: $[M+H]^+$ Calcd. for $C_{19}H_{22}N_2Br$ 357.10; Found 357.18.

1-hexyl-2-(4-bromo-2-methylbenzene)-benzimidazole (2B). Reaction of **1B** (2.0 g, 7.0 mmol), hexylbromide (5.75 g, 34.8 mmol), KOtBu (1.56 g, 13.9 mmol) and a catalytic amount of KI in 150 mL dry THF yields 2.11 g of the title compound as a reddish liquid (81 % yield). ^{1}H NMR (500 MHz, $CDCl_3$): δ 7.82 (d, J = 8, 1H), 7.53 (s, 1H), 7.46 (d, J =8.5, 1H), 7.42 (d, J = 8.5, 1H), 7.32 (m, 2H), 7.26 (m, 1H), 3.98 (t, J = 8, 2H), 2.23 (s, 3H), 1.67 (m, 2H), 1.15 (m, 6H), 0.82 (t, J = 7.5, 3H). MS (ESI) *m/z*: $[M+H]^+$ Calcd. for $C_{20}H_{24}N_2Br$ 371.11; Found 371.17.

1-hexyl-2-(4-bromo-2,6-dimethylbenzene)-benzimidazole (2C). Reaction of **1C** (800 mg, 2.7 mmol), hexylbromide (2.2 g, 13.3 mmol), KOtBu (600 mg, 5.3 mmol) and a catalytic amount of KI in 60 mL dry THF yields 895 mg of the title compound as a brown liquid (91 % yield). ^{1}H NMR (400 MHz, $CDCl_3$): δ 7.79 (m, 1H), 7.41 (m, 1H), 7.31 (m, 4H), 3.83 (t, J = 7.5, 2H), 2.05 (s, 6H), 1.59 (m, 2H), 1.18 (m, 6H), 0.82 (t, J = 7, 3H). MS (ESI) *m/z*: $[M+H]^+$ Calcd. for $C_{21}H_{26}N_2Br$ 385.13; Found 385.21.

General procedure for malononitrile coupling (3A-3C): An oven dried flask was charged with **2A-2C**, $Pd(PPh_3)_4$, NaOtBu, and degassed DME. A solution of malononitrile in degassed DME was then added via syringe at room temperature under N_2. The reaction flask was then sealed and heated to 75 °C for 12 h. The reaction mixture was diluted into water and precipitated by adjusting the pH to 6.5 with slow addition of 2M HCl. The resulting solid was isolated by filtration then purified by column chromatography on silica gel, eluting with 60% EtOAc in hexanes.

1-hexyl-2-(4-(dicyanomethyl)benzene)-benzimidazole (3A). Reaction of **2A** (1.78 g, 5.0 mmol), malononitrile (990 mg, 15.0 mmol), $Pd(PPh_3)_4$ (580 mg, 0.5 mmol), and NaOtBu (2.9 g, 30.0 mmol) in 45 mL DME yields 1.44 g of the title compound as a tan powder (82 % yield). ^1H NMR (400 MHz, d6-dmso): δ (ppm) 8.00 (m, 1H), 7.74 (m, 1H), 7.56 (d, J = 8.8, 2H), 7.55 (m, 2H), 6.97 (d, J= 8.8, 2H), 4.48 (t, J = 7.6, 2H), 2.50 (s, 6H), 1.82 (m, 2H), 1.20 (m, 6H), 0.81 (t, J = 6.8, 3H). MS (ESI) *m/z*: $[M+H]^+$ Calcd. for $C_{22}H_{23}N_4$ 343.19; Found 343.30; $[M-H]^-$ Calcd. for $C_{22}H_{21}N_4$ 341.18; Found 341.31.

1-hexyl-2-(4-(dicyanomethyl)-2-methylbenzene)-benzimidazole (3B). Reaction of **2B** (1.14 g, 3.07 mmol), malononitrile (607 mg, 9.21 mmol), $Pd(PPh_3)_4$ (350 mg, 0.3 mmol), and NaOtBu (1.77 g, 18.42) in 45 mL DME yields 830 mg of the title compound as a tan powder (76 % yield). ^1H NMR (500 MHz, d6-dmso): δ(ppm) 8.05 (d, J = 9, 1H), 7.80 (d, J = 9, 1H), 7.62 (m, 2H), 7.31 (d, J=8.5, 1H), 6.80 (s, 1H), 6.77 (m, 1H), 4.32 (t, J = 8, 2H), 2.16 (s, 3H), 1.70 (m, 2H), 1.10 (m, 6H), 0.76 (t, J = 7, 3H). MS (ESI) *m/z*: $[M+H]^+$ Calcd. for $C_{23}H_{25}N_4$ 357.21; Found 357.32; $[M-H]^-$ Calcd. for $C_{23}H_{23}N_4$ 355.19; Found 355.22.

1-hexyl-2-(4-(dicyanomethyl)-2,6-dimethylbenzene)-benzimidazole (3C). Reaction of **2C** (895 mg, 2.4 mmol), malononitrile (480 mg, 7.24 mmol), $Pd(PPh_3)_4$ (280 mg, 0.24 mmol), and NaOtBu (1.39 g, 14.46 mmol) in 36 mL DME yields 620 mg of the title compound as a tan powder (70 % yield). ^1H NMR (400 MHz, d6-dmso): δ(ppm) 8.07 (m, 1H), 7.83 (m, 1H), 7.64 (m, 2H), 6.65 (s, 2H), 4.21 (t, J = 9, 2H), 1.97 (s, 6H), 1.66 (m, 2H), 1.14 (m, 6H), 0.77 (t, J = 8.5, 3H). MS (ESI) *m/z*: $[M+H]^+$ Calcd. for $C_{24}H_{27}N_4$ 371.22; Found 371.28; $[M-H]^-$ Calcd. for $C_{24}H_{25}N_4$ 369.21; Found 369.19.

General procedure for alkylation and deprotonation (BXTMC-2). To a round bottom flask was added **3A-3C**, KOtBu, and acetone. The mixture was cooled to 0 °C prior to the dropwise addition of freshly prepared pentyl triflate in acetone. The reaction was stirred at 0 °C for 1 h. The solvent was then removed in vacuo, taken up in DCM and filtered. The supernatant was purified by column chromatography on silica gel using a gradient of EtOAC in DCM (0 – 20%).

1-hexyl-2-(4-(dicyanomethanide)benzene)-3-pentylbenzimidazole (B0TMC-2). Reaction of **3A** (600 mg, 1.74 mmol), pentyl triflate (426 mg, 1.92 mmol), KOtBu (194 mg, 1.74 mmol), in 15 mL acetone yields 310 mg of the title compound as a yellow powder (43 % yield). ^{1}H NMR (500 MHz, d^6-dmso): δ (ppm) 8.10 (m, 2H), 7.68 (m, 2H), 7.42 (d, J = 9, 2H), 6.96 (d, J = 9, 2H), 4.32 (t, J = 7.5, 4H), 1.69 (m, 4H), 1.15 (m, 10 H), 0.764 (m, 6H). ^{13}C{H} NMR (500 MHz, d^6-dmso): δ 151.85, 147.87, 131.49, 130.52, 126.71, 124.16, 118.41, 113.96, 107.52, 32.61, 30.85, 28.73, 28.51, 28.25, 25.77, 22.29, 21.87, 14.22, 14.08. MS (ESI) *m/z*: [M+H]$^+$ Calcd. for $C_{27}H_{33}N_4$ 413.27; Found 413.29. Anal. Calcd. For $C_{27}H_{32}N_4$: C, 78.60; H, 7.82; N, 13.58. Found: C, 78.97; H, 7.67; N, 13.36.

1-hexyl-2-(4-(dicyanomethanide)-2-methylbenzene)-3-pentylbenzimidazole (B1TMC-2). Reaction of **3B** (400 mg, 1.12 mmol), pentyl triflate (272 mg, 1.23 mmol), KOtBu (125 mg, 1.12 mmol), in 12 mL acetone yields 120 mg of the title compound as a yellow powder (25 % yield). ^{1}H NMR (500 MHz, d^6-dmso): δ (ppm) 8.13 (m, 2H), 7.71 (m, 2H), 7.30 (d, J = 8, 1H), 6.82 (s, 1H), 6.79 (d, J = 8, 1H), 4.36 (m, 2H), 4.11 (m, 2H), 2.00 (s, 3H), 1.66 (m, 4H), 1.14 (m, 10H), 0.77 (m, 6H). ^{13}C {H} NMR (500 MHz, d^6-dmso): δ 151.58, 147.76, 137.75, 131.46, 131.44, 130.74, 126.88, 124.52, 119.70, 116.46, 114.25, 107.47, 31.57, 30.88, 28.65, 28.43, 28.24, 25.77, 22.25, 21.89, 19.59, 14.21, 14.04. MS (ESI) *m/z*: [M+H]$^+$ Calcd. for $C_{28}H_{35}N_4$ 427.29; Found 427.2. Anal. Calcd. For $C_{28}H_{34}N_4$: C, 78.83; H, 8.03; N, 13.13. Found: C, 78.65; H, 7.81; N, 12.98.

1-hexyl-2-(4-(dicyanomethanide)-2,6-dimethylbenzene)-3-pentylbenzimidazole (B2TMC-2). Reaction of **3C** (400 mg, 1.08 mmol), pentyl triflate (263 mg, 1.2 mmol), KOtBu

(120 mg, 1.08 mmol), in 12 mL acetone yields 242 mg of the title compound as a yellow powder (% yield). ^{1}H NMR (400 MHz, d^6-dmso): δ (ppm) 8.15 (m, 2H), 7.73 (m, 2H), 6.68 (s, 2H), 4.21 (t, J = 8, 4H), 1.92 (s, 6H), 1.65 (m, 4H), 1.19 (m, 10H), 0.78 (m, 6H). ^{13}C {H} NMR (500 MHz, d^6-dmso): δ 151.07, 147.56, 137.91, 131.47. 127.13, 124.69, 117.92, 114.47, 107.35, 31.08, 30.92, 28.72, 28.50, 28.37, 25.91, 22.23, 21.93, 19.90, 14.23, 14.03. MS (ESI) *m/z*: $[M+H]^+$ Calcd. for $C_{29}H_{37}N_4$ 441.30; Found 441.35. Anal. Calcd. For $C_{29}H_{36}N_4$: C, 79.05; H, 8.24; N, 12.72. Found: C, 78.92; H, 8.24; N, 12.69.

S1.2 Calculation of intrinsic hyperpolarizability. The maximum theoretical hyperpolarizability, defined by Eq. S1.1, depends on the first excitation energy, E_{eg}, the number of electrons, N, and fundamental constants.[1]

$$\beta_{max} = \sqrt[4]{3}\left(\frac{e\hbar}{\sqrt{m}}\right)^3 \frac{N^{3/2}}{E_{01}^{7/2}} \qquad \textbf{(S1.1)}$$

In the case of conjugated π systems, it is convention to include two electrons for each double bond, and for **BXTMC-2** chromophores, two additional electrons for the anionic donor group and two for the nitrogen lone pair. The total number of electrons N = 18 for these systems. E_{eg} is taken as the onset of the low energy optical absorption in DCM.

Table S1.1. Calculation of intrinsic hyperpolarizability (β_{max}) from number of polarizable electrons (N), lowest transition energy (E_{01}) and EFISH derived beta (β_{obs})

	N	E_{01} (eV)	$\lvert\beta_{obs}\rvert$ (esu x 10^{-30})	β_{max} (esu x 10^{-30})	β_{int}
B0TMC-2	18	2.55	486	3370	0.14
B1TMC-2	18	2.62	499	3070	0.16
B2TMC-2	18	2.67	1056	2870	0.37
TMC-2	14	2.18	890	4010	0.20

---

[1] Kuzyk, M. G.; Singer, K. D.; Stegeman, G. I., Theory of Molecular Nonlinear Optics. *Adv. Opt. Photonics* **2013,** *5* (1), 4.

S1.3 Electric-field induced second harmonic generation (EFISH). EFISH measurements were carried out in CH_2Cl_2, dimethylformamide (DMF) and anhydrous $CHCl_3$ solutions of different concentrations at a non-resonant fundamental wavelength of 1907 nm using a Q-switched, modelocked Nd^{3+}:YAG laser (pulse durations of 15 ns (90 ns) at a 10 Hz repetition rate). The 1064 nm initial wavelength was shifted to 1907 nm by a Raman shifter with a high-pressure H_2 cell. The $\mu\beta_{vec}$ values reported (see Table S1.2) are the averages of more than 10 successive measurements performed on each sample.

Table S1.2. EFISH measurements in DCM solution

B0TMC-2		**B1TMC-2**		**B2TMC-2**	
Conc. (M)	$\mu\beta_{vec}$ ($x10^{-48}$ esu)	Conc. (M)	$\mu\beta_{vec}$ ($x10^{-48}$ esu)	Conc. (M)	$\mu\beta_{vec}$ ($x10^{-48}$ esu)
10^{-4}	-10300 ± 1030	10^{-4}	-8420 ± 1077	10^{-4}	-9660 ± 1540
5×10^{-5}	-8600 ± 3010	$5x10^{-5}$	-11730 ± 2672	$5x10^{-5}$	-19620 ± 2355
		10^{-5}	-13831 ± 9680	10^{-5}	-26000 ± 2600

Table S1.3. EFISH measurements in DMF solution

B0TMC-2		**B1TMC-2**		**B2TMC-2**	
Conc. (M)	$\mu\beta_{vec}$ ($x10^{-48}$ esu)	Conc. (M)	$\mu\beta_{vec}$ ($x10^{-48}$ esu)	Conc. (M)	$\mu\beta_{vec}$ ($x10^{-48}$ esu)
10^{-4}	-8400 ± 1300	10^{-4}	-12740 ± 1660	10^{-3}	-12000 ± 1200
				10^{-4}	-20370 ± 2037
				5×10^{-5}	-18670 ± 7624

S1.4. Nuclear Overhauser effect (NOE) NMR spectroscopy. B0TMC-2, **B1TMC-2** and **B2TMC-2** were dissolved in dry DMSO-d_6; the resulting solutions degassed via four freeze-pump-thaw cycles. NOE measurements as a function of temperature (298-358 K) were performed on a Bruker Avance III spectrometer operating at 400.13 MHz, equipped with the Smartprobe, using the 1D-GOESY pulse sequence developed by Keeler and co-workers,[2,3] under the initial rate approximation.[4]

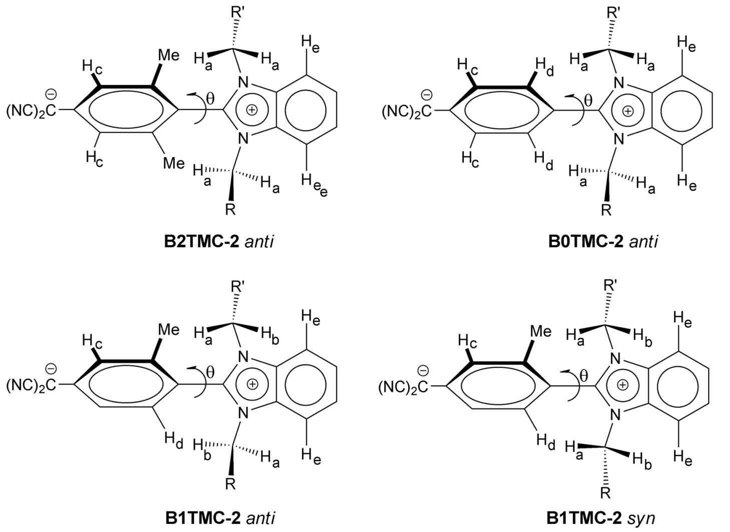

B2TMC-2 *anti* **B0TMC-2** *anti*

B1TMC-2 *anti* **B1TMC-2** *syn*

Scheme S1.1. Chemical structure and numbering scheme of *syn* and *anti* conformations for **B0TMC-2**, **B1TMC-2** and **B2TMC-2** chromophores.

---

[2] Stott, K.; Stonehouse, J.; Keeler, J.; Hwang, T. L.; Shaka, A. J., Excitation Sculpting in High-Resolution Nuclear Magnetic Resonance Spectroscopy: Application to Selective NOE Experiments. *J. Am. Chem. Soc.* **1995,** *117*, 4199.

[3] Stonehouse, J.; Adell, P.; Keeler, J.; Shaka, A. J., Ultrahigh Quality NOE Spectra. *J. Am. Chem. Soc.* **1994,** *116*, 6037-6038.

[4] The mixing time (τm) was set to 100 ms as a good compromise between initial rate approximation and a sufficient signal to noise ratio. Neuhaus, D.; Williamson M. *The Nuclear Overhauser Effect in Structural and Conformational Analysis*; VCH Publishers: New York, 1989.

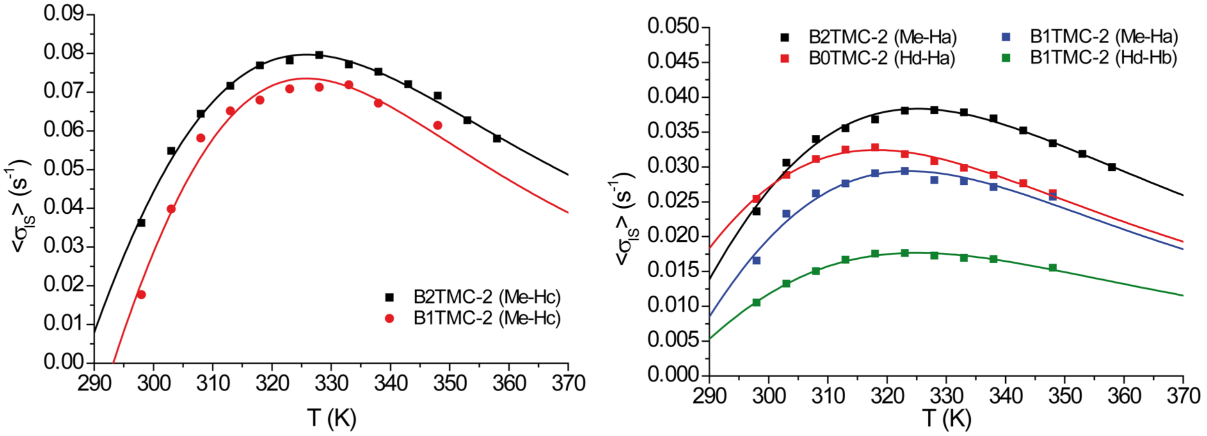

Figure S1.1. Cross-relaxation rate constants σ_{IS} for **B0TMC-2**, **B1TMC-2** and **B2TMC-2** measured from 1D-NOESY NMR experiments in dry DMSO-d$_6$ as a function of temperature.

Table S1.4. Average internuclear distance $<r_{IS}>$ (Å) and correlation time τ_c (10^{-12} s, at 298 K) estimated from the best nonlinear least-squares fit of cross relaxation data for **B0TMC-2**, **B1TMC-2** and **B2TMC-2**.

	$<r_{IS}>$	τ_c
	B0TMC-2	
H_d-H_a	3.01	245
	B1TMC-2	
M_e-H_c	2.63	372
M_e-H_a	3.06	294
H_d-H_b	3.33	295
	B2TMC-2	
M_e-H_c	2.59	326
M_e-H_a	2.95	285

In order to correlate the experimentally determined internuclear distances between aromatic (Me or H_d groups) and benzimidazole (H_a and H_b protons) moieties with the average twist angle in solution (θ, Scheme S1.1), average internuclear distances (under r_{IS}^{-6} averaging)[5] as a function of dihedral twist angle were computed from X-ray structures. The comutation was performed using the following assumptions. *i*) Considering that, out of the two average Me-H_c distances computed for the two limiting static conformations, having one shorter and one longer Me-H_c distances (2.62 and 2.84, respectively, Scheme S1.2), the former compares well with the experimentally measured Me-H_c distance (about 2.6 in both **B2TMC-2** and **B1TMC-2**),[6] only conformations having one shorter Me-H_a distances were considered, when computing average Me-H_a distances as a function of θ for each Me-H_a pairs.[7] *ii*) For the symmetric systems (**B2TMC-2** and **B0TMC-2**), were H_a and H_b are magnetically equivalents,[8] only the conformation in which the two n-alkyl chains points in opposite directions, with respect to the benzimidazole moiety (conformation *anti*, Scheme S1), was considered. *iii*) The situation is more complex in the case of the asymmetric system **B1TMC-2**, for which H_a and H_b are magnetically inequivalents (δ_{Ha} = 4.11 ppm, δ_{Hb} = 4.38 ppm at 298 K). The experimental observation that Me-H_a and H_d-H_b NOEs are stronger than the corresponding Me-H_b and H_d-H_a NOEs (Figure S1.2) can still be compatible with the presence of only the *anti* conformation (Scheme S1.1); However, the observation that the $NOE_{Hb\text{-}He}$ is about 1.35 time stronger than the $NOE_{Ha\text{-}He}$ (Figure S1.2) suggests the presence of an additional conformation in which the Hb moiety is closer to He. The simplest way to model this experimental evidence is to

---

[5] Neuhaus, D.; Williamson, M., *The Nuclear Overhauser Effect in Structural and Conformational Analysis*. VCH Publishers: New York, 1989.

[6] This is due to the well-known phenomenon that the NOEs tends to overweight shorter distances, due to r-6 dependence.

[7] This means that, in the case of **B2TMC-2** for example, only 24 static distances (instead of 48) are averaged for each value of θ and a given conformation of the two n-alkyl chains.

[8] In principle, the two pairs of methylene hydrogens closer to nitrogen atoms should be different because R≠R'. However, since R = C4 alkyl chain and R' = C5 alkyl chains, the difference in chemical shift is negligible.

consider the presence of the *syn* conformation in which the two n-alkyl chains are pointing toward the same directions with respect to the benzimidazole plane (Scheme S1.1).[9] Assuming that the observed $NOE_{Hb\text{-}He}/NOE_{Ha\text{-}He}$ ratio is only due to the relative fraction of *anti* and *syn* conformations, lead to estimate the percent population of *anti* (86%) and *syn* (14%) conformers. Consequently, computed average Me-H_a and H_d-H_b distances as a function of θ are weighted for the percent population of *anti* and *syn* isomer.

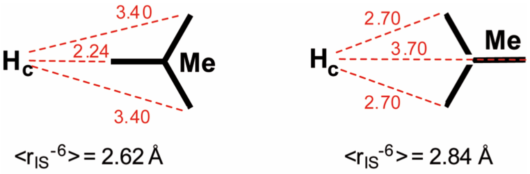

Scheme S1.2. Limiting static conformations of Me moiety and H_c protons in the benzene ring of **B0TMC-2**, **B1TMC-2** and **B2TMC-2** chromophores.

---

[9] For simple steric considerations, out of the two possible *syn* conformations, only the one with both n-alkyl chains pointing toward Hd is considered.

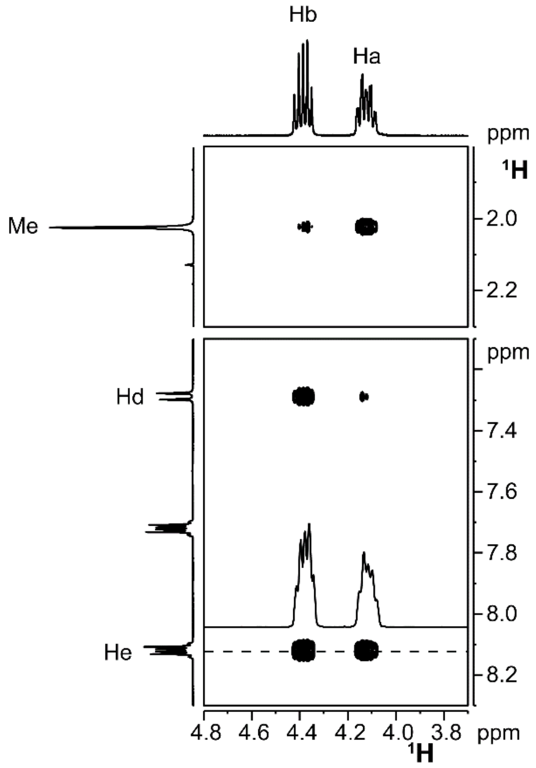

Figure S1.2. Two sections of 2D NOESY NMR experiment of **B1TMC-2** (DMSO-d_6, 323 K) showing that: *i*) Me-H_a and H_d-H_b NOE contacts are much stronger than Me-H_b and H_d-H_a ones; *ii*) H_e-H_b NOE interaction is stronger than H_e-H_a one.

Under those assumptions, average internuclear distances as a function of dihedral twist angle θ (approximately equal to 60°, 65°, 70°, 75°, 80°, 85° and 90°) for **B0TMC-2**, **B1TMC-2** and **B2TMC-2** were computed. The results are reported in Figure 1.4 of the main text. It must be noted that, considering the simplified approach described above, these computed average distances are somewhat biased toward shorter distances (i.e. toward the distance of closest approach); consequently, the derived twist angle in solution (obtained by comparing experimental internuclear distances with computed ones, Figure 4 of the main text) are somewhat underestimated, representing a kind of lower limit for θ. First of all, it does appear that θ values for **B1TMC-2** are very similar if estimated using $NOE_{Me\text{-}Ha}$ (77°) or $NOE_{Hd\text{-}Hb}$ (78°), suggesting that the assumptions are reasonable. Concerning the comparison between the three chromophores, there is no doubt that

B0TMC-2 exhibits the smallest twist angle (64°) in solution. However, **B1TMC-2** and **B2TMC-2** were found to have very similar twist angles (77-78° and 76°, respectively), according to the present analysis.

S1.5. Crystallographic information. Single crystals of **BXTMC-2** chromophores were grown by layering of n-hexane on to a dichloromethane solution. Crystals were mounted in inert oil and transferred to a nitrogen stream on the diffractometer, equipped with a Bruker Kappa APEX CCD area detector and a CuKα microsource with MX optics or a MoKα source with graphite optics. The crystal was maintained at 100 K during data collection. Structures were solved by direct methods in Olex2,[10] and structural refinements were made with using ShelXL.[11]

Table S1.5. X-ray Crystallographic Data for **B0TMC-2**, **B1TMC-2**, and **B2TMC-2**

Compound	**B0TMC2**	**B1TMC-2**	**B2TMC-2**
Formula	$C_{27}H_{32}N_4$	$C_{28}H_{34}N_4$	$C_{29}H_{36}N_4$
Molecular Weight	412.6	426.6	440.6
Crystal System	Monoclinic	Triclinic	Triclinic
Space Group	$P2_1/n$	$P\bar{1}$	$P\bar{1}$
T (K)	100	100	100
a (Å)	9.1171(6)	9.6621(10)	10.2578(6)
b (Å)	17.2703(14)	14.6897(17)	13.5871(8)
c (Å)	15.3013(11)	17.747(2)	18.4790(11)
α (°)	90	90	90
β (°)	100.518(4)	104.666(5)	104.030(3)
ɣ (°)	90	90	90

---

[10] Dolomanov, O. V.; Bourhis, L. J.; Gildea, R. J.; Howard, J. A. K.; Puschmann, H., *Appl. Crystallogr.* **2009,** *42*, 339-341.

[11] Sheldrick, G. M., *Acta. Crystallogr. Sect. A* **2007,** *64*, 112-122.

V (Å^3)	2368.8(3)	2436.8(5)	2498.7(3)
Z	4	1	1
Reflections Collected	4141	7052	7222
Observed Reflections	3311	6827	6961
Restraints/Parameters	130/318	0/583	0/885
R1	0.1337	0.1313	0.0791
*w*R2	0.4460	0.3236	0.2109
GooF	2.109	1.081	1.089

S1.6. Extracting parameters from optical spectra

S1.6.1 Excited state dipole moment and $\Delta\mu_{eg}$. The McRae equation provides a simple means to calculate $\Delta\mu_{eg}$ from the change in CT absorption ($\Delta\lambda_{max}$) in solvents of differing polarity.[12,13,14] The solvent polarity function $f(\varepsilon, n^2)$, defined here by the dielectric constant (ε) and refractive index (n), is related to the change in absorption energy (in wavenumbers) between a chromophore in solution and in vacuum.

$$v - v_0 = -mf(\varepsilon, n^2) \qquad \text{(S1.2)}$$

Here v is absorption maximum in solvent, and v_0 is the maximum in vacuum. The slope m is the slope related to $\Delta\mu_{eg}$, via eq. S1.3, where ε_0 is the permittivity of a vacuum, h is planks constant, c the speed of light, a_0 is the Onsager cavity radius, and μ_g is the DFT derived ground state dipole moment.

---

[12] McRae, E. G., *J. Phys. Chem.* **1957,** *61*, 562.

[13] Manohara, S. R.; Kumar, V. U.; Shivakumaraiah; Gerward, L., *Mol. Liq.* **2013,** *181*, 97.

[14] Grabowski, Z. R.; Rotkiewicz, K.; Rettig, W., *Chem. Rev.* **2003,** *103*, 3899.

$$\Delta\mu_{eg} = \frac{4\pi\varepsilon_0 hca_0^3}{\mu_g} m \tag{S1.3}$$

We have taken the Onsager cavity radius (a_0) to be half the length of the π conjugated region. Fitting of solvatochromic data for **BXTMC-2** chromophores then allows for extraction of the $\Delta\mu_{eg}$ as reported in Table S1.6.

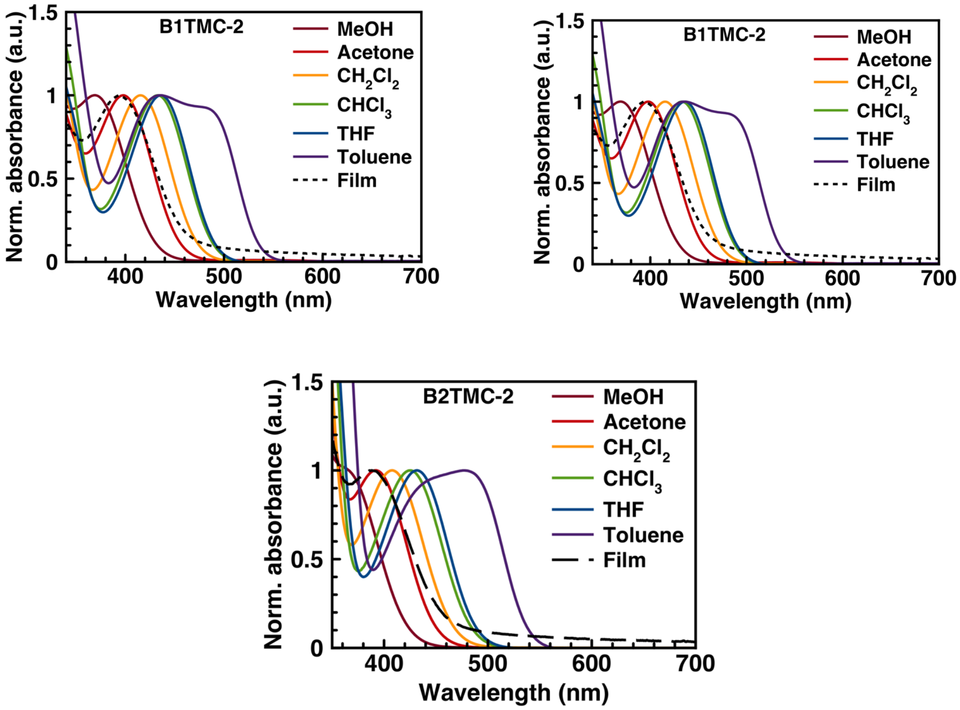

Figure S1.3. Solvatochromic measurement of BXTMC-2 chromophores. Films were spin-coated onto glass substrates using $CHCl_3$ solution.

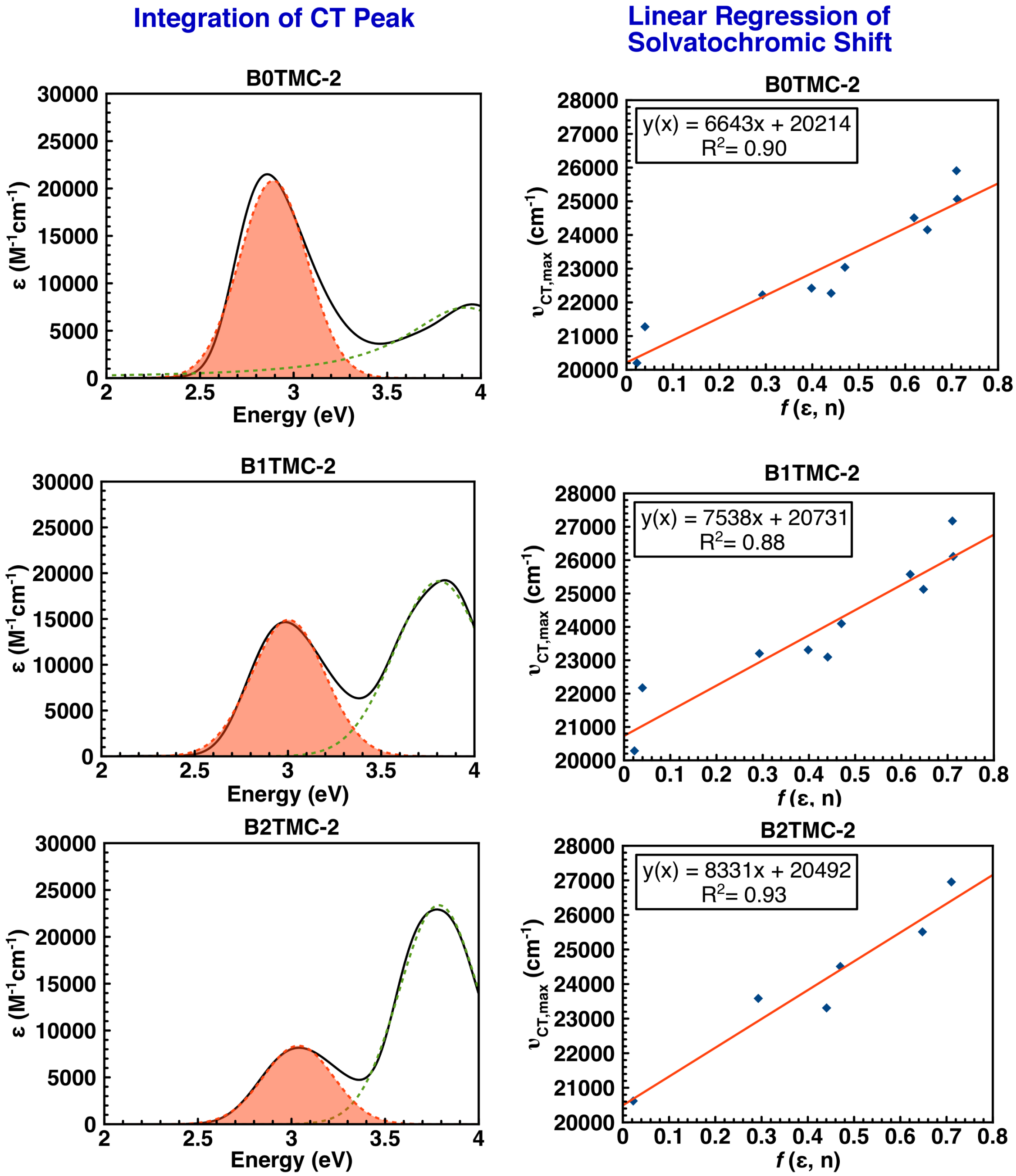

Figure S1.4. Extraction of parameters from optical absorption. *Left*: CT peaks are fit to estimate transition dipole moments. *Right*: Linear regression of solvatochromic shift of the CT maximum.

S1.6.2 Extraction of transition moments. The transition moment can be extracted by integrating the CT peak when ε ($M^{-1}cm^{-1}$) is plotted against E (eV).[15]

$$\left|\mu_{eg}^{*}\right|^{2}=\left(\frac{9.13\times10^{-3}}{E_{eg}}\right)\int_{0}^{\infty}\varepsilon(E)dE \qquad \text{(S1.4)}$$

The two lowest energy transitions in DCM can be de-convoluted, allowing for extraction of the CT transition moments.

Table S1.6. Parameters extracted from optical spectra of BXTMC-2 in DCM.

	υ_0 (cm^{-1})	a_0 (Å)**	*m*	μ_g (D)*	$\Delta\mu_{eg}$ (D)	μ_{eg} (D)
B0TMC-2	20214	5.8	6643 ± 780	21.2	-12.36 ± 1.5	5.45
B1TMC-2	20731	5.8	7538 ± 965	23.5	-12.67 ± 1.6	4.72
B2TMC-2	20492	5.8	8331 ± 1130	24.6	-13.37 ± 1.8	3.43

*computed using DFT, see table HF/6-31G** geometry **taken as ½ the pi system length as determined by the crystal structure.

S1.7. Computational methodology. Structures were optimized in Q-Chem[16] at the HF and B3LYP level with a 6-31G** basis set in the gas phase (with no geometric constraints). The HF optimized structures showed closer agreement to the measured torsional angles. The alkyl chains were truncated to simplify geometry optimizations; an ethyl group is sufficient to accurately obtain the steric interaction which defines the torsional angle. Structures were checked for imaginary vibrational modes to confirm an energy minimum. Excited state dipole moments were calculated

---

[15] Perez-Moreno, J.; Zhao, Y.; Clays, K.; Kuzyk, M. G.; Shen, Y.; Qiu, L.; Hao, J.; Guo, K., Modulated Conjugation as a Means of Improving the Intrinsic Hyperpolarizability. *J. Am. Chem. Soc.* **2009,** *131*, 5084-5093.

[16] Shao, Y.; Gan, Z.; Epifanovsky, E.; Gilbert, A. T. B.; Wormit, M.; Kussmann, J.; Lange, A. W.; Behn, A. *et al.* Advances in molecular quantum chemistry contained in the Q-Chem 4 program package. *Molecular Physics* **2015,** *113* (2), 184-215

in Q-Chem using TDDFT CAM-B3LYP/6-31G**. Qualitatively good agreement with experimental spectra suggests that the electronic structures calculated in the gas phase are similar to those observed experimentally in solution. Discrepancy in $\Delta\mu_{eg}$ likely results of the stabilization from dipole moments in solution versus gas, our estimation of Onsager cavity, or a combination of factors. We also note that without geometric constraints, the torsional angles are close, but do not exactly match those determined by NOE and crystallographic characterization. We did not pursue nonlinear optical properties calculations.

Table S1.7. Gas phase HF/6-31G** geometries, TDDFT using CAM-B3LYP/6-31+G**

	twist angle	E_{01} (eV)	E_{02} (eV)	μ_g (D)	$\Delta\mu_{ge}$ (D)
B0TMC-2	51.1	3.0	4.1	21.22	-19.5
B1TMC-2	67.9	2.7	3.8	23.46	-24.6
B2TMC-2	89.0	2.4	3.8	24.58	-27.4

Table S1.8. Gas phase B3LYP/6-31G** geometries, TDDFT using CAM-B3LYP/6-31+G**

	twist angle	E_{01} (eV)	E_{02} (eV)	μ_g (D)	$\Delta\mu_{ge}$ (D)
B0TMC-2	41.7	3.0	3.9	20.71	-14.95
B1TMC-2	53.6	2.8	3.9	21.73	-18.50
B2TMC-2	68.0	2.6	4.0	23.05	-22.41

S1.8. Cyclic voltammetry. CV solutions were prepared containing 0.1 M Bu_4NPF_6 in anhydrous acetonitrile; the chromophores measured at ~2 mM concentration, and solutions were bubbled with N_2 to displace oxygen. Measurements were performed using a glassy carbon working electrode, Ag/AgCl reference, and referenced to Fc/Fc+, scanning at a rate of 50 mV/s.

Table S1.9. Cyclic voltammetry of BXTMC-2.

	E_{ox} (eV)	E_{red} (eV)	E_{01} (eV)
B0TMC-2	0.24	-1.94	2.18
B1TMC-2	0.36	-2.03	2.39
B2TMC-2	0.34	-2.10	2.44

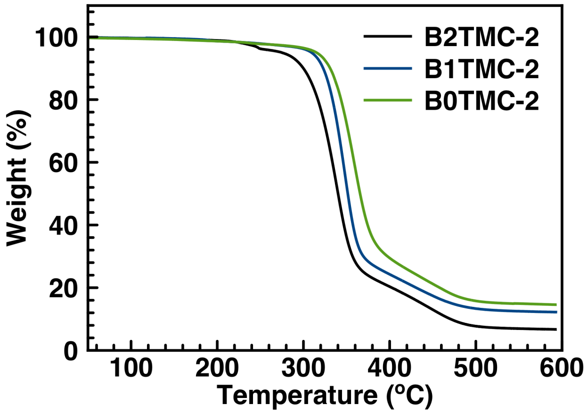

Figure S1.5. TGA analysis with ramp rate of 10 ºC/min under N_2.

Chapter 2 Appendix

S2.1. Materials synthesis and characterization. Reagents were purchased from Sigma Aldrich and used without purification unless otherwise noted. The commercially obtained tetrabutyl phosphonium bromide ($Bu_4P^+Br^-$) and tetrabutylammonium bromide ($Bu_4N^+Br^-$) was pure by NMR and showed very low levels of visible absorption which were subtracted as baseline in UV-Vis experiments. $Bu_4P^+Br^-$ was dried at > 100 °C under vacuum for several days to minimize the water content. Solutions used for optical absorption, NMR, and vibrational spectroscopy studies were treated with basic alumina to eliminate trace levels of acid. All samples were then dried over 4Å molecular sieves. Chromophore **B2TMC-2** was synthesized and purified as reported previously.[17] Films were spin coated (4000 rpm, 30s) onto glass substrates from solutions with 20 mg/mL PMMA, 4 mg/mL chromophore, with varied amount of $Bu_4P^+Br^-$ (0.4 mg/mL, 2 mg/mL, and 10 mg/mL) in $CHCl_3$. The films are expected to approximately reflect the composition of the solutions from which they were cast.

S2.2. Solvatochromic measurements with $Bu_4P^+Br^-$ and $Bu_4N^+Br^-$ in $CHCl_3$. The same experiment performed for $Bu_4P^+Br^-$ was repeated with nitrogen analogue $Bu_4N^+Br^-$ (Figure S2.1, left). In literature, it is common to see selective solvation of similar probe molecules, such as Reichardt's Dye by organic salts in binary organic salt/organic solvent mixtures.[18] Such trends are

---

[17] Lou, A. J.-T.; Righetto, S.; Barger, C.; Zuccaccia, C.; Cariati, E.; Macchioni, A.; Marks, T. J. Unprecedented Large Hyperpolarizability of Twisted Chromophores in Polar Media. *J. Am. Chem. Soc., submitted* **2018**.

[18] Ab Rani, M. A.; Brant, A.; Crowhurst, L.; Dolan, A.; Lui, M.; Hassan, N. H.; Hallett, J. P.; Hunt, P. A.; Niedermeyer, H.; Perez-Arlandis, J. M.; Schrems, M.; Welton, T.; Wilding, R. Understanding the Polarity of Ionic Liquids. *Phys. Chem. Chem. Phys.* **2011**, *13*, 16831-16840; (c) Reichardt, C. Pyridinium N-phenolate Betaine Dyes as Empirical Indicators of Colvent Polarity: Some New Findings. *Pure Appl. Chem.* **2004**, *76*, 1903-1919.

also present in the salt/**B2TMC-2** system as evidenced by the initial decrease in λ_{CT} below 5% salt (Figure S2.1, right), and are confirmed by NMR experiments (below).

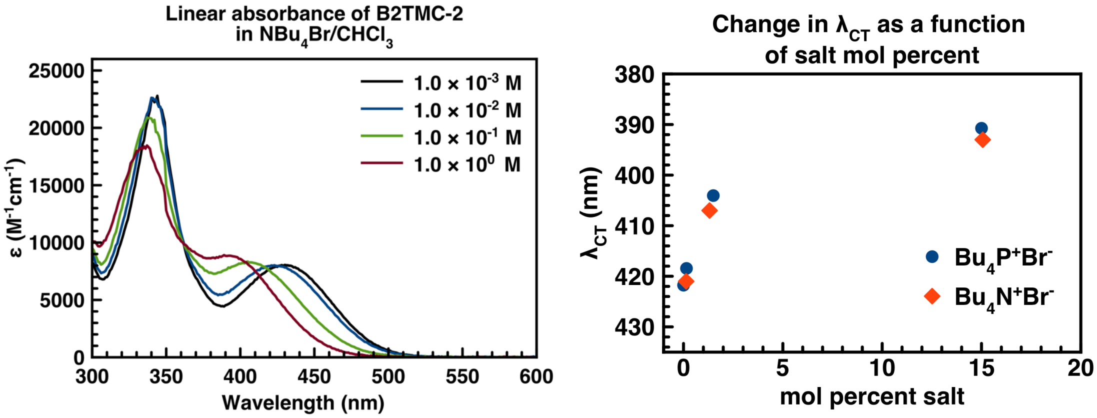

Figure S2.1. *Left*: UV-Vis spectroscopy of **B2TMC-2** in $CHCl_3$ with various amounts of $Bu_4N^+Br^-$. *Right*: CT maximum with respect to salt mol percent

To confirm that spectroscopic changes are a result of halochromism and not related to changes in aggregation, concentration dependent measurements in $CHCl_3$ were pursued, and showed consistnet λ_{CT} over ~2 orders of magnitude dilution.

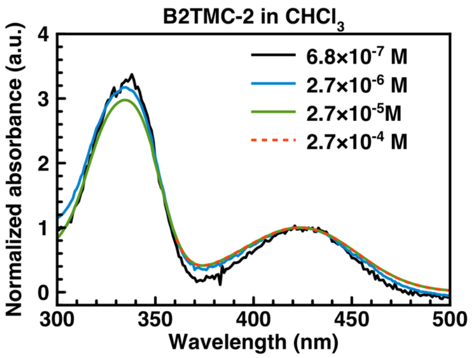

Figure S2.2. Linear optical absorption of **B2TMC-2** in $CHCl_3$

S2.3. Infrared vibrational spectroscopy of B2TMC-2 in $Bu_4P^+Br^-/CHCl_3$ solution. Vibrational spectroscopy was performed to observe changes in the CN stretching modes with increasing concentrations of $Bu_4P^+Br^-$ (Figure S2.3). These modes are known to be sensetive to the amount of neagative charge on the dicyanomethanide donor group, and thus are diagnostic of the chromophroe electronic strucutre. Shifts in the main *v*(CN) peak from 2175 ± 0.1 to 2172 ±

0.2 cm^{-1} and the low energy side component from 2139 ± 0.1 to 2135 ± 0.3 cm^{-1} suggest that the electron density is increased by the presence of $Bu_4P^+Br^-$ salt. Other diagnostic regions of the IR spectrum proved difficult to interpret due to overlap of peaks from the highly concentrated $Bu_4P^+Br^-$ salt.

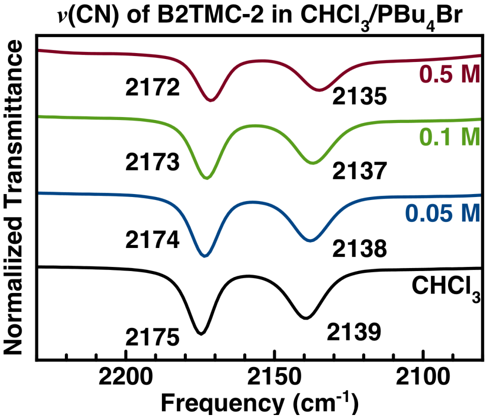

Figure S2.3. Infrared vibrational spectroscopy of **B2TMC-2** in pure $CHCl_3$ and $CHCl_3$ with 0.05, 0.1, and 0.5 M $Bu_4P^+Br^-$. The area shown encompasses the v(C≡N) in-phase (2172-2175 cm^{-1}) and out of phase (2135-2139 cm^{-1}) vibrations.

S2.4. NMR with varied concentration of $Bu_4P^+Br^-$ and $Bu_4N^+Br^-$ in $CDCl_3$. NMR experiments were performed by adding stock solution of salt/$CDCl_3$ to a **B2TMC-2**/$CDCl_3$ solution at room temperature (Figure S2.4). Because of the impact of the salt on solvent chemical shift, the spectra were shifted such that the chemical shift of the salt and silicone internal standard remained constant. The solvent ($CHCl_3$) signal is removed from figures for visual clarity. Plots of the donor and aceptor chemical shifts in the prenece of $Bu_4P^+Br^-$ and $Bu_4N^+Br^-$ suggest selective solvation of **B2TMC-2** (Figure S2.5), similar to what was seen in UV-Vis.

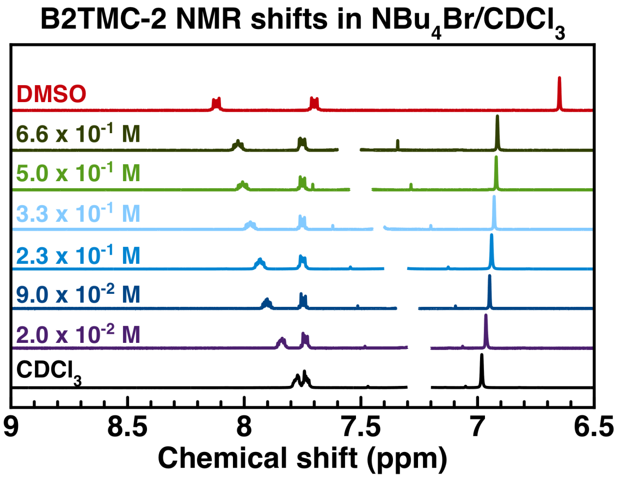

Figure S2.4. NMR chemical shifts of the aromatic region of **B2TMC-2** with increasing amounts of $Bu_4N^+Br^-$ in $CDCl_3$

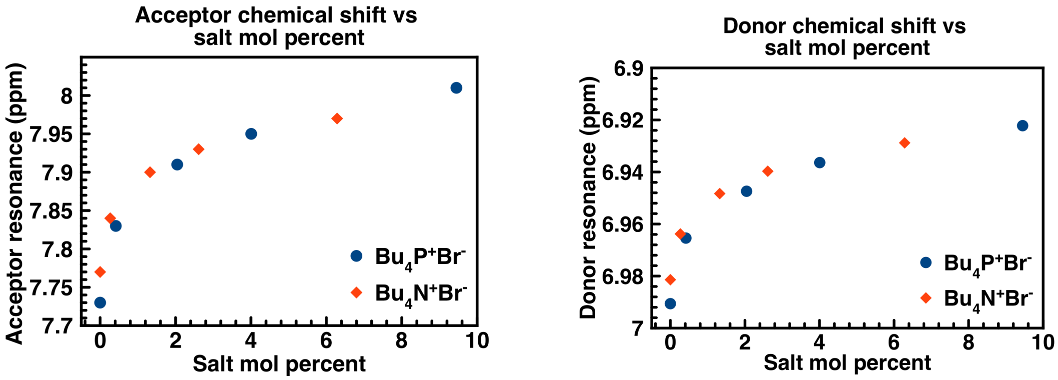

Figure S2.5. Acceptor (left) and donor (right) chemical shifts as a function of salt mol percent

S2.5. EFISH experimental details and full results. EFISH measurements were carried out on solutions of CH_2Cl_2 and $CHCl_3$ with an incident wavelength of 1907 nm, obtained by Raman-shifting the fundamental 1064 nm wavelength produced by a Q-switched, mode-locked Nd^{3+}:YAG laser manufactured by Atalaser. The $\mu\beta$ values reported are the mean values of several measurements performed on the same sample. $CHCl_3$ was treated with basic Al_2O_3 prior to use. In addition, $CHCl_3$ was also distilled from CaH_2 to remove trace amount of water when the measurements were performed in the presence of $Bu_4P^+Br^-$. β_{vec} is calcaulted usign the DFT derived ground state dipole moment in footnote 17, using the highest reliable dilution.

Table S2.2. EFISH and linear absorption of **B2TMC-2** in solutions of $Bu_4P^+Br^-/CHCl_3$, CH_2Cl_2, and $CHCl_3$

$[Bu_4P^+Br^-]$ (M)	λ_{CT} (nm)	$\mu\beta_{vec}$ ($\times 10^{-48}$ esu) 1.0×10^{-3}	5.0×10^{-4}	1.0×10^{-4}	5.0×10^{-5}
Pure $CHCl_3$	425	-875 ± 154	----	-2,160 ± 425	------
(A) 1.0×10^{-4}	425	----	----	-13,000 ± 1300	----
(B) 5.0×10^{-2} (a)	411	----	-9,760 ± 9760	-18,400 ± 1190	-22,160 ± 2660
(C) 1.0×10^{-1}	403	-2,190 ± 219	-10,760 ± 753	-----	-----
(D) 5.0×10^{-1}	400	-2,760 ± 550	----	-20,140 ± 1200	-----
Pure CH_2Cl_2	404	-----	----	-9,660 ± 1546	-19,620 ± 2354

(a) the μβ of $Bu_4P^+Br^-$ at this concentration resulted in a very low value (-23.7×10^{-48} esu) which is maintained at higher concentration.

S2.6. Typical ion pair distances in the solid state.[19] In the **B2TMC-2**/$Bu_4P^+Br^-$ solutions, there are four possible cation/anion pairings between the salt and the benzimidazolium cation, Bz^+, and the dicyanomethanide anion, $RC(CN)_2^-$. Crystallographic structures of the relevant ion pairs can be found in literature (Figure S2.7); in such coulombic interactions, the cation-anion distance is suggestive of the strength of the interaction. Bz^+/Br^- and Bz^+/I^- exhibit ion pair distances of ~3.7 - 4.1 Å, measured by the shortest N--halogen distance. This is shorter than the P--X (X = Cl^- and

---

[19] (a) Lou, A. J.-T.; Righetto, S.; Barger, C.; Zuccaccia, C.; Cariati, E.; Macchioni, A.; Marks, T. J. Unprecedented Large Hyperpolarizability of Twisted Chromophores in Polar Media. *J. Am. Chem. Soc., submitted* **2018**; (b) Wright, A. G.; Weissbach, T.; Holdcroft, S. Poly(phenylene) and m-Terphenyl as Powerful Protecting Groups for the Preparation of Stable Organic Hydroxides. *Angew. Chem. Int. Ed.* **2016**, *55*, 4818-4821; (c) Zhuo, J.-B.; Zhu, X.-X.; Lin, C.-X.; Bai, S.; Xie, L.-L.; Yuan, Y.-F. Design, Synthesis and Anion Recognition of Ferrocene-Based Benzimidazolium Receptors. *J. Organomet. Chem.* **2014**, *770*, 85-93; (d) Adamova, G.; Gardas, R. L.; Nieuwenhuyzen, M.; Puga, A. V.; Rebelo, L. P.; Robertson, A. J.; Seddon, K. R. Alkyltributylphosphonium Chloride Ionic Liquids: Synthesis, Physicochemical Properties and Crystal Structure. *Dalton Trans.* **2012**, *41*, 8316-8332; (e) Muromachi, S.; Takeya, S.; Yamamoto, Y.; Ohmura, R. Characterization of Tetra-n-butylphosphonium Bromide Semiclathrate Hydrate by Crystal Structure Analysis. *Cryst. Eng. Comm.* **2014**, *16*, 2056-2060; (f) Dean, P. M.; Fraser, K. J.; MacFarlane, D. R. CCDC: 740286. *CSD Comm.* **2009**; (g) Turner, D. R.; MacDonald, R.; Teng Lee, W.; Batten, S. R. Ammonium Salts of Carbamoyldicyanomethanide, $C(CN)_2(CONH_2)^-$: Effects of Hydrogen-Bonding Cations on Anionic Networks. *Cryst. Eng. Comm.* **2009**, *11*, 298-305; (h) Yi, C.; Blum, C.; Liu, S.-X.; Ran, Y.-F.; Frei, G.; Neels, A.; Stoeckli-Evans, H.; Calzaferri, G.; Leutwyler, S.; D'ecurtis, S. A Layered Red-Emitting Chromophore Organic Salt. *Cryst. Growth Des.* **2008**, *8*, 3004-3009; (i) Benaissa, I.; Taakili, R.; Lugan, N.; Canac, Y. A Convenient Access to N-Phosphonio-Substituted NHC Metal Complexes [M = Ag(i), Rh(i), Pd(ii)]. *Dalton Trans.* **2017**, *46*, 12293-12305.

Br^-) distance in Bu_4P^+, which is ~4.1 - 4.4 Å. In the absence of suitable $Bu_4P^+/RC(CN)_2^-$ crystal structures in the CSD or in open literature, we expect that the structural similarity of $Bu_4N^+Br^-$ and $Bu_4P^+Br^-$ will lead to comparable interactions with $RC(CN)_2^-$. The typical N--carbanion distance in $Bu_4N^+/RC(CN)_2^-$ is between ~4.7 - 5.6 Å. This is longer than in **B2TMC-2**, where the interaction of Bz^+ and $RC(CN)_2^-$ exhibits a N--carbanion distance of 4.5 Å. These isolated ion pair distances suggest that both Br^- and $RC(CN)_2^-$ have a stronger interaction with Bz^+ than Bu_4P^+, likely as a result of the Bu_4P^+ bulky *n*-Bu groups. This is in good agreement with our observation that $Bu_4P^+Br^-$ has little impact on δ_{Hc}, but leads to large changes in δ_{Ha} and λ_{CT}.

Figure S2.6 demonstrates the direct competition of imidazolium (Im^+)/Br^- and phosphonium (R_4P^+)/Br^- interactions in a tethered di-cationic complex. Im^+ is similar to Bz^+ both in electronic and physical structure, with the typical N--Br distance in Im^+/Br^- crystals on the order of ~3.4 - 4.1 Å. In Figure S6, the Im^+/Br^- N--Br distance (~4.0 Å) is similar to that in pure Im^+/Br^- crystals while the shortest P--Br distance is ~4.7 - 4.9 Å, which is ~0.4 - 0.6 Å longer than in $Bu_4P^+Br^-$. The overall magnitude of the interaction, and the elongation of P--Br is further evidence of the preference for Im^+/Br^- interactions over R_4P^+/Br^- ones.

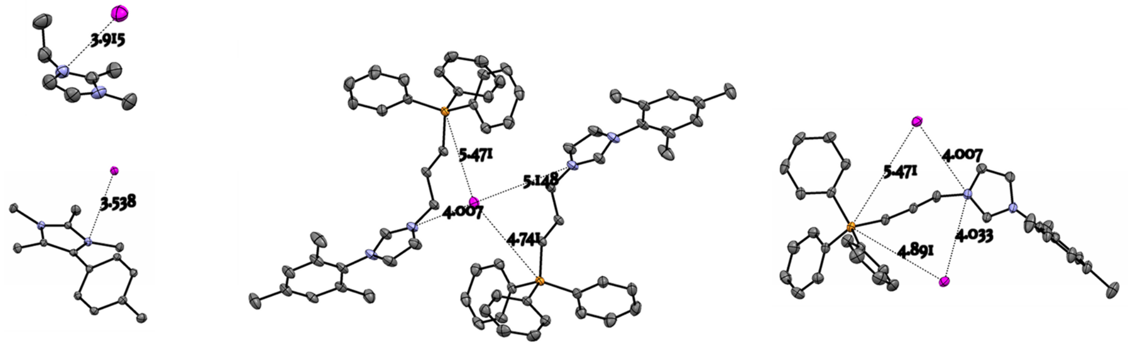

Figure S2.6. Crystal structures accessed by the CSD. Left: Im^+/Br^- with closest Br--N labeled; Center and right: Tethered di-cation system showing competition of R_4P^+ and Im^+ for coulombic interactions with Br^- (pink).

Benzimidazolium/halogen

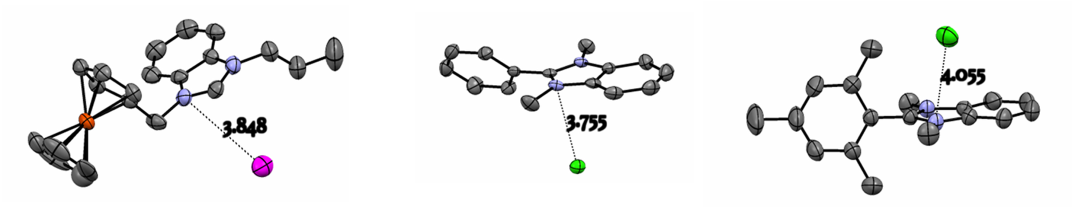

Tetrabutylphosphonium/halogen

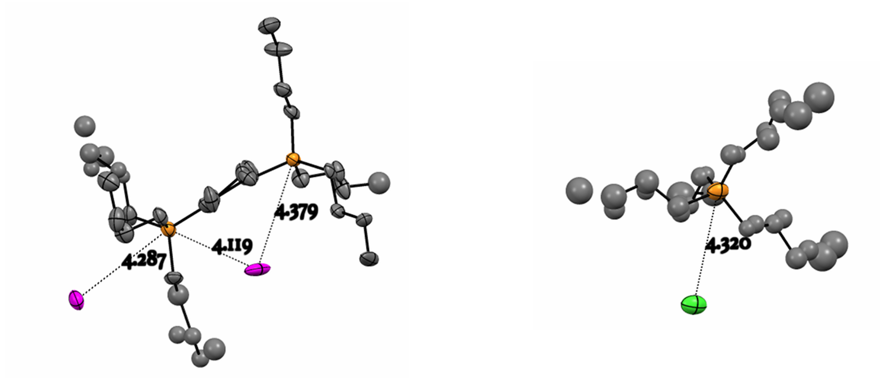

Tetraakylammonium/dicyanomethanide

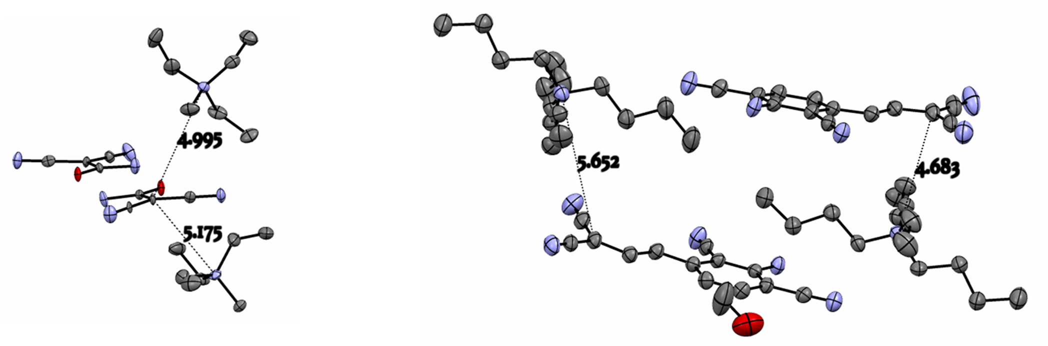

B2TMC-2: benzimidazolium/dicyanomethanide

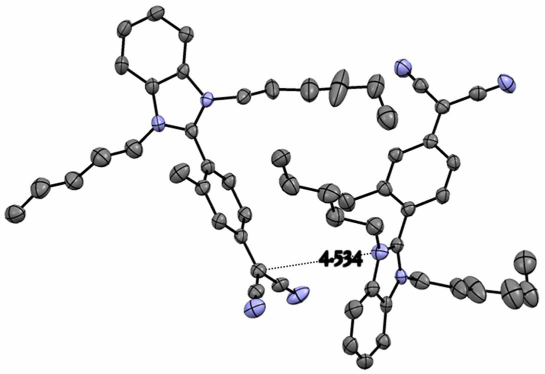

Figure S2.7. Crystal structured accessed by the CSD, atoms are color coded nitrogen (light blue), oxygen (red), carbon (grey), bromine (pink), chlorine (green). *Panel 1*: Measured distance of the shortest N--anion distance in $Bz^{+}X^{-}$; *Panel 2*: Anhydrous crystal structures of $Bu_4P^{+}X^{-}$; *Panel 3*: Representative $Bu_4N^{+}RC(CN)_2^{-}$ salts; *Panel 4*: Closest N--carbanion distance in **B2TMC-2** crystal structure.

Chapter 3 Appendix

S3.1. Materials and methods. All reagents were purchased from Sigma-Aldrich and used without further purification unless otherwise noted. Tetrahydrofuran (THF), dichloromethane (CH_2Cl_2), and toluene were dried by passing through a column of activated alumina under argon. The reagent 2,5-dibromo-1,3-dimethylbenzene was purchased from Combi-Blocks. NMR spectra were recorded on Varian Mercury-400 MHz and INOVA-500 MHz spectrometers. Low resolution mass spectra were recorded on Amazon X and Amazon SL LC-ESI mass spectrometer. Elemental analysis was performed by Midwest Microlab. Optical spectra were recorded using an Agilent Cary 5000 spectrophotometer.

S3.2. Z-scan measurements. The sensitivity of the nonlinear optical measurements of nonlinear refraction can be improved by an order of magnitude by using the dual-arm (DA) Z-scan technique[20] compared to the single arm Z-scan.[21] In this methodology, the solvent is placed in one arm and the solution is placed in another arm with identical experimental parameters. In order to correlate the noise between two arms (e.g. pulse energy, beam waist, pulse width, and beam pointing, etc.), the scans are performed simultaneously.

In this work, a Ti:Sapphire femtosecond laser (Clark-MXR) producing 1 mJ pulse energy at a 1 kHz repetition rate at 800 nm is used to pump an optical parametric amplifier (OPA) TOPAS-C whose output can be tuned in the range of 1100-2600 nm. The measurements at 800 nm are

---

[20] Ferdinandus, M. R.; Reichert, M.; Ensley, T. R.; Hu, H.; Fishman, D. A.; Webster, S.; Hagan, D. J.; Van Stryland, E. W. Dual-Arm Z-scan Technique to Extract Dilute Solute Nonlinearities from Solution Measurements. *Opt. Mater. Express* **2012**, *2*, 1776.

[21] Sheik-Bahae, M.; Said, A. A.; Wei, T. H.; Hagan, D. J.; Van Stryland, E. W. Sensetive Measurement of Optical Nonlinearities Using a Single Beam. *IEEE J. Quantum Electron.* **1990**, *26*, 760-769.

performed using the output of the laser, and measurements at 1100 nm and 1300 nm are performed by fixing the output wavelength from the signal beam of the OPA. At each wavelength, the OA signal for a 0.5 mm thick GaAs and CA signal for 1 mm thick fused silica is recorded to calibrate the setup and to characterize the spot size and relative pulsewidth in each arm. In addition, similar measurements are performed on cuvettes of CS_2 to equalize the two arms. The energies in the two arms are equalized by matching the peak to valley transmission change, $\Delta T_{p\text{-}v}$ for CS_2.[1] The Z-positions (the beam focus at each arm) are equalized by translating one of the stages where the sample is mounted. Open aperture (OA) and closed aperture (CA) signals are recorded simultaneously, and the nonlinear refraction (NLR) is extracted after dividing the CA by OA data to decouple the nonlinear refraction from the nonlinear absorption (NLA) background.

The DA Z-scan signals at wavelengths of 800 nm, 1100 nm, and 1300 nm are shown in the panels (A-F) of Figure S3.1 for several pulse energies. Figure S3.1 (A, C, E) shows the normalized transmission of OA signal and Figure S3.1 (B, D, E) shows the normalized transmission of CA/OA signal as a function of the Z-position indicating NLA and a positive NLR. The OA signal scales linearly with the pulse energy, however, the CA/OA scales quadratically with the pulse energy. This scaling indicates that two-photon absorption (2PA) is the dominant mechanism in NLA and is modeled via the 2PA cross-section, δ_{2PA}. However, a bound-electronic third-order nonlinearity cannot accurately explain the observed behavior of CA/OA. We attribute this behavior to the excited-state refraction induced by 2PA which can be explained via a cascaded $\chi^{(3)}: \chi^{(1)}$ effect. The effective induced change in the phase via nonlinear refraction can be modeled as $\Delta\varphi_{eff} = (k_0 n_2 I + \sigma_{ESR} N)L$, where k_0 (1/m) is the vacuum wavenumber, n_2 (m^2/W) is the bound-electronic third-order nonlinear refraction related to the second hyperpolarizabilty, I (W/m^2) is the beam irradiance, σ_{ESR} (m^2) is the excited-state refraction cross-section, N (m^{-3}) is the density of molecules in the excited

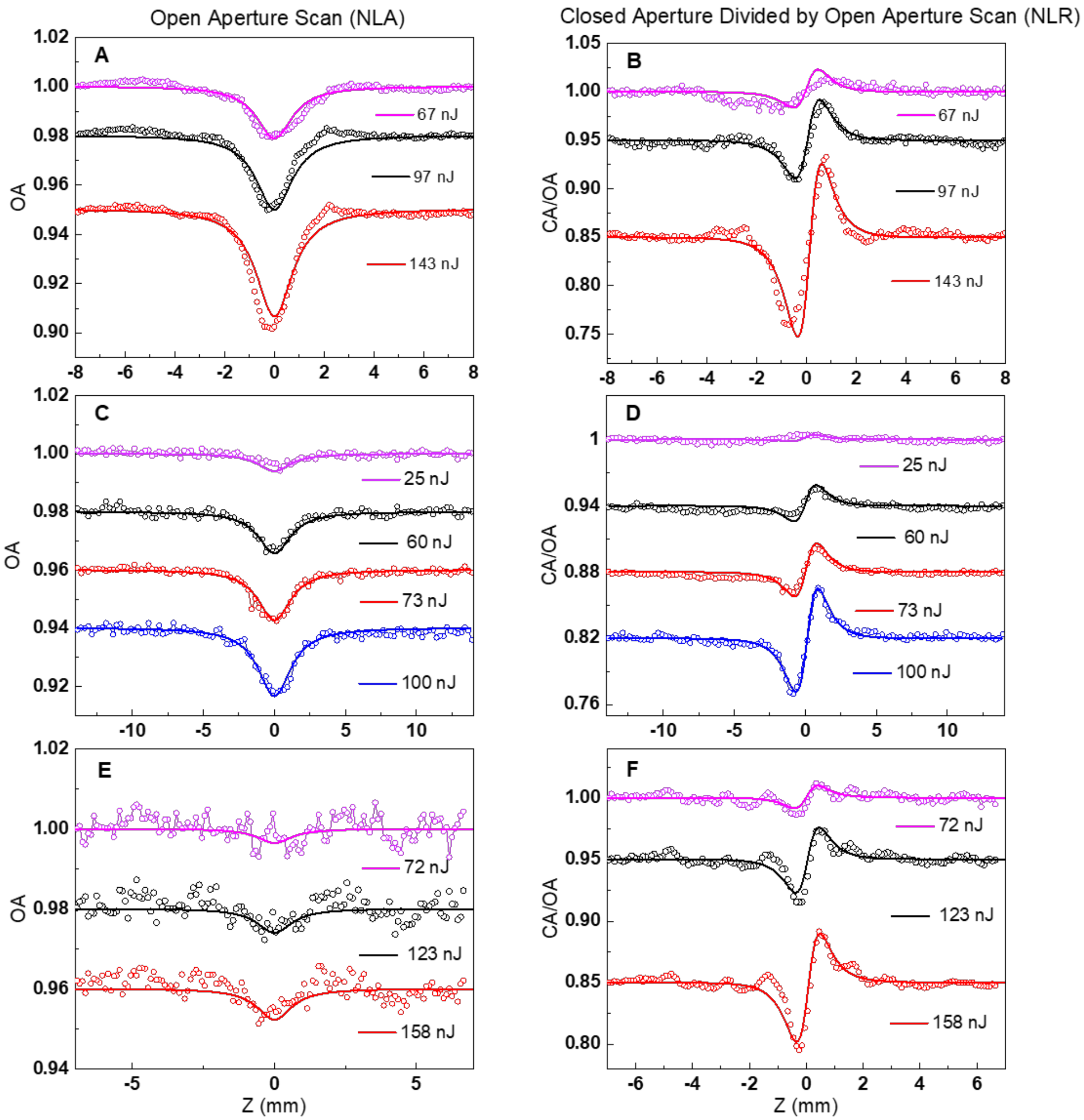

Figure S3.1. Dual arm (DA) Z-scan signals at 800 nm for A) OA, and B) CA/OA, at 1100 nm for C) OA, and D) CA/OA, and at 1300 nm for E) OA, and F) CA/OA for **TMC-3’** solution in dry DCM. The nonlinear effect of the solvent is subtracted for each wavelength when performing dual-arm measurements. Experiments are performed at different laser irradiances in order to characterize the origin of the nonlinearity. Solid lines are the fits to the experimental data using the Z-scan theory indicating 2PA and positive excited-state NLR induced by 2PA.

state induced by 2PA, and L is the sample thickness. Our fittings revealed a very small bound-electronic third-order nonlinear refraction and large excited-state refractive cross-section. The peak–to-valley transmission change, $\Delta T_{p\text{-}v}$, scales quadratically with the pulse fluence (F) with the relation $\Delta T_{p\text{-}v} \sim k_0\, \delta_{2PA}\sigma_{ESR}F^2/\tau$, where τ is the laser pulse width (FWHM).

S3.3. Finite field computation of polarizability. In order to ease the computational burden, structures were computed with truncated side chains, as ethyl groups (**TMC-3'-Et**) for TDDFT and finite field calculations, and as ethyl hexyl groups (**TMC-3'-EH**) in the case of computation of dimers, for which sidechains may play a more important role. The structures were optimized at the B3LYP/6-31G** level in Q-Chem[22] with constrained inter-aryl torsional angles from 65° to 85° in 5° increments, as well as at 89°. The state dipole moments for the ground, ICT, and SFCT states were calculated by TDDFT (CAM-B3LYP/6-31+G**) in the presence of static electric fields (F) applied along the molecular axis, ranging from -0.001 to 0.001 au in 0.0001 au increments. The choice of field strength was based on the desire to preserve the character of the excited states, as well as to prevent the significant contribution of higher order nonlinearities.

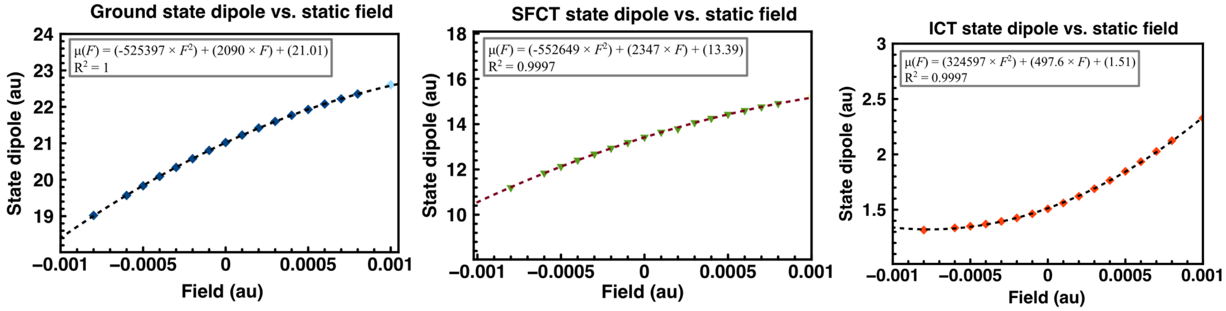

Figure S3.2. Field dependence of TDDFT derived state dipole moments (markers) of **TMC-3'-Et** at 85°, fit with second order polynomial (dotted lines).

---

[22] Shao, Y.; et al. Advances in molecular quantum chemistry contained in the Q-Chem 4 program package. *Molecular Physics* **2015**, *113*, 184-215.

In all cases, a second order polynomial was found to be sufficient for fitting the curves, as is shown in Figure S3.2 for the 85º geometry of **TMC-3'-Et**. Torsional angles below 70º lead to a highly mixed character of the SCFT transition and are therefore not reported. The computed ground and excited state polarizabilities and σ_{ESR} (calculated by eq S3.1)[23] are reported in Table S3.1.

$$\sigma_{ESR} = \frac{4\pi^2}{\lambda}\frac{(n^2+2)^2}{9n}\left(\alpha_{2P} - \alpha_g\right) \tag{S3.1}$$

Table S3.1. α_g, α_{sfct} and σ_{ESR} computed by the FF method, using TDDFT derived ICT and SFCT excited states.

Torsional Angle	α_g (au)	α_{SFCT} (au)	α_{ICT} (au)	σ_{ESR} @ 800 nm (x 10^{-17} cm^2)		
				no change in geometry	5 degree planarization	10 degree planarization
65	2165	---	1042	---	---	---
70	2175	1764	935	-4.14	---	---
75	2178	1957	798	-2.23	-4.17	---
80	2157	2173	645	0.16	-2.01	-3.96
85	2090	2308	495	2.20	0.84	-1.34
89	1342	1563	863	2.23	9.73	8.37

Here we have also taken into account the possibility that the molecular geometry may change slightly upon SFCT, leading to a reduction in the torsional angle. Table S1 reports values for σ_{ESR} for the case of 5º and 10º relaxation. Our computational work is benchmarked to experimentally derived α_g (Table S3.2), which is calculated using the SOS approach with μ_{eg} and E_{eg} values extracted from the linear absorption spectrum in DCM. The static value is in very good agreement

---

[23] Li, F.; Song, Y.; Yang, K.; Liu, S.; Li, C. *Optics Communications* **1998**, *145*, 53-56.

with the FF derived value at 89º geometry, which is consistent with the large torsional angles observed in previous work.[24]

Table S3.2. α_g computed from experimental optical transitions using a three-state SOS model

	Wavelength			
	800 nm	1100 nm	1300 nm	static
α_g (au)	2017	1667	1586	1410

S3.4 Synthesis of TMC-3'

Synthesis of 4-bromo-3,5-dimethylbenzaldehyde (1). Dry THF (200 mL) and 3,5-dibromoxylene (15 g, 56.8 mmol) was added to an oven dried flask under N_2 and cooled to -78 °C. *n*-butyl lithium (2.67 M solution in hexanes, 22.4 mL) was added drop-wise via syringe pump over 30 min. After stirring at -78 °C for 30 min, DMF (13 mL) was added slowly, and the reaction was warmed to room temperature then stirred for 1 h. The reaction mixture was then quenched into 5% HCl, neutralized with saturated $NaHCO_3$, and extracted with ethyl acetate. The organic phase was dried with Na_2SO_4 and the solvent was removed under reduced pressure. The crude product was recrystallized from hexanes to give 10.0 g of the title compound as soft white crystals (83% yield). ^{1}H NMR (500 MHz, $CDCl_3$): δ 9.93 (s, 1H), 7.57 (s, 2H), 2.50 (s, 3H).

Synthesis of 4-(pinacolatoboron)-3,5-dimethylbenzaldehyde (2). To an oven dried schlenk flask, **1** (2.0 g, 9.4 mmol), KOAc (2.8 g 28.2 mmol), $Pd(PPh_3)_2Cl_2$ (330 mg, 0.46 mmol) and B_2Pin_2 (4.8 g, 18.8 mmol) were added under argon atmosphere. 1,4-dioxane (20 mL) was added via syringe, then the flask was sealed and heated to 100 °C for 24 h. The reaction mixture was then

---

[24] (a) Kang, H.; Facchetti, A.; Jiang, H.; Cariati, E.; Righetto, S.; Ugo, R.; Zuccaccia, C.; Macchioni, A.; Stern, C. L.; Marks, T. J. *J. Am. Chem. Soc.* **2007**, *129*, 3267-3286. (b) Shi, Y.; Frattarelli, D.; Watanabe, N.; Facchetti, A.; Cariati, E.; Righetto, S.; Tordin, E.; Zuccaccia, C.; Macchioni, A.; Wegener, S. L.; Stern, C. L.; Ratner, M. A.; Marks, T. J. *J. Am. Chem. Soc.* **2015**, *137*, 12521-12538.

poured into water and extracted with ethyl acetate. The organic layer was dried with Na_2SO_4 and concentrated *in vacuo*. The crude product was purified by column chromatography on silica gel using a gradient of 1−10 % ethyl acetate in hexanes to afford the title compound as 2.13 g of crystalline white solid (87% yield). ^1H NMR (500 MHz, $CDCl_3$): δ 9.93 (s, 1H), 7.44 (s, 2H), 2.46 (s, 6H), 1.41 (s, 12H). $^{13}C\{H\}$ NMR (500 MHz, $CDCl_3$): δ 193.01, 142.54, 136.82, 127.42, 109.99, 84.26, 24.98, 21.99.

Synthesis of 4-(3-methylpyridine)-3,5-dimethylbenzaldehyde (3). An oven dried flask was charged with **2** (1.5 g, 5.77 mmol), K_3PO_4 (4.44 g, 20.96 mmol), 4-chloro-3-methylpyridine hydrochloride (860 mg, 5.24 mmol), Pd_2dba_3 (192 mg, 0.21 mmol) and SPhos (172 mg, 0.42 mmol) under Ar atmosphere. Toluene (18 mL), then degassed water (2 mL) were added and the flask was sealed, then heated to 100 °C for 24 h. The reaction mixture was poured into water, and extracted with ethyl acetate. The organic layer was dried over Na_2SO_4, filtered, and concentrated *in vacuo*. The crude was purified by column chromatography on silica gel using a gradient of 30−100 % ethyl acetate in hexanes to yield 1.06 g of the title product as a yellow oil, which crystallizes upon standing (94% yield). ^1H NMR (500 MHz, $CDCl_3$): δ 10.01 (s, 1H), 8.61 (s, 1H), 8.57 (d, J = 5 Hz, 1H), 7.66 (s, 2H), 7.03 (d, J = 5 Hz, 1H), 2.02 (s, 6H), 2.01 (s, 3H). $^{13}C\{H\}$ NMR (500 MHz, $CDCl_3$): δ 192.2, 151.1, 147.9, 147.6, 144.4, 136.2, 135.9, 130.8, 128.9, 122.9, 20.11, 16.13. MS(ESI) *m/z*: $[M+H]^+$ Calcd. for $C_{15}H_{15}N_1O_1$ 226.12; Found 226.09.

Synthesis of 4-(3-methylpyridine)-1-(E)-styryl-(4-bromobenzene)-3,5-diemthylbenzene (4). An oven dried flask was charged with **3** (1.0 g, 4.53 mmol), **6** (1.39g, 4.53 mmol), KO*t*-Bu (1.0 g, 9.07 mmol), and THF (35 mL) under N_2. The reaction was stirred at room temperature for 2 h then poured into water and extracted with dichloromethane. The organic layer was dried over Na_2SO_4, filtered and concentrated under reduced pressure. The crude product was purified by column chromatography on silica gel using a gradient of 30−100% ethyl acetate in hexanes to afford 1.32 g of the title compound, a white solid (78% yield). ^{1}H NMR (500 MHz, $CDCl_3$): δ 8.61 (s, 1H), 8.55 (d, J = 5 Hz, 1H), 7.52 (d, J = 8.5 Hz, 2H) 7.50 (d, J = 8.5 Hz, 2H), 7.31 (s, 2H), 7.17 (d, J = 5.5 Hz, 1H), 7.09 (s, 2H), 2.14 (s, 3H), 1.96 (s, 6H). ^{13}C{H} NMR (500 MHz, $CDCl_3$): δ 136.5, 136.2, 135.3, 131.8, 128.9, 127.9, 127.6, 125.8, 124.1, 121.4, 60.4, 20.2, 16.3, 14.2. MS (ESI) *m/z*: $[M+H]^+$ Calcd. for $C_{22}H_{20}N_1Br_1$ 378.09; Found 378.11 [100%], 380.09 [97%].

Synthesis of 2-(4-{2-[4-(3-methyl-pyridin-4-yl)-3,5-dimethyl-phenyl]-vinyl}-phenyl)-malononitrile (5). An oven-dried flask was charged with NaH (247 mg, 10.3 mmol) and 4 mL degassed DME. Malononitrile (343 mg, 5.2 mmol) in degassed DME (4 mL) was added drop-wise at 0 °C, and the resulting white suspension was stirred for 1 h at room temperature under N_2. Compound **4** (650 mg, 1.7 mmol) in degassed DME (4 mL) was added via syringe at room temperature, followed by $Pd(PPh_3)_4$ (198 mg, 0.17 mmol). The flask was fit with a condenser and heated to 85 °C overnight. The reaction mixture was quenched into 50 mL water and neutralized with 5 % HCl to pH = 7, causing the solution to turn orange with some visible precipitate. The aqueous solution was extracted with DCM, and the organic phase was washed with brine, dried over Na_2SO_4, filtered and concentrated under reduced pressure. Silica gel column chromatography using 10−100 % ethyl acetate in hexanes affords 500 mg of the title compound as a light yellow-brown powder (81 % yield). ^{1}H NMR (500 MHz, $CDCl_3$): δ 8.57 (s, 1H), 8.52 (d, J = 6.5 Hz, 1H), 7.63 (d, J = 10.5, 2H), 7.49 (d, J = 10.5, 2H), 7.30 (s, 2H), 7.13 (s, 2H), 7.09 (d, J = 6.5, 1H), 1.99 (s, 3H), 1.96 (s, 6H). ^{13}C {H} NMR (500 MHz, $CDCl_3$): δ 151.1, 147.7, 139.7, 135.9, 135.5, 131.5, 130.8, 127.8, 127.6, 126.75, 126.0, 124.7, 123.7, 27.9, 20.2, 16.2. MS (ESI) *m/z*: $[M+H]^+$ Calcd. for $C_{25}H_{21}N_3$ 364.18; Found 364.19; $[M-H]^-$ Calcd. for $C_{25}H_{21}N_3$ 362.16; Found 362.13. Anal. Calcd. For $C_{25}H_{21}N_3$□0.6 H_2O: C, 80.23; H, 5.98; N, 11.23. Found: C, 79.92; H, 5.56; N, 11.05.

Synthesis of 2-[4-(2-{4-[3-methyl-1-(2-propyl-heptyl)-1H-pyridin-4-ylidene]-3,5-dimethyl-cyclohexa-2,5-dienylidene}-ethylidene)-cyclohexa-2,5-dienylidene]-malononitrile (TMC-3-EH) (6). An oven dried flask was charged with **5** (200 mg, 0.55 mmol) and 15 mL dry DCM under N_2. Freshly prepared 2-ethyl-1-hexyl triflate (170 mg, 0.65 mmol) was added slowly to this solution, which was then stirred at room temperature for 2 h. The solvent was then removed *in vacuo*, and the resulting yellow precipitate was washed with hexanes. The solid was then re-dissolved in 15 mL DCM to which NaOMe in MeOH (0.5 M, 1.5 mL) was added drop-wise, causing the color to change from orange to deep red. The solution was stirred for 10 minutes, then the solvent was removed under reduced pressure to yield a dark red gel, to which 20 mL DCM and 20 mL H_2O were added. The organic phase was dried over Na_2SO_4, and the solvent was removed under reduced pressure to yield a red liquid. The pure product was obtained by silica gel column chromatography using THF, then a gradient of 5−9% MeOH in DCM as eluents. The resulting red flaky solid was suspended in DCM, and the product precipitates as a bright orange powder, which is isolated by filtration and washed with cold DCM to afford 162 mg of the title compound as an orange powder (62% yield). ^1H NMR (500 MHz, d^6-DMSO): δ 9.17 (s, 1H), 9.01 (d, J = 7.5 Hz, 1H), 7.98 (d, J = 8 Hz, 1H), 7.38 (s, 2H), 7.29 (d, J = 10.5, 2H), 7.13 (d, J = 20 Hz, 1H), 6.91 (d, J = 20 Hz, 1H), 6.73 (d, J = 10.5, 2H), 4.50 (m, 2H), 2.13 (s, 3H), 2.07 (m, 1H), 1.90 (s, 6H), 1.50-1.20 (m, 8H), 0.85 (m, 6H). Anal. Calcd. For $C_{33}H_{37}N_3$*0.2 CH_2Cl_2: C, 81.03; H, 7.61; N, 8.50. Found C, 80.94; H, 7.65; N, 8.53.

Synthesis of 2-[4-(2-{4-[3-methyl-1-(2-octyl-decyl)-1H-pyridin-4-ylidene]-3,5-dimethyl-cyclohexa-2,5-dienylidene}-ethylidene)-cyclohexa-2,5-dienylidene]-malononitrile (TMC-3’) (7). An oven dried flask was charged with **5** (285 mg, 0.78 mmol) and 15 mL dry DCM under N_2 then cooled to 0 ºC. Freshly prepared 2-octyl-1-decyl triflate (170 mg, 0.65 mmol) was added slowly to this solution, which was then stirred at room temperature for 24 h. The solvent was then removed *in vacuo*, and the resulting yellow precipitate was washed with hexanes. The solid was then re-dissolved in 15 mL DCM to which NaOtBu (160 mg, 1.6 mmol) in 2 mL MeOH was added drop-wise, causing the color to change from orange to deep red. The solution was stirred for 10 minutes, the diluted with 20 mL DCM and washed with 50 mL H_2O were added. The resulting red solid was recrystallized from hot IPA to yield 210 mg of the title compound as a bright orange powder (42% yield). ^{1}H NMR (500 MHz, d^6-DMSO): δ 9.18 (s, 1H), 9.01 (d, J = 7.8 Hz, 1H), 7.98 (d, J = 7.7 Hz, 1H), 7.39 (s, 2H), 7.28 (d, J = 10.7 Hz, 2H), 7.14 (d, J = 20.4 Hz, 1H), 6.91 (d, J = 20.4 Hz, 1H), 6.73 (d, J = 10.5 Hz, 2H), 4.50 (d, J = 9.6 Hz, 2H), 2.14 (s, 3H), 2.07 (m, 1H), 1.90 (s, 6H), 1.30-1.10 (m, 32H), 0.85 (t, J = 6.7, 6H). ^{13}C {H} NMR (500 MHz, d^6-DMSO): δ 158.52, 145.59, 143.20, 142.51, 139.32, 138.02, 134.41, 133.40, 130.59, 128.93, 127.48, 126.17, 125.99, 125.61, 122.02, 118.61, 64.71, 31.76, 30.65, 29.92, 29.60, 29.57, 29.46, 29.42, 29.24, 29.17, 29.10, 25.86, 25.84, 22.56, 20.04, 16.79, 14.42. Anal. Calcd. For $C_{45}H_{61}N_3$: C, 83.93; H, 9.55; N, 6.52. Found C, 84.02; H, 9.38; N, 6.51.

4-(diethyl phosphonate)benzylbromide (8). An oven-dried flask was charged with triethyl phosphite (5 mL, 29.2 mmol) and 4-bromobenzyl bromide (6.63 g, 26.5 mmol) under N_2. The flask was sealed, and heated to 85 °C overnight. The reaction mixture was distilled under reduced pressure (50 torr, 90 °C) to afford the 7.52 g of the title compound as a colorless viscous liquid (92% yield). ^{1}H NMR (400 MHz, $CDCl_3$): δ 7.40 (d, J = 8.5 Hz, 2H), 7.14 (dd, J1 = 8.5 Hz, J2 = 2.5 Hz, 2H), 4.00 (m, 4H), 3.05 (d, J = 21.5 Hz, 2H), 1.22 (t, J = 7.5 Hz, 6H).

S3.5 IR spectrum of solid TMC-3’

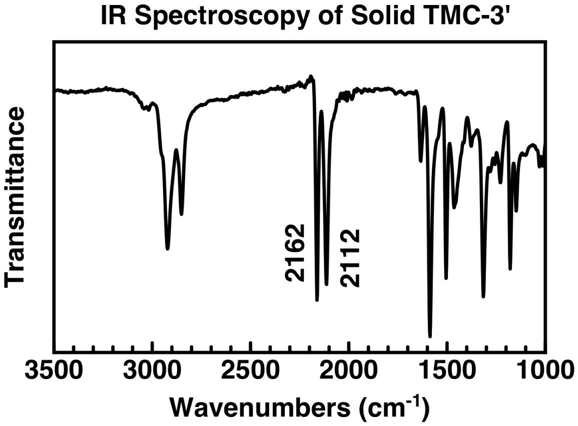

Figure S3.3. Solid-state IR spectrum of **TMC-3’**.

Vita

ALEXANDER J. LOU

EDUCATION

Northwestern University; Evanston, IL ***July 2018***
Ph.D. in Chemistry; GPA: 3.8/4.0

Kellogg School of Management, **Northwestern University**; Evanston, IL ***Summer 2017***
Management for Scientists and Engineers Certificate Program

Williams College; Williamstown, MA ***2013***
B. A. with Honors in Chemistry

RESEARCH AND WORK EXPERIENCE

Northwestern University | Advisor: *Prof. Tobin Marks* ***2013 – 2018***

Designed and synthesized molecules with large electro-optic (E-O) response for use in high-speed fiber-optic communication

- Synthesized molecules that combine exceptionally high E-O response (in a wide range of environments) with device-compatible molecular properties
- Performed thorough UV-Vis, fluorescence, NMR, crystallographic and cyclic voltammetry characterization on solutions, crystals, and thin films to understand observed E-O response; determined that modified molecular geometry leads to improved physical and E-O properties
- Developed organic salt additives as a potential processing technique to enhance E-O response
- Fabricated films from E-O molecules via spin-coating

Developed molecules with large nonlinear optical (NLO) response for use in all-optical switching

- Optimized synthesis of exceptionally promising twisted molecule (TMC-3’) from 13 steps to 6
- Initiated collaboration with a team of physicists to investigate intensity and wavelength dependence of TMC-3’ NLO response; realized a ~4x improvement over previous generation as a result of higher-order NLO contributions, invited to present results at specialized NLO conferences
- Mentored an undergraduate in air-free organic synthesis techniques

Established three-member subgroup focused on elucidating relationships between newly discovered magneto-electric (M-E) NLO phenomena and tunable molecular parameters

- Collaborated with theoreticians to identify structural motifs which can enhance M-E NLO response; utilized quantum computation to confirm theoretical results
- Disseminated updates and authored contributions at 4 annual program reviews

Williams College | Advisor: *Prof. Sarah Goh* ***2013***

Synthesized and characterized temperature-responsive polymer-based micelles

- Assessed micelle formation and thermo-responsivity by dynamic light scattering; micelles displayed potential as drug-delivery vehicles based on temperature dependent size changes
- Gained proficiency in air-free polymerization and polymer characterization using GPC and NMR

Los Alamos National Laboratory | Advisor: *Prof. Rico Del Sesto* ***Summer 2011, 2012***

Realized high-throughput, nondestructive extraction and analysis of organic dyes using ionic liquids

- Improved method for forensic analysis of dyes in natural fibers by replacing destructive solvents with mild ionic liquids; increased sensitivity towards dyes and reduced requisite sample size

AWARDS

- NDSEG Graduate Research Fellowship (~$100,000/3yrs) ***2014 – 2017***
    - Highly competitive national fellowship supporting graduate study
- ACS Organic Division Undergraduate Award ***2013***
- Sigma Xi Research Honors Society ***2013***

SELECTED SCIENTIFIC PUBLICATIONS (5 OF 7)

[5] **Lou, A.**; Righetto, S.; Barger, C.; Zuccaccia, C.; Cariati, E.; Macchioni, A.; Marks, T. J. Unprecedented Large Hyperpolarizability of Twisted Chromophores in Polar Media. *Journal of the American Chemical Society* **2018, DOI:** 10.1021/jacs.8b04320.

[4] **Lou, A.**; Righetto, S.; Cariati, E.; Marks, T. J. Organic Salts Suppress Aggregation and Enhance Hyperpolarizability of a π-Twisted Chromophore. *Submitted*.

[3] **Lou, A.***; Dreyer, E.*; Rand, S. C.; Marks, T. J. Molecular Design Principles for Magneto-Electric Materials: All-Electric Susceptibilities Relevant to Optimal Molecular Chromophores. *Journal of Physical Chemistry C* **2017**, *121* (30), 16491-16500.

[2] Shi, Y.; **Lou, A.**; He, G.; Baev, A.; Swihart, M.; Prasad, P.; Marks, T. J. Cooperative Coupling of Cyanine and Tictoid Twisted π-Systems to Amplify Organic Chromophore Cubic Nonlinearities. *Journal of the American Chemical Society* **2015**, *137* (14), 4622-4625.

[1] Lovejoy, K.; **Lou, A.**; Davis, L.; Sanchez, T.; Iyer, S.; Corley, C.; Wilkes, J.; Feller, R.; Fox, D.; Koppisch, A.; Del Sesto, R. Single-Pot Extraction-Analysis of Dyed Wool Fibers with Ionic Liquids. *Analytical Chemistry* **2012**, *84*, 9169-9175.

INVITED SCIENTIFIC PRESENTATIONS (4 OF 5)

[4] Foundations of Nonlinear Optics, Skidmore College, NY – *Oral presentation* **2018**

[3] Materials Research Society National Meeting, Boston, MA – *Oral presentation* ***2017***

[2] Foundations of Nonlinear Optics, University of the Bahamas – *Oral presentation* ***2017***

[1] Foundations of Nonlinear Optics, Tufts University, MA – *Oral presentation* ***2016***

LEADERSHIP ROLES

PLU Chemistry Honor Society Board Member, Northwestern University ***2015 – 2017***

- Organized events for chemistry graduate students (enrollment ~250) to increase morale and encourage a collaborative environment (annual budget ~$6,000)
- Managed allocation of $5,750 to assist 20 students with travel for professional development; introduced rubric system to improve the consistency of travel awards
- Planned committees for selection of competitive departmental research awards

Lab Safety Designate, Northwestern University ***2014 – 2018***

- Participated in monthly safety meetings outlining new programs and potential hazards

- Facilitated contact between post-doctoral associates, graduate students and administrative figures

TEACHING EXPERIENCE

Laboratory Teaching Assistant ***2010 – 2014***

Northwestern University and Williams College (Organic Chemistry and Physical Chemistry)

- Taught introductory and advanced laboratory skills to classes of 15-20 students; tutored organic chemistry course material, graded lab reports and exams, prepared pre-lab lectures

SOCIETIES

- Phi Lambda Upsilon Chemistry Honors Society ***2015 – 2018***
- Materials Research Society **2017 – *Present***